Understanding Spatter and its Spatial Variations in Laser Powder Bed Fusion of Ti6Al4V

Daniel Lund

A thesis submitted in partial fulfillment of the requirements for the degree of

Master of Science

University of Washington

2024

Committee:

Dwayne Arola

Ramulu Mamidala

Xu Chen

Reid Schur

Program Authorized to Offer Degree:

Materials Science and Engineering

University of Washington

Abstract

Understanding Spatter and its Spatial Variations in Laser Powder Bed Fusion of Ti6Al4V

Daniel Lund

Chair of the Supervisory Committee:
Dwayne Arola
Department of Materials Science and Engineering

Laser Powder Bed Fusion (LPBF) is rapidly expanding for the fabrication of metal engineering components that are traditionally produced by conventional manufacturing processes. However, in applications involving the manufacture of stress-critical and safety-critical components, it is limited by the need to certify the parts for their reliability and service life. Methods of non-destructive evaluation (NDE) exist but can often be costly and/or time consuming. Spatter occurs as a byproduct of the LPBF process and consists of the discharge of molten media from within the meltpool. Spatter is influenced by, and thus representative of other process variables, such as gas flow, laser-powder interaction dynamics, and thermal gradients in the build environment. To this end, we explore the opportunity for using predictive technologies for LPBF that are based on spatter, particularly the examination of spatter obtained through in-situ imaging. Results show that the generation of spatter is dependent on powder type (i.e. processing) and for a specific powder the orientation of spatter trajectories is found to be influenced by both scan angle and gas flow. Trends in concentration of spatter content with respect to distance from build regions are presented.

TABLE OF CONTENTS

LIST OF FIGURES

LIST OF TABLES

ACKNOWLEDGMENTS

First and foremost, I'd like to acknowledge the support of my family in pursuing science and discovering the joy in figuring out how things work.

I wish to express sincere appreciation to my professors in the Materials Science and Engineering Department at the University of Washington, my advisor, Dwayne Arola, and my colleagues in the LAMPR group who helped me accomplish much of the research in this project.

Finally, I'd like to thank my undergraduate professors at Chico State who shared a genuine and formidable enthusiasm for studying physics. It is this enthusiasm that convinced me this would be worth coming back to.

DEDICATION

To Marta, for her support and encouragement during this project.

Chapter 1. INTRODUCTION

Additive manufacturing needs predictive technologies to achieve widespread adoption in industry. The metal additive manufacturing (AM) community has been very active in this area and made tremendous progress in the use of in-situ monitoring technology to evaluate builds and the metal quality. One of the exciting new areas that offers the potential for identifying or predicting defects and other aspects of build quality is the patterns of spatter, which can be observed using in-situ imaging tools.

1.1 Metal Additive Manufacturing

Additive Manufacturing (AM) refers to a family of manufacturing processes, often identified as 3D printing, that use data from a digital 3D model to produce a part through a layer-by-layer deposition of material. In fact, the AM family encompasses seven classes of processes, including material extrusion, and powder bed fusion, the latter of which will be described in the following section. These processes employ variations of a general technique of iteratively depositing and bonding a series of 2D thin layers of material on top of each other [3]. The individual layers are produced with shapes that are infinitely variable, enabling creation of parts of virtually any physically possible geometry. Furthermore, while conventional manufacturing processes such as welding, casting, machining, and forming often require dedicated tooling and the use of a series of processes to achieve a product, AM allows the fabrication of novel designs with intricate features with no additional tooling needed. In cases where overhanging features must be produced, support structures may be necessary to achieve accurate printing, but these support structures can be printed in parallel with the part and thus do not require significant modification of the process.

Additive manufacturing (AM) was developed roughly 40 years ago for producing non-structural prototypes of engineering components for proof-of-concept purposes [16]. Using fairly inexpensive polymer feedstock materials, a net-shape representation of a component could be created from a CAD model in a matter of hours [17]. While usually not durable enough for most load-bearing applications, the ease of producing prototypes substantially increased the rate of producing and

assessing design iterations. Now that AM technology has developed further to support the production of components out of a variety of metals, AM can now be used to produce functional end-use components [16]. This further accelerates the design process and allows engineers and designers greater agency in developing ideas into end-use products. Components can be produced for a low initial investment cost. Also, compared to traditional manufacturing processes such as casting, injection molding, and machining, design complexity of components is much less restricted. AM methods allow the creation of intricate component geometries that would be difficult or impossible to manufacture with conventional methods [16, 18]. Furthermore, it bypasses the traditional lengthy process of developing a prototype and then producing the tooling that will be required for production using a traditional casting or forging process.

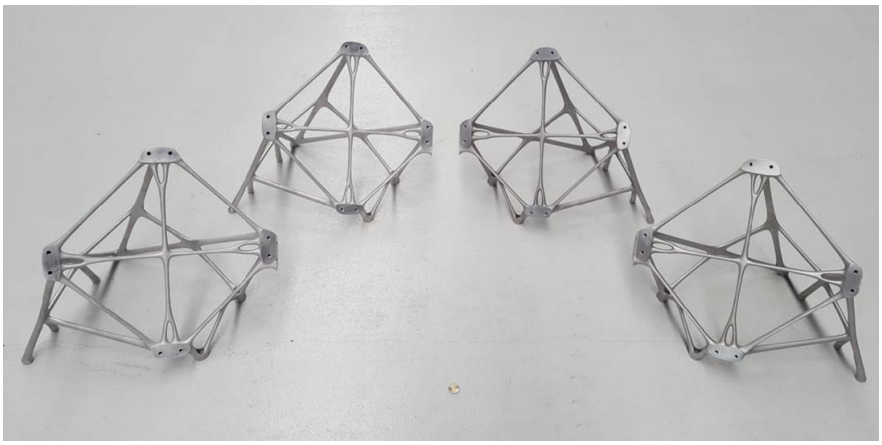

Figure 1.1: Lattice structures with low volumetric material density can be made with little wasted material using AM [1].

Additive manufacturing is often described as a disruptive technology, [19] in that it has developed from a niche market as a means of producing proof-of-concept models with low mechanical strength, to a means of efficiently producing end-use parts with strength comparable or equal to parts produced by conventional methods. In this manner it is overtaking or "disrupting" conventional manufacturing methods. For parts having low volumetric density, AM shines by requiring only the material needed to complete the physical part. Figure 1.1 shows parts that would be

prohibitively expensive to produce with subtractive methods, but easy and efficient to make using AM.

1.2 Laser Powder Bed Fusion

Laser Powder Bed Fusion (LPBF) represents a subset of AM processes that uses a laser beam to selectively melt particles of metal powder together into a solid part.

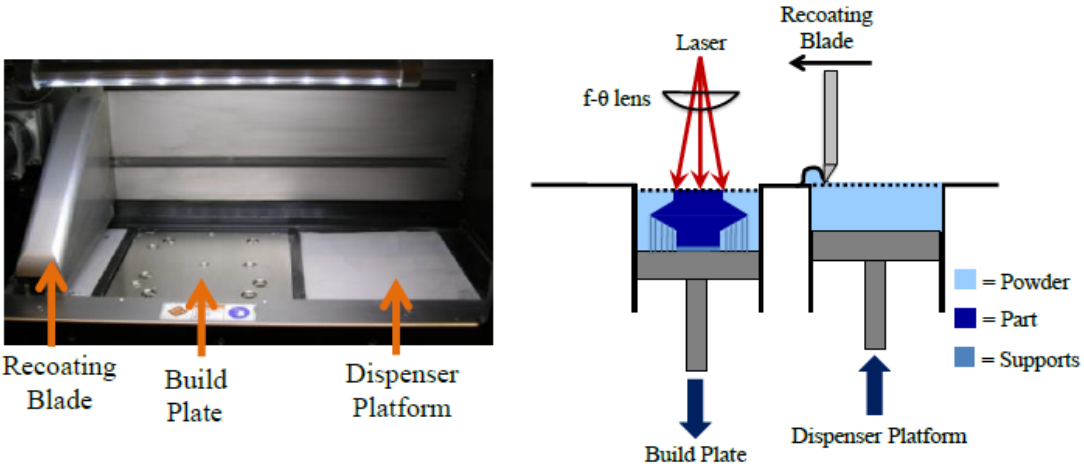

Figure 1.2: Build chamber of a typical LPBF system and schematic representation of the LPBF process [2].

The principal components of a typical LPBF system are shown in Figure 1.2, including a build plate, dispenser platform or piston, recoating blade, and laser. The process consists of raising the dispenser platform to provide a controlled dose of powder, incrementally lowering the build plate, spreading a thin layer of powder across the build plate with a rake, and scanning the surface of the powder with a laser to achieve an adequate temperature for melting the metal and achieving a bond of adequate strength with the previous layer [16]. The path of the laser beam is controlled by a scanning mirror that deflects the beam to scan the desired region across the powder bed surface. The shape of the scanning region is controlled to follow the shape of the part cross section at that

layer height [16]. This process is iterated layerwise over the height of the part until the build is complete.

Before the build is started, the atmosphere in the build chamber is purged and back-filled with an inert gas (usually argon) to prevent oxidation of the molten metal. A ducting system circulates the inert gas from the back to the front of the build chamber to displace process byproducts produced by interactions between the laser and the powder. Process byproducts will be discussed further in the following section.

1.3 Spatter

When the laser energy incident on the powder bed is absorbed by the powder, the powder melts in a small region near the laser spot. This region, identified as the meltpool, is typically on the order of 100-300 μ across [3, 20] though this varies depending on powder composition and morphology, laser energy and scanning parameters, and other processing conditions. **Spatter** refers to molten metal ejected from the meltpool in a powder bed fusion (PBF) process onto the powder bed or elsewhere in the build cavity. The spatter reaction is caused, in part, due to the effects of Marangoni convection centrifugal forces and vapor recoil pressure in the melt pool [3]. Once the local momentum of liquid metal exceeds the pressure produced by surface tension, a portion of the material within the melt pool is ejected. Vaporization pressure can also displace unmelted powder particles which can land back in the melt track, resulting in poor surface quality [21, 22]. This process is illustrated in Figure 1.3. The ejected material can form particles, up to 6 times as large as the original powder particles [23], which are generally 10-60 μm in diameter [16, 24]. An assessment of ejected spatter particles has shown that they often travel about 1-2 m/s, [20] but can occasionally reach speeds of up to 15 m/s [20]. When spatter is deposited on the build surface, the particles, often being much larger that the feedstock powder particles, may not undergo complete melting during the processing of subsequent layers, leading to the formation of lack-of-fusion defects [25]. Spatter can be formed under a fairly broad range of conditions representative of the LPBF process [26, 27] and is a primary contributor to the formation of defects [28, 3].

There are multiple mechanisms associated with the formation of build defects in parts resulting

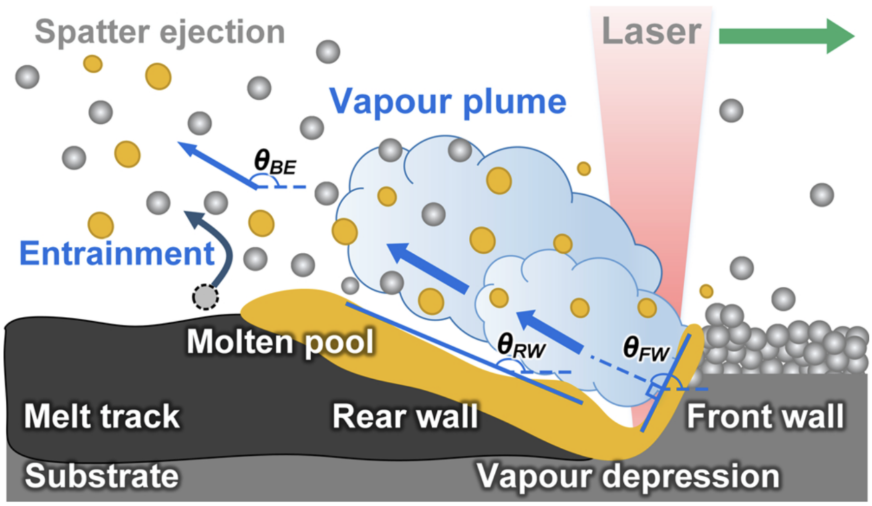

Figure 1.3: Schematic of the correlation between the depression zone and the backward-ejected spatter in LPBF [3].

from spatter. If a significant amount of metal is ejected from the meltpool, the absence of metal will leave a depression on the build surface. After the following recoating cycle, the depression will be filled with powder, resulting in a region where the powder paving thickness is greater than the layer thickness. And due to the excess powder, this region will likely experience inadequate fusion following laser exposure, potentially resulting in a lack-of-fusion (LOF) defect [9]. Spatter can also reduce the energy density input by deflecting or obstructing the laser beam [7], and spatter particles that are redeposited on the build surface can interfere with subsequent fusion due to the larger size of spatter particles or composition [29, 30]. Ejected spatter can also uptake oxygen during its flight if the build cavity is not fully inert, resulting in oxygen contamination of the part [29]. Young et al. [31] identified five types of spatter that occur in LPBF, and discuss the mechanisms of their formation. As a result of these detrimental aspects of spatter, a more detailed description of the mechanisms and the potential methods for identifying related spatter events is warranted and will be covered in Chapter 2.

Spatter can be captured by in-situ optical tomography (OT) imaging. This involves a camera that captures thermal images of the build space, often with an extended exposure lasting the

duration needed to process one layer.

1.4 Objectives

While metal AM offers many new possibilities for engineering and manufacturing, there are barriers that must be overcome before widespread adoption of AM can be achieved [28]. One issue involves the variability of mechanical properties in AM-produced parts. Suppliers of metal AM products for critical applications must certify that the quality of metal and mechanical properties of the components are adequate for their application before they can be put into service [28]. Certification programs for metal AM components typically cost suppliers on the order of $10 million over a span of years [32]. The most common method of validation, X-ray micro-computed tomography (μCT) analysis, can be expensive, time consuming, and otherwise unsuitable for implementation at production scales [28]. This is a major obstacle for adoption of AM [33].

There is a need to certify AM-produced parts in a manner that takes less time and expense than μCT analysis. Strong efforts and progress have been made in examining trends in the in-situ data, particularly for meltpool imaging [34, 35]. However, much less attention has been focused on the characteristics of process byproducts such as spatter and condensate, despite the fact that both of these byproducts can result in defects [28, 29]. The primary goal of this study is to examine spatter through in-situ imaging and evaluate relationships with build quality and other process variables such as inert gas flow. The specific objectives include:

i) to develop an approach for characterizing spatter from optical tomography data acquired during the build

ii) to distinguish spatial variations in spatter across the build space and contributing variables

iii) to interpret the importance of powder source to spatter generation, and

iv) to assess opportunities for examining the inert gas flow distribution in the build cavity according to spatter characteristics

Chapter 2. LITERATURE SURVEY

2.1 Process Monitoring

Many commercial LPBF systems now offer built-in tools to collect data during the build process in-situ, using integrated sensing equipment, and layer by layer throughout the manufacture of parts. For instance, in the case of the EOS M290 used in this study, the in-situ data available includes meltpool imaging, optical tomography imaging (OT) of the powder bed, and powder bed imaging. It is also possible to monitor and document machine variables, such as temperature, oxygen content, pressures, axis positions, and laser power [8]. These tools enable the user to establish baseline parameters for normal machine operation, and can be helpful for identifying abnormal operating conditions or events that can reduce the quality of parts. Following the completion of a build, this data can be further analyzed to aid in identifying any features of concern.

There are many potential opportunities for improving the LPBF process through process sensing and in-situ monitoring. Process sensing can enable the detection of and even the prevention of defects. It also has the potential for optimizing various part properties such as dimensional accuracy and surface roughness [33]. In-situ sensing tools can also be used to examine related process variables, such as the use of high-speed Schlieren imaging to examine the inert gas flow [36]. Using existing data such as input parameters and geometry together with in-situ data and ex-situ reporting of finished parts offers possibilities to improve and develop the manufacturing process much faster than with manual adjustment alone.

In-situ monitoring tools in LPBF are largely applied to identify anomalous events and/or the introduction of defects during printing. Some common types of defects and other LPBF process features are detailed below:

- **spatter**: molten metal ejected from the meltpool as a result of laser-powder interaction dynamics. Ejection of the molten metal is driven in part by two main process phenomena: (1) vapor pressure produced by the molten metal following laser exposure, and (2) Marangoni convection (temperature-dependent surface tension) forces due to temperature gradients in

the meltpool [3].

- **plume**: a mixture of metal vapor, plasma, and small condensed particles above the melt pool, generated when laser energy vaporizes the metal in the meltpool [4]. Plume can interfere with the transmission of laser energy to the powder bed, and in some cases of laser welding can attenuate the incident laser energy by as much as 40% [37]. As the plume cools, the particles can accumulate on surfaces in the build chamber and form condensate [38].

- **condensate**: condensed metal vapor that forms a sparse distribution of particles with a diameter of 10-150 nm [4]. Condensate can accumulate on surfaces inside the build chamber and attenuate or defocus the laser beam if allowed to accumulate on optical components, [38, 39] which can cause process defects. Due to its high surface area to volume ratio, condensate from flammable metals can be highly reactive and presents a safety hazard to handle.

- **denudation**: displacement of powder particles close to the melt track due to the vapor recoil pressure produced by the meltpool [4, 5, 22]. The upward-directed gas jet produced by metal vaporization creates a lateral draw of gas into the jet, entraining nearby powder particles in the process [22]. These particles are often launched upward and deposited elsewhere in the build space [22]. While this phenomenon can be minimized by scanning the powderbed with the laser at low powder to pre-sinter the powder [20, 40, 41], this adds additional time to the build process and may be undesireable to implement in industry.

- **balling**: breaking up of the meltpool into spherical droplets due to capillary instability when the length to width ratio of the meltpool is high or when the incident energy intensity is low [26]. Conditions that inhibit wetting of the powder bed with the meltpool can cause balling, such as the presence of oxides on the surface of the powder particles [38]. Conditions that favor wetting of the powder bed with the meltpool can decrease the incidence of balling, as can decreasing the length to width ratio of the meltpool [26, 42].

- **trapped gas void**: a void in the part produced when metal solidifies around a portion of gas [16]. This gas can be either evolved from the meltpool or captured from the build atmosphere [16]. Trapped gas voids, also referred to as gas porosity, tend to be spherical in shape and small in size, generally 100 μm or less [28, 43].

- **lack-of-fusion (LOF) void**: a void in the part formed when the incident energy density is insufficient to fuse the powder layer to the previous layer. LOF voids can be 250 μm or more, [16] and often have sharp corners that can act as stress risers and initiate premature failure [16]. As a result, LOF porosity tends to be much more problematic than trapped gas porosity.

- **keyhole**: a deep depression in the meltpool formed under conditions of high incident energy intensity. When energy intensity exceeds a certain threshold, approximately 10^6 W/cm^2, [4] the shape of the meltpool changes from wide and shallow to narrow and deep due to the rapid rate of metal vaporization. The absorptivity of the meltpool increases to nearly 100% due to the multiple incidences of the laser beam upon the keyhole surface, as shown in Figure 2.1. Collapse of the molten metal on the surface of a keyhole can result in a trapped gas void at the bottom of a keyhole, as shown in a simulation by Khairallah et al. in Figure 2.2.

LPBF is typically operated as an open loop process, meaning corrective actions are only taken post build. There is opportunity for improving the performance of LPBF systems by implementing real-time process control [33], which involves continuous monitoring of process signatures and taking corrective actions during the build. Process parameters can be continuously adjusted to support optimum build results, and in certain cases defects that would result in part rejection can be repaired. In cases where part defects cannot be repaired the build can be halted to minimize waste, or the area of concern flagged for offline inspection. Kruth et al. [44] implemented feedback control for a self-built LPBF system, monitoring the meltpool with a photodiode and CMOS camera. By combining the information from these two sensors, melt pool area and geometry could be determined. This information was used for continuous control of the laser power to maintain a

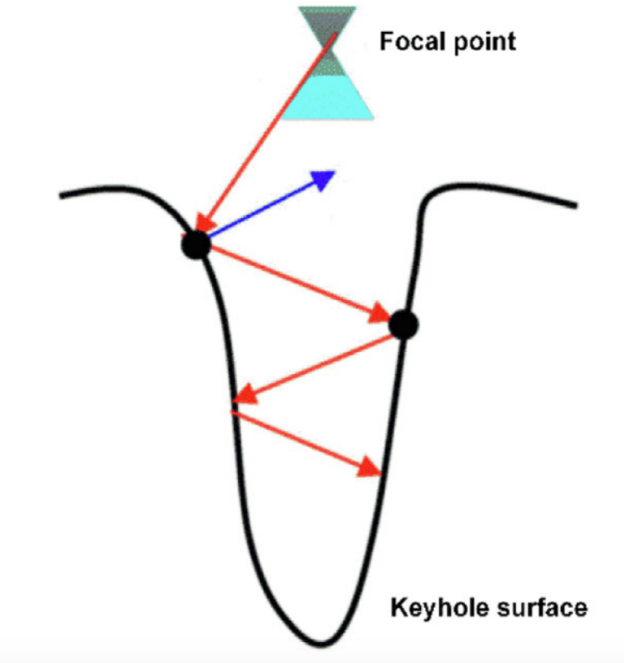

Figure 2.1: Multiple laser beam incidence on the keyhole surface [4].

constant melt pool area. In this study, parts with overhanging features and no support structures were designed so that variations in laser power would have a more dramatic effect on part quality. In particular, excess laser power would cause the meltpool to sink into the powder bed. The authors printed parts with and without continuous feedback control and showed that feedback control resulted in improved part quality. Real-time process control needs to be explored if it is to be applied to improve quality in LPBF.

While in-situ data collection tools are helpful for identifying macroscopic variations in the build process, such as excess spatter or variations in brightness of the meltpool, they often do not have adequate spatial resolution to identify the intricacies of some defect features. Yin et al. [45] observed micro-scale explosion behavior in the meltpool during LPBF of a brass alloy using a high-power pulsed diode laser and a high-speed video camera, with a spatial resolution of about 4 μm/pixel. By comparison, the OT camera on the EOS M290 has a spatial resolution of approximately 125 μm/pixel. While this behavior is more dramatic in the case of a brass alloy, where the

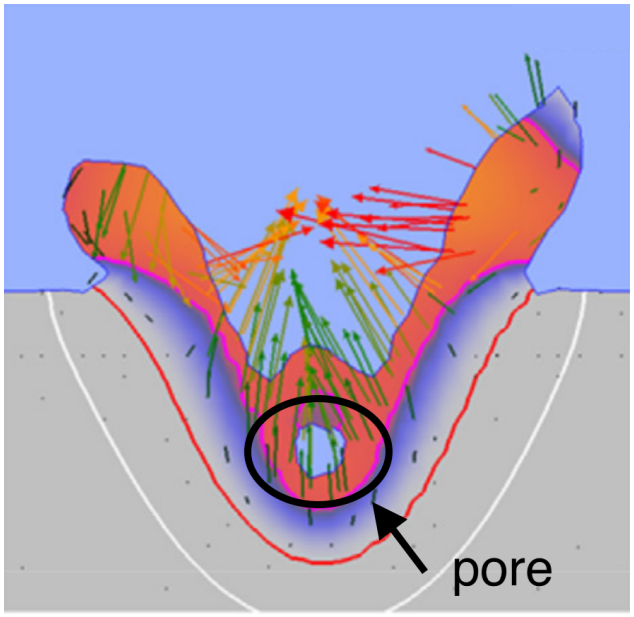

Figure 2.2: Simulation showing formation of a pore at the bottom of a keyhole following keyhole collapse [5].

melting point of the system is significantly higher than the boiling point of zinc, similar explosion behavior has been observed in LPBF of Ti-6Al-4V alloy [46]. Systems that implement effective process control using in-situ tools must take into account the limitations of in-situ measurement systems. Nevertheless, in-situ tools are woefully underutilized and have great potential to improve the quality of LPBF parts.

2.2 Gas Flow Dynamics

The recirculating shielding gas present in a LPBF system serves to protect the meltpool from exposure to oxygen and other contaminants. It also serves to remove process byproducts from the build space. Process byproducts, including spatter, can be redeposited in nearby areas of the build space and "contaminate" subsequent layers in the build, resulting in future defects. As a result, the dynamics of gas flow in LPBF is a hot topic of current research efforts. Gas flow dynamics is relevant to spatter as well due to its influence on spatter trajectory. Anwar and Pham [7] showed that parts built with higher gas flow velocities have higher tensile strength, which is expected to

result from the gas effectiveness of carrying process byproducts to the outlet. If the velocity is too high, however, the gas flow will disrupt the uniformity of the powder bed. Hence, there is an optimum flow speed that effectively clears byproducts generated by the meltpool without disturbing unmelted powder.

Due to the contributions of gas flow to build quality, there is intrinsic value in quantifying the gas flow distribution to understand characteristics of interest and identify problematic regions. Gas flow in the build chamber can be evaluated using computational fluid dynamics (CFD) simulation tools, or experimentally using anemometry or particle image velocimetry (PIV). Wang and Chang [47] performed a study of gas flow using a generalized rectangular build chamber with the nozzle located at the left edge of the build plate and an outlet port located at the right edge of the plate. This chamber was designed to resemble the build chamber of a typical industrial selective laser melting (SLM) system. The experimental chamber spanned 325 mm from left to right, and 605 mm in depth. Gas flow velocity was measured using two constant temperature anemometers, which were oriented perpendicular to each other to measure the streamwise and transverse components of flow. Flow was qualitatively visualized by introducing a particle aerosol and illuminating the aerosol with a laser light sheet [47]. Experimental results were compared to CFD simulations with combinations of nozzle and outlet sizes, as well as over a range of distances between the nozzle/outlet ports and the build plate. The objective was to find the conditions that produced optimal flow uniformity. This effort was continued by Chen and Wang [6], who measured gas flow using particle image velocimetry (PIV) in a redesigned build chamber with dimensions about twice as large, again seeking to replicate the conditions of a typical SLM system. In these experiments, the nozzle was located above the build space and the two outlets were on the left and right edges of the build plate as shown in Figure 2.3. This is similar to the gas flow strategy used in the EOS M400 [48]. They were able to capture the velocity profiles of the gas in the build chamber using two different nozzle shapes. Based on their results, they were able to determine which nozzle would be more effective for an LPBF process. It appears that results obtained from experiments of this type could be used to optimize the flow profile in an LPBF system to support optimum build quality [6, 30]. Further improvement could be achieved by controlling the direction of gas flow to

minimize the amount of spatter redeposited on build regions [30]. With a broader understanding of the details of the LPBF process, it is possible improve build results by using properly selected process parameters.

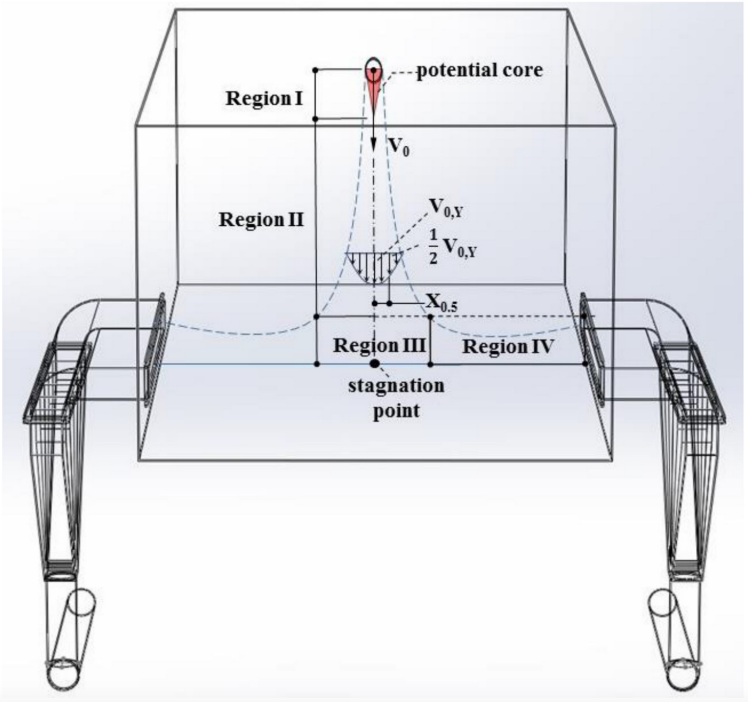

Figure 2.3: Experiment setup for PIV measurement of gas flow in the build chamber [6].

Anwar [7] observed that when the laser scans in the direction of the gas flow, the spatter is more likely to be blown into the path of the laser. This is because the upwind-ejected spatter will be turned around by the force of the gas flow after which it can re-enter the path of the laser, as illustrated in Figure 2.4. Under these conditions, less spatter was collected in the outlet, suggesting that some of the spatter may have been "melted" upon re-incidence with the laser beam. More visible light emissions were also observed in this scan direction, further suggesting repeat interactions with the laser. The laser energy is attenuated by these repeat interactions, resulting in wider and shallower weld tracks, poor or incomplete fusion and decreased ultimate tensile strength (UTS) of the finished parts [7]. Scanning against the direction of gas flow ejects spatter downwind, where it

will be carried further away from the laser [7, 30]. Scanning against the direction of gas flow helps to minimize the amount of spatter redeposits [30].

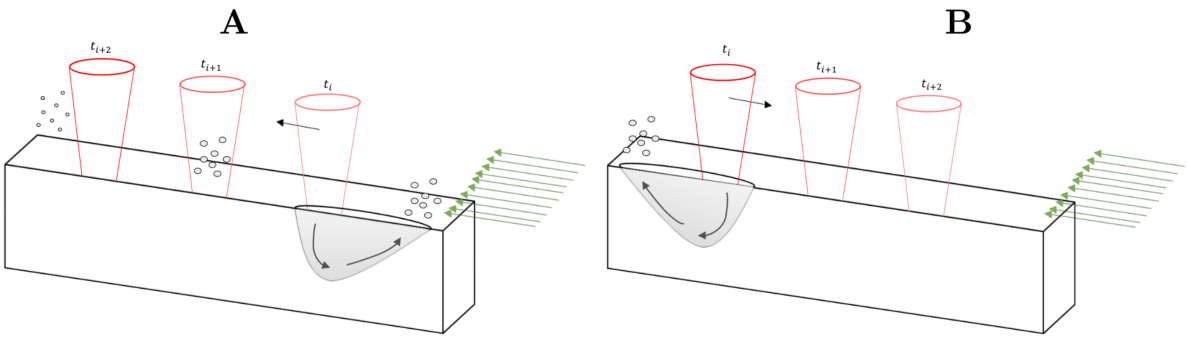

Figure 2.4: Schematic of laser beam scanning. **A**: scanning in the same direction as the flow. **B**: scanning against the direction of the flow [7].

2.3 Spatter Formation

The generation of spatter is a complex process that merits attention. There are multiple mechanisms by which spatter is generated, and while some of the attributes are well understood, ongoing research continues to reveal new insights about the process. The purpose of understanding the underlying mechanisms responsible for the formation of spatter is to guide interpretation of build data to predict defects, or any other attributes detrimental to part properties.

As mentioned in the introduction, spatter in LPBF is caused primarily due to the effects of Marangoni convection centrifugal forces and vapor recoil pressure produced by the meltpool [3]. The Marangoni effect in LPBF refers to movement of molten metal in the melt pool due to temperature dependent surface tension [3, 4, 39]. This phenomenon is shown in Figure 2.5. Because the temperature of the metal at the bottom of the meltpool is higher than the metal at the tail end of the meltpool, the surface tension is lower than at the tail end of the meltpool. This results in a flow of molten metal from the bottom of the depression upwards and back towards the cooler metal at the tail end of the meltpool [4]. The high energy intensity of the laser, typically on the order of 10^5

- 10^6 W/cm^2, heats the molten metal in the meltpool enough to cause vaporization on the surface, which creates a region of increased pressure above the meltpool. In turn, this increased pressure causes a depression in the meltpool. Depending on the magnitude of the recoil vapor pressure, as well as other process attributes, molten metal can be driven from the bottom of the vapor depression up the walls of the depression and ejected after it continues upward past the top of the depression [4, 5, 39]. Yin et al. [3] observed that spatter ejection characteristics are influenced by the shape of the meltpool. Spatter ejection angles tend to follow the angle of the rear wall of the meltpool, identified as Θ_{RW} in Figure 2.6. This angle gets lower, or closer to horizontal, with increasing laser power, and in turn, the backward ejection angle of the spatter particles (Θ_{BE}) follows this trend [3]. This describes the general process of spatter formation in LPBF, though there are many additional phenomena in the LPBF process that can also serve as contributors.

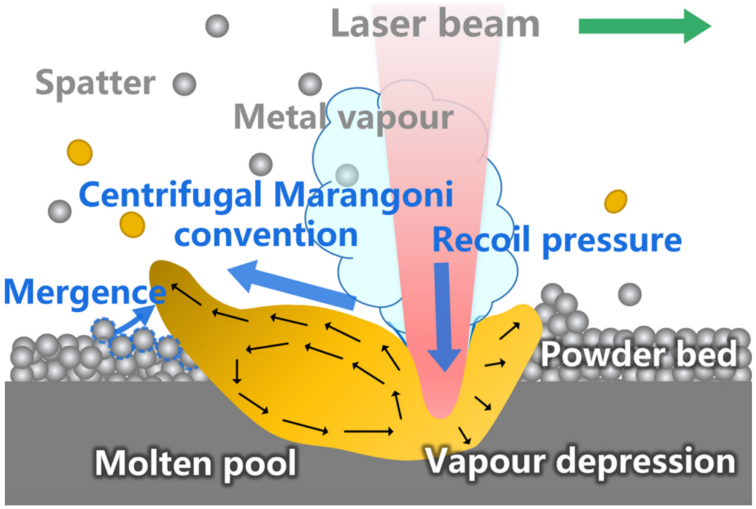

Figure 2.5: Schematic of the meltpool showing Marangoni convection and the vapor depression [3].

One example of a secondary mechanism of spatter generation is "droplet" spatter, resulting from interactions between the meltpool and the powder bed. Gunenthiram et al. [26] identify droplet spatter formation in two modes. In a typical LPBF process, metal powder particles next to

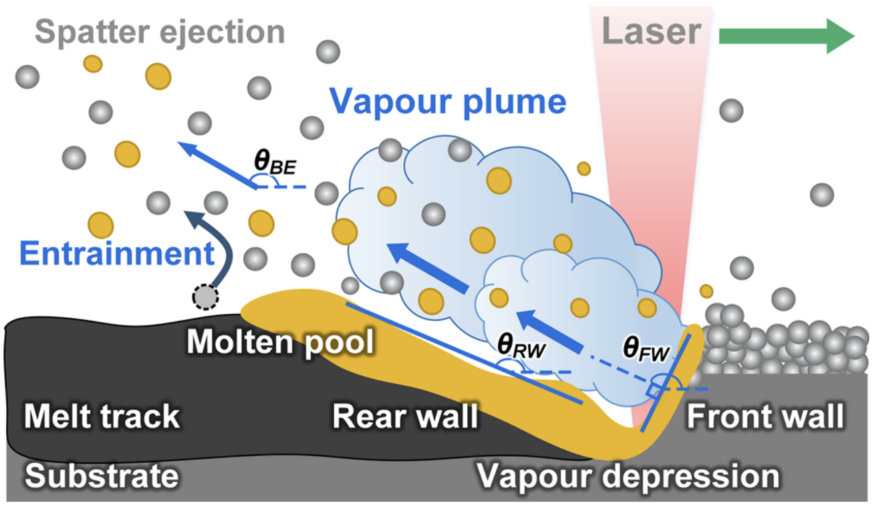

Figure 2.6: Schematic of the correlation between the depression zone and the backward-ejected spatter in LPBF [3]. Shown previously in Figure 1.3.

the meltpool can be heated by conduction, become liquid, and agglomerate, forming larger droplets of molten metal that are near but not part of the meltpool. Under conditions of high laser energy intensity, the high vaporization pressure and acceleration of liquid out of the vapor depression can shear off and eject the adjacent satellite liquid agglomerations as spatter. For low energy intensity, the surface tension may either draw the droplets back into the melt pool, or cause spheroidization and ejection of the extremities of the melt pool, producing droplet spatter despite the lower energy intensity and vapor recoil pressure. It is apparent that spatter can not easily be avoided and, to be successful, robust process control must be able to capture mechanisms of spatter generation under varied conditions.

Overall, spatter formation is associated with a degradation in mechanical properties of the metal relative to builds without spatter [25]. As such, spatter is considered to be a detrimental feature of the LPBF process [29]. Yin et al. [3] reported that protrusions extending above the top of the current layer, including spatter present on the build surface, can make the recoater blade jump. That reaction of the recoater blade can result in irregularities in the thickness of the powder layer [3]. The depression created by the vapor recoil pressure can result in the powder paving

thickness being greater than the layer thickness, in which case the laser may be unable to penetrate the powder, resulting in lack-of-fusion (LOF) voids [3]. Understanding these mechanisms can help inform what types of defects to look for and where to look for them following observation of a significant spatter event.

The metal powder feedstock used in LPBF can take up oxygen through the course of the build process. Deng et al. examined the oxygen uptake of parts produced from austenitic stainless steels [21]. They found that the oxygen content of the parts exceeded what was present in the virgin powder due to oxygen uptake during printing. Further analysis identified that the primary mode of oxygen uptake was by molten spatter absorbing oxygen during flight and landing back on the powder bed [21]. While oxygen uptake is undesireable, EDS analysis can be used to distinguish hot and cold spatter particles according to the oxygen content on the surface of the particles [30].

Upon re-melting of the spatter particles within the meltpool, the oxygen was incorporated into the build. Particles that did not land back in the meltpool were retained with the recovered powder and contributed to the chemistry of metal in subsequent builds. Wang et al. [39] also observed an increase in the oxygen content of CoCr alloy powder in LPBF with increasing reuse cycles. In comparing parts built with virgin powder to parts built with powder that had been reused 6 times, more spatter was present on the surface of the parts built with reused powder [39]. Similar studies on the effects of oxygen uptake have been applied to other AM processes, such as Montelione et al. [49] in the case of electron beam (EB) PBF. This is a critical detail concerning powder reuse: reusing powder saves money but the quality of the resulting parts is diminished. The authors in [39] also performed a build with the shielding gas recirculation system turned off, which enabled the evolved smoke to accumulate in the build chamber. As expected, elements with increased concentration in the smoke were observed to diffuse into the spatter particles. Therefore, a variety of spatter characteristics, including size, temperature, and length of path could have correlations to the oxygen content of finished parts and the recovered powder.

Spatter in LPBF has been studied through simulation. However, these simulations are often oversimplified and fail to capture sufficient detail to represent the process accurately. In the work of Yuan and Gu [50], the authors simulated the powder bed using a continuum model that revealed

insights into the effects of process parameters on the build, but failed to capture the effects of a randomly distributed bed of powder particles. Khairallah et al. [5] successfully simulated melt dynamics in a powder-scale simulation modeling features of the LPBF process in detail, including vapor recoil pressure and a bed of randomly distributed particles with a realistic size distribution. The result is that powder scale effects such as vapor entrainment of particles near the meltpool or particle agglomeration can be observed. Their model produced 3D temperature and velocity data on a 2 μm scale, based on heat diffusion computed on the nanosecond scale to produce high-resolution representations of interactions between the laser, powder, and meltpool. The results of their simulations reveal a breadth of insights about the LPBF process, and supplementary understanding through the videos shared with their article, [20]. For instance, they consider the situation where a large spatter particle, or raised agglomeration of powder particles is present on top of the powder bed. When the laser strikes this irregularity with adequate laser power (e.g. 300 W), the vapor pressure produced by the interaction with the laser is able to dislodge the particle, albeit with a comparatively small disturbance of the meltpool depth. However, if the laser power is lower, (150 W) the vapor pressure instead pushes the particle down into the meltpool, resulting in a protrusion that later interferes with recoating. This form of processing and defect was correlated with inferior mechanical strength. These results were used to recommend high laser power but within limitations to avoid keyholing [20]. Additionally, agglomerations of particles coincident with the melt track will often break up into smaller particles when the laser strikes them. These reactions can cause spatter to form and land elsewhere in the powder bed, contaminating the surroundings and also causing a cascading effect that generates more spatter [20]. As such, achieving good part quality depends on minimizing spatter in the build process.

One cause of spatter formation identified in the simulations is when the internal pressure of the meltpool exceeds the surface tension due to the momentum of the melt flow, combined with the applied vapor recoil pressure [20]. This can happen when there is a rapid change in either meltpool temperature or laser power. Preventing spatter requires controlling the rate of temperature increase of the meltpool, which limits the change in recoil pressure and in turn meltpool depth. A common cause of spatter generation is when the laser changes direction at the ends of the melt track and

delivers a higher energy density input than when traversing at constant speed. It is possible to remedy this issue by turning the laser off during the period of reversal and turning it back on after. However, the rapid ramp up after turning the laser back on can cause unstable meltpool conditions and subsequently spatter. Khairallah et al. [20] identified a maximum rate of change of the depth of the meltpool, dz/dt, below which spattering does not occur. A PID controller was implemented in the simulation to vary the laser power to maintain a target meltpool depth defined by a tracer point. When the laser is turned on, this point is lowered at a rate selected to be less than the critical value of dz/dt. The laser power map associated with a meltpool of stable depth can be adopted in actual AM systems. Simulations can reveal possibilities for direct improvements to real-world processing.

2.4 Monitoring Spatter

There are many approaches available to acquire and assess in-situ data obtained from process monitoring. There are an equally large number of methods that have been explored for using that data to achieve process improvement, particularly the use of in-situ imaging data. However, far less work has been reported concerning spatter. Perhaps that is because the generation of spatter is a complex process that can be influenced by many factors. For instance, local material properties, incident laser energy or volumetric energy density (VED), thermal gradients in the machine, flow dynamics of the shielding gas, and laser scan direction, can all be contributors [28]. In turn, tracking these attributes enables offline analysis that can be used to improve the LPBF process.

Many popular LPBF systems offer native in-situ data collection tools. The EOS M290 features EOSTATE, a process monitoring suite composed of the following tools [8]:

- **EOSTATE MeltPool**: samples meltpool radiant emissions in the range of 400 nm - 900 nm along the path of the laser beam. Additional features of the software include the ability to monitor the data in real time during printing and flag any regions that deviate from a set of user-specified parameters.

- **EOSTATE Exposure OT**: A CMOS camera captures two optical tomographic images of the build space for each layer over the time scanning each layer. One image is a temporal integration of radiant emissions captured by the camera, the other image represents a maximum of radiant emissions. Spatter can be studied from these images.

- **EOSTATE PowderBed**: captures two visible light images for each layer with a CCD camera, one after recoating and another after scanning. Process anomalies, such as edge swelling, spatter redeposits, or incomplete powder spreading can be identified in these images.

- **EOSTATE Base**: captures machine parameters such as gas flow rate and pressure, oxygen level, temperatures, laser power, axis positions, and other information related to the build.

These features are illustrated in Figure 2.7.

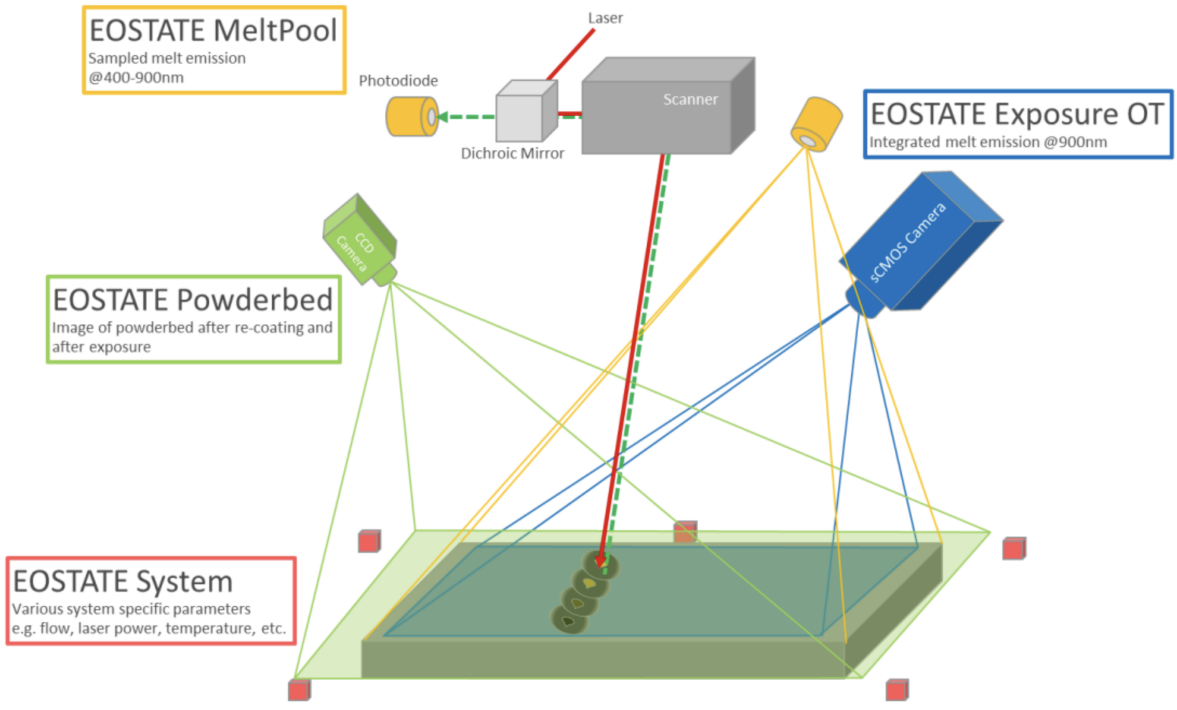

Figure 2.7: Illustration of process monitoring tools offered in EOSTATE [8].

Snow et al. [28] used in-situ imaging of spatter to train a dynamic segmentation convolutional neural network (DSCNN) used for the prediction of defects in LPBF. They added a 24.4 megapixel visible light camera to their LPBF system to capture images of the powder bed at two instances, including after laser melting and after powder spreading. While the EOS M290 system used in [28] has native in-situ OT imaging support, this imaging system and other native in-situ systems have inadequate spatial resolution to provide an accurate representation of defects or other regions of concern. Furthermore, the addition of high-resolution visible light imaging combined with the native OT imaging provided a more robust dataset to train the DSCNN and in turn more accurate model results [28].

Liu and Wen [4] used in-situ X-ray imaging to examine the formation of keyholes in LPBF. Keyholes occur when the vaporization pressure of the metal forms a depression in which laser energy is reflected a number of times. Under these conditions, energy absorption increases dramatically, resulting in the formation of localized intense vaporization within the melt pool and the generation of spatter [51]. Multiple in-situ approaches are capable of monitoring vaporization in the melt pool, including IR imaging and acoustic monitoring [33]. While in past research some authors assume that the effects of vaporization can be neglected, [52] Semak and Matsunawa [51] suggest that more attention should be placed on monitoring vaporization of metal in LPBF. In addition to keyholing, metal vaporization results in significant heat loss from the melt pool as well as displacement of nearby unmelted powder particles, a phenomenon known as "denudation". Incorporating these details into analysis of LPBF results in a more accurate representation of the process.

The majority of studies reported on spatter dynamics have relied on 2D imaging. Wu et al. [40] demonstrated that with a well-designed image processing algorithm, 2D imaging of spatter content can be used to aid in detecting the number of spatter particles in realtime. Fischer et al. [9] used high speed imaging (1000 FPS) with a plenoptic camera to track the motion of spatter particles in an LPBF process in 3D. The average particle velocities measured using plenoptic imaging were found to vary from 0.5 m/s to 5 m/s, a fairly wide range but well within the appropriate range for spatter particles in LPBF. Particles were initially ejected at roughly 3-4 times these velocities

but slowed within 1-2 milliseconds to approximately average values. Tracking particle motion in 3D revealed that spatter is primarily ejected up and backward (opposite the direction of laser scanning), but there is often a considerable component of velocity perpendicular to the melt track. A plot of spatter trajectories as viewed from above the build plate in [9] is shown in Figure 2.8. This highlights the complex nature of spatter generation in the LPBF process. They asserted that with an understanding of spatter dynamics, it could be possible to control the scan angle to reduce the impact of spatter on the build and to know where defects are most likely to exist in the component. They also commented on the opportunity to use spatter dynamics to better understand the impact shielding gas has on the build. In a later article these authors expanded their work to include measuring temperature of the particles by computing the ratio of two narrow band wavelength intensities [53]. These monitoring techniques offer a wealth of information about the LPBF process which has direct application to predicting build quality.

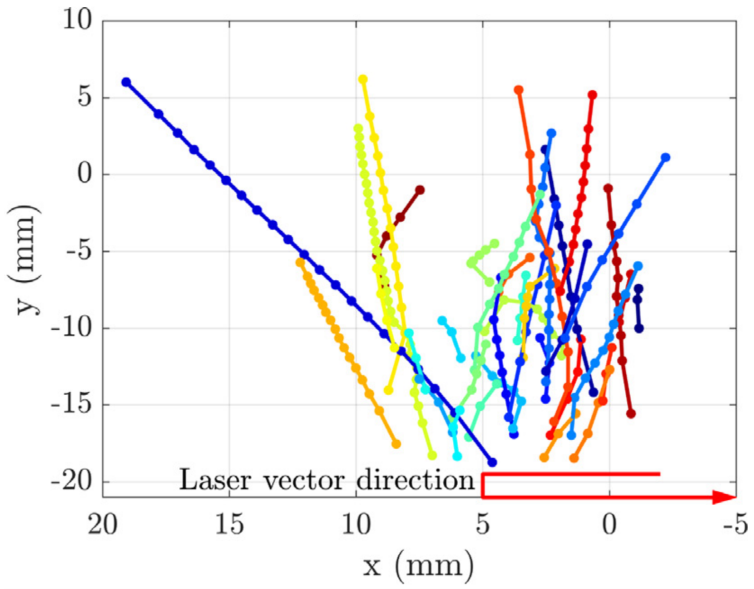

Figure 2.8: Top view of spatter trajectories showing significant transverse motion [9].

2.5 Defect Prediction

LPBF has tremendous potential to expand the possibilities of modern manufacturing, but widespread adoption is limited by various factors, including the need to qualify the mechanical properties of finished parts. The defects generated during LPBF are well-classified, but their formation mechanisms are not well understood. Additionally, the cost of qualifying finished parts can be up to twice as much as the direct costs associated with manufacturing [32]. For these reasons there is interest in better understanding the mechanisms of defect formation, as well as developing methods of qualification that are more efficient and economical.

For parts to be used in applications where their structural behavior is critical, such as any load bearing application, it must be established that the parts are free from any defects that could compromise their mechanical properties. Defects in LPBF-produced parts may occur when process parameters are not properly tailored to the build conditions. Some of the most common defects in LPBF parts are trapped gas voids, lack-of-fusion voids, keyholes, and balling [16, 33], which were discussed in Section 2.1.

The primary method of non-destructive evaluation (NDE) applied to AM parts typically involves the use of X-ray micro-computed tomography (μCT). This approach involves performing a series of scans of the part from varying angles and using an algorithm to reconstruct a 3D model of the part that describes the radiographic density. Defects in the part that may contribute to premature failure can be identified by μCT through grayscale variations, which correlate to porosity. The drawback of this approach is that it is costly, time consuming, and often requires destructive testing of numerous witness coupons, [28] which makes it difficult for AM technologies to compete as a manufacturing solution if all parts must be evaluated by μCT . In addition, various errors in the μCT process can mask defects, especially when scanning large parts [28]; repeatable scan results can be difficult to achieve without the use of a commonly accepted quality metric for scans [54] and a scan standard.

Due to the many challenges in applying μCT to AM parts in industry on a production scale, there is substantial research interest in being able to identify defects in AM parts without evaluating

the parts using computed tomography (CT) methods. Non-destructive evaluation (NDE) of parts produced with LPBF has been performed with various in-situ imaging systems, such as high speed x-ray imaging, sonic inspection, vibrational analysis, optical emission spectroscopy, and more [33]. But there is now a community wide goal to utilize in-situ data or an aspect of process monitoring for early detection, or at the very least as a first-pass screening method.

Meltpool imaging has received the most focus for predicting defects in LPBF-produced parts. For example, Estalaki et al. [34] trained a K nearest neighbors machine learning model to predict defects in LPBF-produced parts according to the time above the apparent melting threshold and the maximum radiant intensity of the meltpool. They found that the maximum radiant intensity was more important than time above the apparent melting threshold. Model effectiveness was improved by using the 1st, 2nd, and 3rd-nearest neighbors for voxel state prediction, compared to using the central voxel alone. In addition to K-nearest-neighbors, they tried five other models, including Random Forests, Decision Trees, Multi-Layer Perceptron (MLP), Logistic Regression and AdaBoost. Their Random Forests model was found to be the most effective in identifying correlations with a F1 score of 0.966, indicating a fairly robust model. Other studies that have used meltpool data to to predict defects include [43, 55]. There is indeed good reason to pay attention to meltpool characteristics as proper control of meltpool shape and size has been shown to have a positive effect on part properties [18, 56].

While meltpool imaging is not only useful it is also thoroughly studied. Monitoring spatter data has received recent attention and could offer more effective prediction of anomalies in the printing process. Repossini et al. [57] used both melt pool imaging as well as spatter imaging for defect detection, and found that use of spatter data significantly improved the ability of their model to detect over and under melting conditions [57]. Using images of spatter collected from a high speed camera, they were able to fit an ordinal logistic regression model that predicted defects better than with meltpool data alone. In fact, it was found that using spatter data alone for prediction produced results comparable to those achieved by combining spatter and meltpool data [57]. Different processing conditions were shown to produce different spatter characteristics. For example, an increase in energy density caused an increase in the average and variance of the number of

ejecta. They noted that one limitation of tracking particles with visible imaging is that the observed spatial spread of the particles depends on the time the particle temperature remains above a level that results in visible light emissions as well as the ejection velocity [57]. The success in defect prediction in this experiment shows that the LPBF community can benefit from further study of spatter and its relation to part quality.

Very recently, Snow et al. [28] presented an innovative approach to using spatter data for defect prediction. A build was performed using process parameters and build geometry that facilitated spatter generation. The images captured were then labeled so that each pixel was classified in one of eight categories: powder, printed, spatter-on-part (non-flaw), μCT flaw (large), μCT flaw (small), and more. This allowed the DSCNN to be sensitive to different types of process signatures. The trained network was able to detect the majority of the large flaws identified in the μCT data, and most of the flaws that weren't detected were beyond the resolution limit of the imaging system. To quantify the performance of their model, they introduced a metric regarded as the $a_{90/95}$, corresponding to the flaw size with a 90% probability of detection on the lower 95% confidence interval. They argue this metric is a more accurate representation of the model's ability to identify large flaws, as well as of model performance as a function of flaw size. For this study, the $a_{90/95}$ was 541 μm, which is fairly large for a LPBF flaw. Nevertheless, the authors believe it could be reduced with more training data, regrouping the μCT data based on model predictions, and adding additional sensing modes capable of detecting additional process signatures. This represents a significant step forward in the application of spatter data to defect prediction in LPBF, and suggests that future work will likely bring additional progress.

2.6 Summary

LPBF facilitates production of high value components for the manufacturing, engineering, and related technical sectors, but the widespread adoption of LPBF manufacturing is currently limited by the time and expense needed to certify the mechanical properties of parts as adequate for the application. It has become clear that trial and error is a very ineffective approach to process improvement, which needs to be more focused and strategic. Spatter has been identified as a key

contributor to the formation of defects in LPBF parts, yet the nature of spatter generation as well as the extent of its influence on part properties are not well understood by the LPBF community. A means of in-situ flaw detection is needed in order for LPBF to be successful. It is understood that the LPBF process is comprised of the interaction of a number of unique features, including (but by no means limited to) a bed of particles with a continuous size distribution, a laser beam with an energy intensity distribution, convection, vaporization, and other fluid phenomena in the meltpool, heat conductivity of metal in both the solid and liquid phases, and ballistic motion of ejected particles subject to drag forces from a forced gas flow, all of which influence the generation, movement, and deposition of spatter. These process features can be studied both through numerical simulation and in-situ data collection to better understand the influence of LPBF process variables in order to improve part quality, predict the characteristics of defects present in LPBF parts, and improve the viability of the LPBF process. The research presented in this thesis makes an effort to expand the current understanding of this field.

Chapter 3. MATERIALS AND METHODS

There is potential to monitor the development and distribution of spatter through in-situ imaging. And with complementary analysis, this information could provide new understanding of the process physics, as well as serve as a resource for evaluating the quality of metal in a build and performing non-destructive detection. For instance, the baseline characteristics of spatter could be characterized quantitatively from a build of known quality and spatter events. Then leveraging that information, the spatter signatures in future builds could be compared to this training data to identify any features that deviate from expected characteristics and merit additional examination.

3.1 EOS M290 printer

The builds in this study were printed on a commercial LPBF system at the University of Washington, the EOS M290. This printer uses a 400 watt ytterbium fiber laser with a wavelength of 1060-1100 nm to melt and fuse the powder into a solid part. This printer has a build area of 250 x 250 mm and a build height of 325 mm [58]. This system directs a cross-flow of inert gas through the build chamber to remove process byproducts, including smoke and condensate. All builds in this investigation were conducted with Argon as the inert gas. The build process consists of a number of steps, including the following:

1. Purge: the atmosphere in the build chamber is flushed by argon gas and vented through an outlet duct. This prevents contamination of the molten metal by hydrogen, oxygen, nitrogen, etc, during processing. The oxygen level in the build chamber is monitored during the build and an alarm informs the operator and interrupts the build if the oxygen level gets too high.

2. Recoating: the build platform moves down by the thickness of one layer of deposited metal, the dispenser piston moves up, and the recoater blade spreads a fresh layer of powder from the dispenser across the build plate.

3. Scanning: the cross sectional shape of the part at the current layer height is scanned with the laser to fuse the powder to the previous layer. The scan pattern is generally a bi-directional hatch to minimize build time and cost. A typical hatch pattern is shown in Figure 3.1.

4. Powder recovery and part removal: the unused powder is removed from the build chamber using either a vacuum or manual means. The build plate is removed with produced components as a unit and the parts are sectioned from the build plate with a wire electrical discharge machining (EDM) process or other mechanical means.

Steps 2 and 3 are performed iteratively as needed to complete the part. The parts routinely need additional post processing before use, such as removal of support structures or machining to achieve the necessary surface finish. The orientation angle of the laser scan path, identified as the scan angle, increments by the hatch rotation with each layer, as shown in Figure 3.2. All builds in this study used a hatch rotation of 67°.

As noted earlier, a ducting system circulates the inert gas from the back of the build chamber to the front. Two inlet nozzles, including an upper and lower nozzle, deliver gas into the build chamber as shown in Figure 3.3.

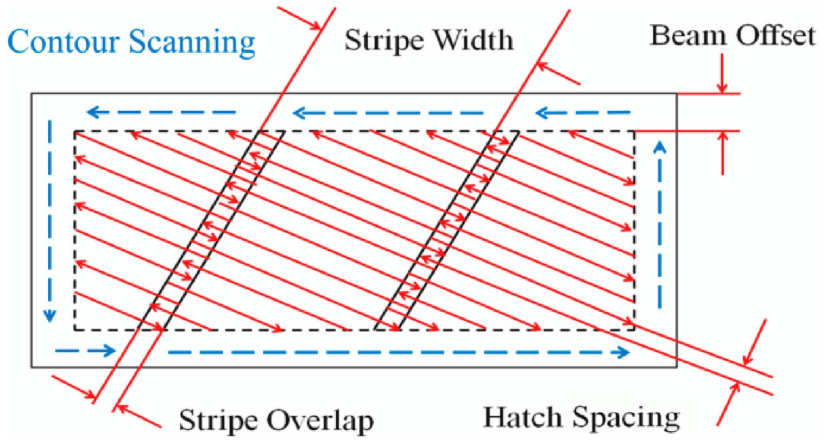

Figure 3.1: Typical hatch pattern for laser scanning and identification of relevant process parameters. [10].

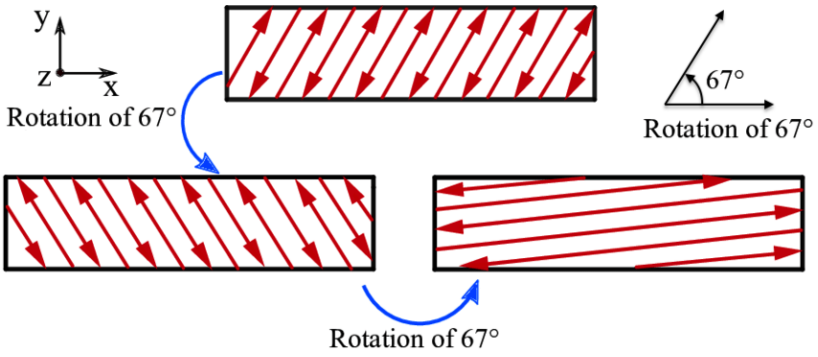

Figure 3.2: Rotation of laser scan pattern with each layer. [11].

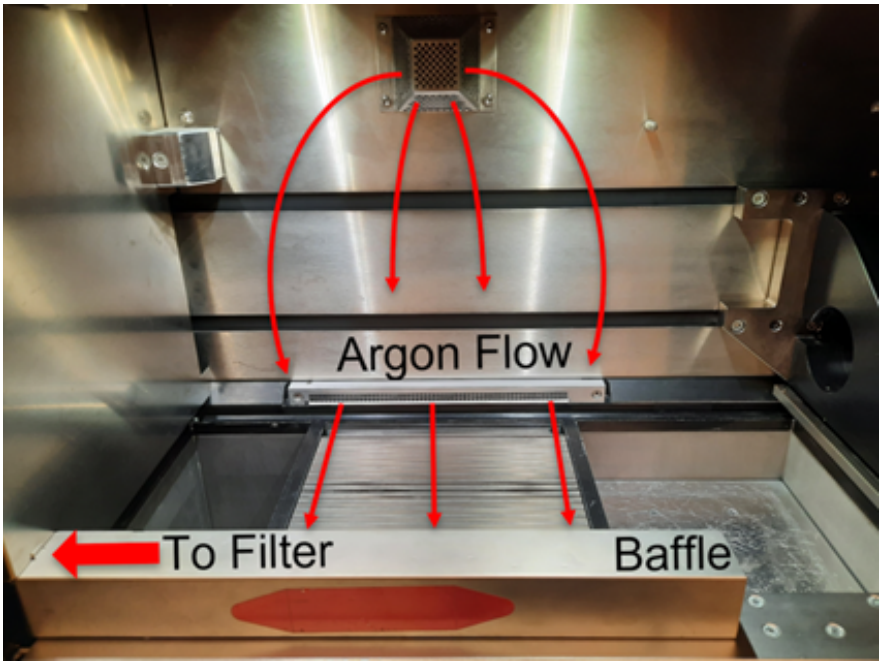

Figure 3.3: Build chamber of EOS M290 printer showing gas flow in the chamber [12].

3.2 Material

The builds in this study were performed using two different Ti6Al4V grade 5 alloy powders that were acquired from two different sources. One of the powder lots was produced using a plasma atomization (PA) process and was acquired from EOS [59], and the second was produced using a gas atomization (GA) process and was provided by GKN [60]. The PA powder from EOS meets specifications for ASTM F2924, and GA powder from GKN was manufactured in accordance with standards defined by AS9100D. Properties of the GKN GA powder and the EOS PA powder are listed in Figures A.1 and A.2, respectively.

3.3 Part Build Configuration

The builds that were performed in this effort are part of a broader round robin investigation that is being conducted to examine mechanical property variability in parts produced by similar model LPBF systems. This round robin study involves 6 participants, including the University of Washington; all of the participants conducted builds of identical design consisting of an array of tensile specimens. All of the specimens were printed on EOS M290 metal AM systems using default parameters and using feedstock powder provided by EOS from lot # 2007910001. The tensile specimens were post-processed according to a standardized procedure and the mechanical properties assessed [15]. The purpose of examining the mechanical properties was to identify any variations in the quality and mechanical behavior of metal between the machines, between different builds performed by the same participant, or between specimens printed in different regions of the build chamber. Details of the study are available in [15].

The build design for the round robin program consisted of identical tensile specimens distributed across 5 different zones and two different levels, as shown in Figure 3.4. The coupons were grouped in clusters within the 5 zones of the build chamber. Zones 1 to 4 occupy each of the four corners of the build space, and Zone 0 is located in the center. The cluster of specimens printed in each zone included specimens printed in both vertical and horizontal orientations. The coupon orientations were rotated in the build plane 5° counter-clockwise from the x-axis to mini-

mize disruption of the recoater blade as it passes over the printed regions. This layout was printed on two different levels (A and B), with each level having 5 zone clusters. Each group of specimens in the respective zones consists of 19 specimens for a total of 190 specimens produced in each build.

Six builds were printed by each participant in total, including two different configurations that were comprised of varying combinations of coupons within the 5 zones. Builds 1 and 6 consisted of metal printed in all 5 zones, while the Builds 2 to 5 consisted of metal printed in Zone 0 and one of the corner zones. Table 3.1 identifies the Zones in which specimens were printed for each build as well as the builds in which each Zone was printed in.

For the GA powder provided by GKN, the build design paralleled that of the round robin program shown in Figure 3.4 (a). However, the design incorporates one level of specimens instead of two, as shown in Figure 3.4 (b) due to the limited volume of the GKN powder. These builds were performed at the University of Washington. The process parameters used for these builds consisted of the default parameters used for Ti6Al4V and are listed in Table 3.2.

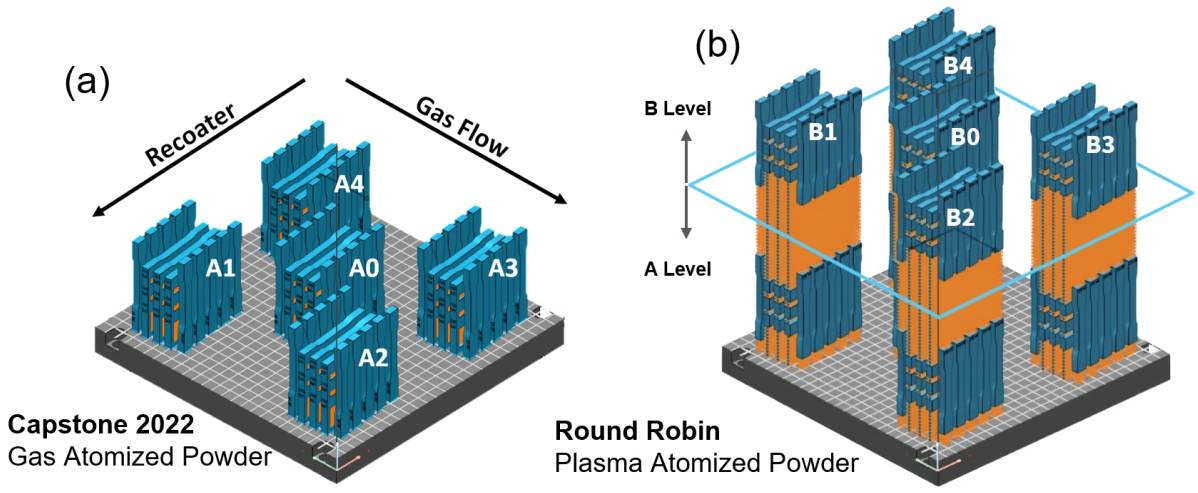

Figure 3.4: Details of the build design outlining the array of tensile coupons with vertical and horizontal orientations for the builds performed with (a) gas atomized and (b) plasma atomized powders. Labels indicate the build zones (0 to 4) on two levels (A and B). Blue indicates dense metal and orange indicates support structure.

Table 3.1: Build and Zone combinations for Capstone 2022 and Round Robin studies.

Build	1	2	3	4	5	6
Zones printed	all (0 to 4)	0, 1	0, 2	0, 3	0, 4	all (0 to 4)
Zone	0	1	2	3	4	
Builds printed in	all (1 to 6)	1, 2, 6	1, 3, 6	1, 4, 6	1, 5, 6	

Table 3.2: Process parameters used for printing [15].

Build Variables	
Laser power	270W
Hatch rotation	67°
Hatch spacing	120 μm
Stripe width	5 mm
Stripe overlap	0.0 mm
Beam offset	0.1 mm
Layer thickness	60 μm

3.4 Image Collection

The EOS M290 at the University of Washington is equipped with the EOSTATE software suite to acquire in-situ data. For the present study, ExposureOT was used to collect optical tomography (OT) in-situ imaging data for all builds. The collected images span the entire build plate area of 250 mm x 250 mm, with each image representing a summation of all radiant exposure observed during the processing of that layer. The OT images are saved as 16-bit grayscale images with a resolution of 2000 x 2000 pixels, which results in a spatial resolution of 125 μm. A representative OT image for a single build layer for the round robin study is shown in Figure 3.5. A summary of image data used for this study is shown in Table 3.3.

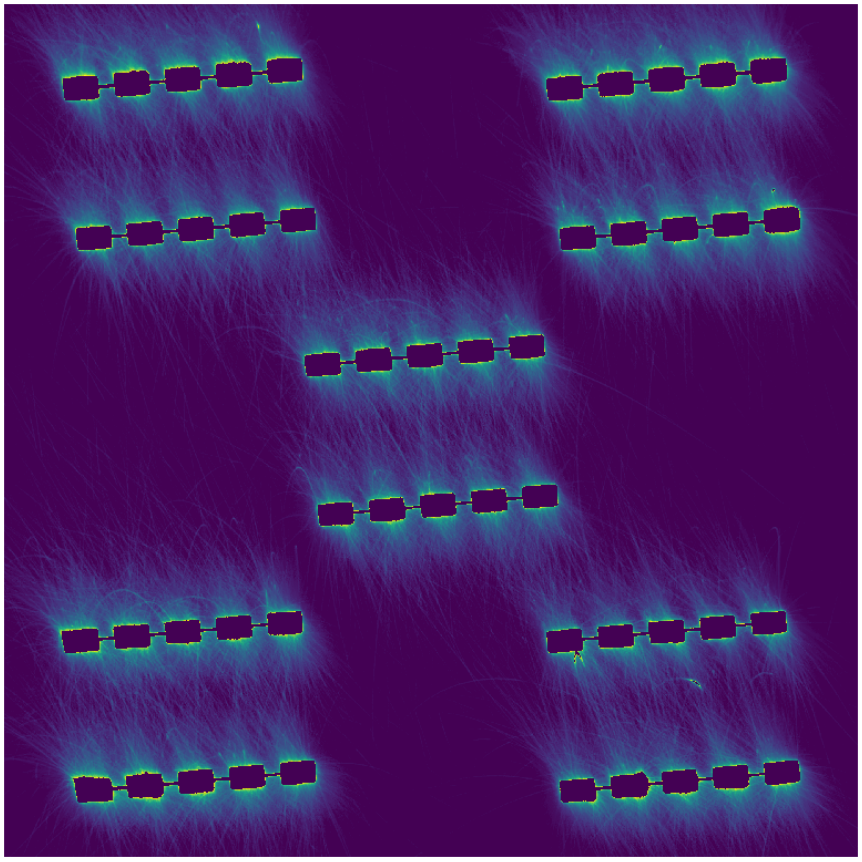

Figure 3.5: Example in-situ OT image with meltpool regions of the tensile specimens omitted. Image has been color scaled to highlight spatter features.

Table 3.3: Details of data used for analysis.

Analysis application	Dataset source	Z min (mm)	Z max (mm)	Layers in range used	# of layers analyzed
Spatter orientation vs. scan angle	GKN GA powder build 6	64.26	65.64	all in range	24
Inter-specimen intensity vs. scan angle, distance from specimen	GKN GA powder builds 1-6	64.26	67.80	all in range	60
"	EOS PA powder builds 1-6	203.40	206.94	all in range	60
Porosity vs. specimen spatter intensity	EOS PA powder build 6, level A	27.48	56.82	scan angle within 6° of vertical	33
"	EOS PA powder build 6, level B	169.50	197.70	scan angle within 6° of vertical	33

3.5 Image Analysis

The spatter distribution was evaluated over the entire build area with respect to machine coordinates. Figure 3.6 shows the coordinate system used for this analysis. Angles are defined counterclockwise with respect to the positive x axis, as shown on the right side of the image. Labels are also shown for Zones 0 to 4, as well as the front and back regions of interest for Zone 0.

Ten regions of interest (ROI) were defined adjacent to the vertical specimens in the OT images of the round robin builds using a Python script [15]. For each zone, a ROI in front of and behind

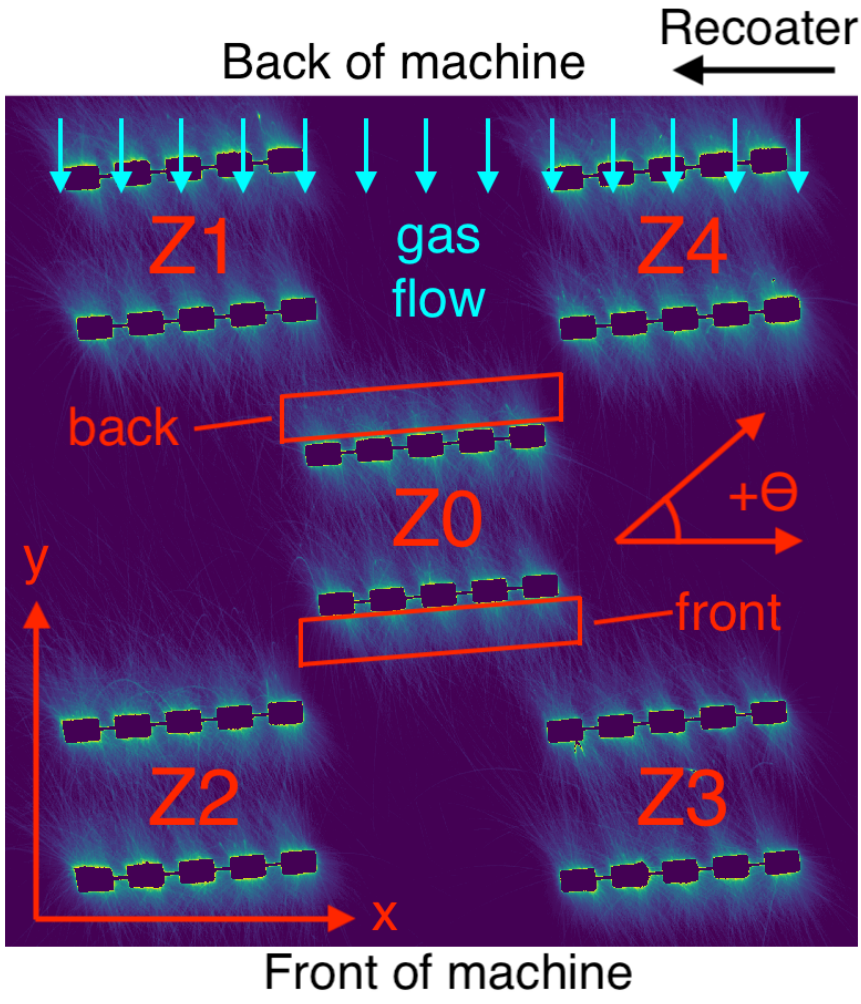

Figure 3.6: In-situ obtained OT image of a layer, labeled to define analysis regions and variables.

the specimen cluster was defined as shown in Figure 3.7. The sectioned ROIs were reshaped from parallelograms into rectangles to make analysis easier. Figure 3.8 a shows a ROI as clipped from the OT image, and Figure 3.8 b shows the same ROI reshaped to be rectangular. By reshaping the ROIs in this manner, distances along the x-axis are preserved, and equal positions along the y-axis correlate to equal distances from the printed specimens. Furthermore, the y-axis of the reshaped ROI remains parallel to the direction of gas flow. Admittedly, the resulting images are distorted from their true shape, but the angular offset of 5° is considered to be minor. This method saves considerable computational expense compared to symmetric rotation.

Unless otherwise noted, all the images examined were from sections of the build consisting of printing of the grip sections of the vertical specimens; all horizontal specimens and other features had been completed in previous layers. Doing so allowed examination of spatter in immediate proximity to the vertical specimens from which it was generated, without the influence of spatter from nearby horizontal specimens in the same cluster.

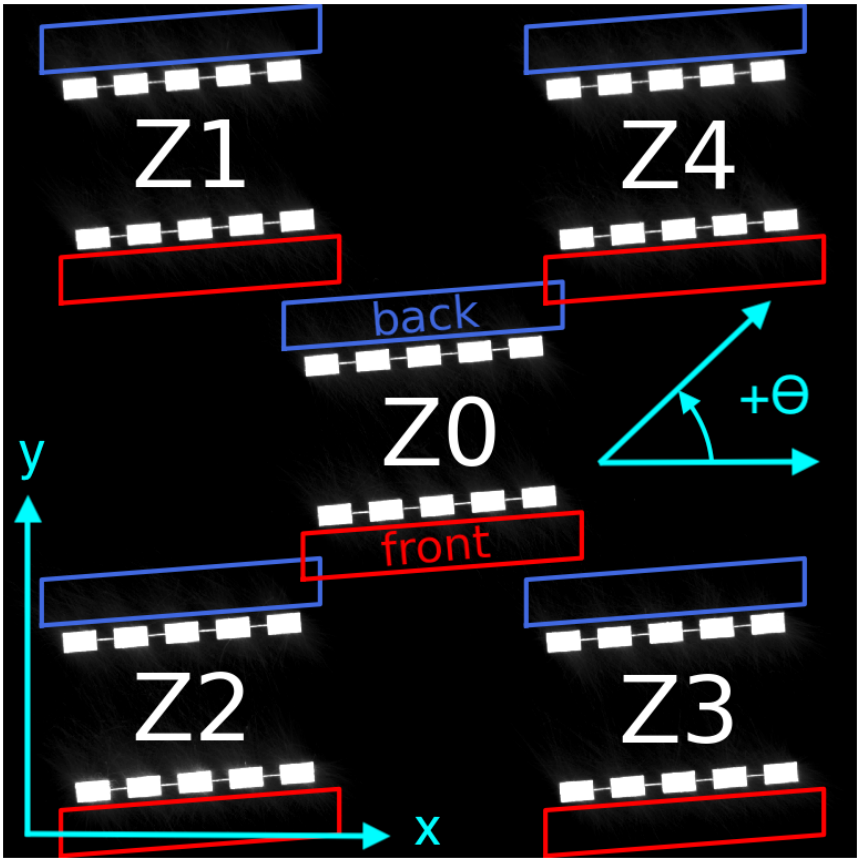

Figure 3.7: Regions Of Interest (ROIs) identified within the build space. Front zones shown in red, back zones shown in blue.

3.5.1 Direction of spatter trajectories

The orientation of spatter features was examined using the OrientationJ [61] plugin for ImageJ [62]. The algorithm determines an orientation for each pixel in the image by comparing the grayscale intensity of the pixel to the grayscale intensity of nearby pixels and identifying the direction of minimum change in grayscale intensity. The direction of spatter is reported as an angle between -90° and 90°. For the analysis in this study, the dominant direction of spatter was determined for each of the 10 ROIs in a sample of 24 sequential OT images. Since the scan angle increments by 67° with each build layer, the resulting data captures variation in the dominant direction of spatter as a function of scan angle.

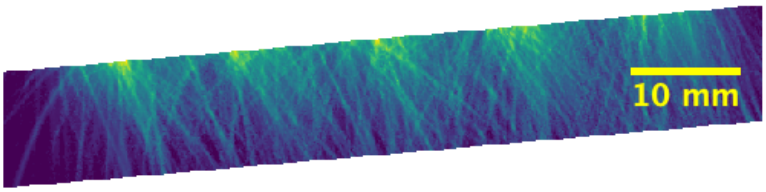

(a) original

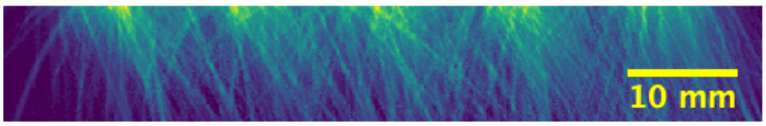

(b) reshaped

Figure 3.8: Details concerning the image processing in the region of interest. (a): Original ROI. (b): Reshaped ROI.

Figure 3.9 shows a histogram of spatter orientation for an ROI along with a Gaussian fit for representative data produced from OT images for Build 6 performed with GA powder. To facilitate plotting and analysis, the histogram data was rotated so that the peak values were in the center of the plotting domain. Bin values were shifted accordingly (i.e. if rotating to the right, as shown in Figure 3.9, the rightmost bin would be rotated to the left side of the histogram and 180° subtracted from the bin value.) As evident in the histogram, the mean angle of spatter ray for this ROI is -100° and the standard deviation is 19.7°.

Figure 3.10 shows a plot of spatter angle peak vs. scan angle for Zone 0, including both the front and back ROIs. Each point represents the peak spatter ray angle of a ROI, and the error bar on the point is one standard deviation. As evident in the figure, there is a correlation between the peak spatter angle with scan angle. A unity line (spatter angle = scan angle) is also plotted to aid in comparing the spatter angle to the scan angle.

Figure 3.11 shows the data presented in Figure 3.10, except that the difference between the peak spatter angle and the scan angle is plotted on the vertical axis rather than the spatter angle. The horizontal axis remains as the scan angle. As evident in the figure, there is a "flattening" of the trend that facilitates clearer identification of variations. Points near the x-axis indicate that

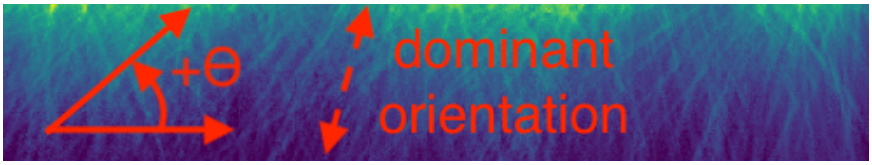

(a) ROI image

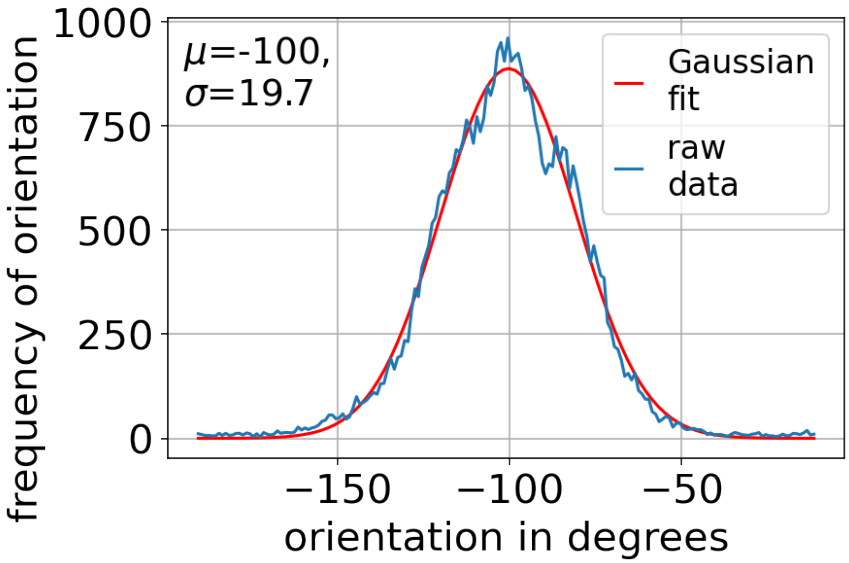

(b) Histogram for ROI

Figure 3.9: Details for post-processing of the OT images for spatter characteristics. (a) ROI image, indicating dominant direction of spatter. (b) Histogram for orientation in a spatter ROI with curve fit.

the scan angle is close to the spatter angle, and points above or below the x-axis indicate that the spatter angle is greater than or less than the scan angle, respectively. There are a couple noteworthy features of this plot. When the scan angle is close to 0° there is a jump in an otherwise roughly linear trend. The uncertainty is also largest in the vicinity of where the scan angle is equal to zero.

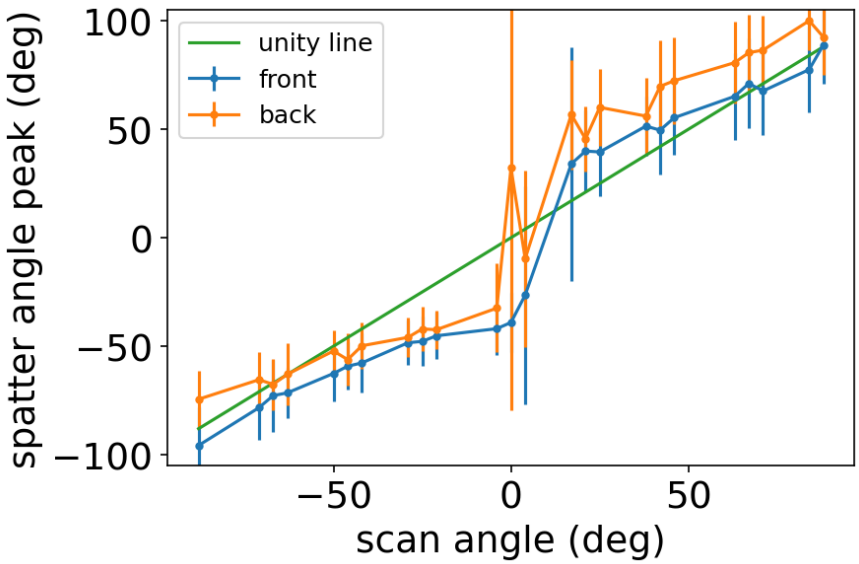

Figure 3.10: Peak spatter angle plotted as a function of scan angle for Zone 0.

According to the distribution in Figure 3.11, the difference between the spatter angle and scan angle response exhibits two characteristic sections. There is a stable section with cohesive data points and low to moderate uncertainty that spans most of the domain. In these layers the spatter signatures were coherent and the histogram showed a narrow angle distribution, akin to that in Figure 3.10, which was well represented by a Gaussian model. There is also a sharp jump in the distribution around 0°, with irregularly spaced points and high uncertainty. The histograms for ROIs with scan angles close to 0° typically exhibited high variability or did not follow a Gaussian form, indicated by a high uncertainty in the curve fit.

While scan angle could drive the primary direction of spatter particle ejection, gas flow is expected to contribute to changes in the direction of particle velocity within its period of flight. A schematic description of this mechanism is illustrated in Figure 3.12. If spatter is ejected at an oblique angle with respect to the direction of gas flow, the gas flow acts to bring the direction of particle motion coincident with the direction of the gas flow. In contrast, if the direction of motion (spatter ejection angle) is not changing from the direction the particle was ejected, (scan angle) the gas and spatter must be parallel. Hence, the predominant direction of gas flow at a location

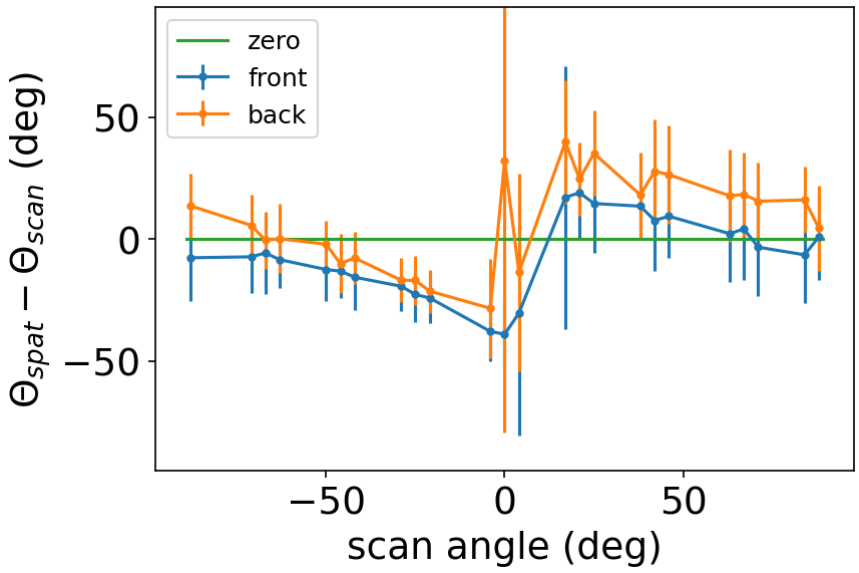

Figure 3.11: Peak spatter angle difference from scan angle for Zone 0. Note the large extent of uncertainty in the region where the scan angle = 0°.

of interest can be inferred from the orientation at which spatter angle and scan angle are parallel according to whether there is diversion or curvature in the spatter ray in the x-y plane.

Since the algorithm that determines the orientation of spatter signatures in the ROI images is indiscriminate of the direction of travel of spatter particles, the scan angle can be offset by ± 180° and still represent the same information. Rotating the plot in Figure 3.11 so that both of the coherent, or linear sections on either side of the erratic section appear uninterrupted results in a more clear trend as shown in Figure 3.13. The coherent and erratic regions of the spatter angle difference data are identified in Figure 3.14, to be used in further discussion. In Figure 3.15, a linear fit was applied to the linear region of the Zone 0 data to quantify a relationship that could be applied across zones and builds. Similar data for Zones 1 through 4 can be seen in Figure C.1.

The interpolated x-intercept in Figure 3.16 identifies where scan angle is equal to spatter angle, which provides an estimate of the gas flow direction within an ROI. The uncertainty in the intercept is derived from the uncertainty in the fit parameters in worst-case scenarios.

The points in the erratic region can be used to characterize the range of scan angles for which

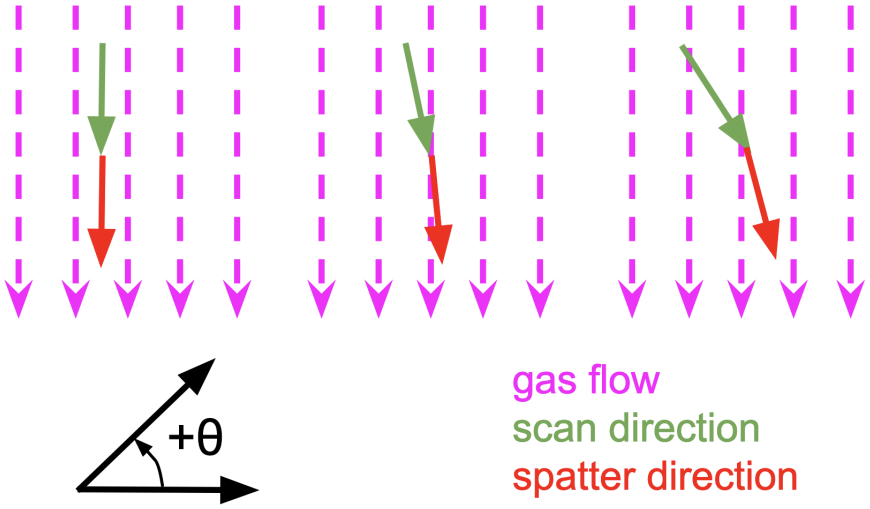

Figure 3.12: Schematic representation of gas flow influencing spatter motion.

the spatter trajectories are incoherent. High directional variability in spatter trajectories may be related to turbulent gas flow. A linear fit will be applied to these points.

3.5.2 Area Intensity

During the course of this study, it was made apparent that the OT images exhibit a distance from camera grayscale intensity variation that results in higher local grayscale intensity near the center of the image, and diminishing grayscale intensity further from the center of the image. Using a method that strives to normalize variations in grayscale intensity, detailed in Appendix B, a correction was performed on the OT images and the inter-specimen intensity analysis repeated. The results presented in this section have been produced using data corrected in this manner.

Spatial variation in the grayscale intensity of spatter was examined and a comparison of the intensity in select inter-specimen regions (ISR) is shown in Figure 3.17. The ISRs are 3.75 mm square. Variation in grayscale intensity with respect to scan angle, as well as with respect to distance from the specimens was evaluated using this approach.

The average grayscale intensity observed in the ISRs is less saturated than the average intensity adjacent to the specimens. As a result, changes in the intensity will be easier to observe in the ISRs

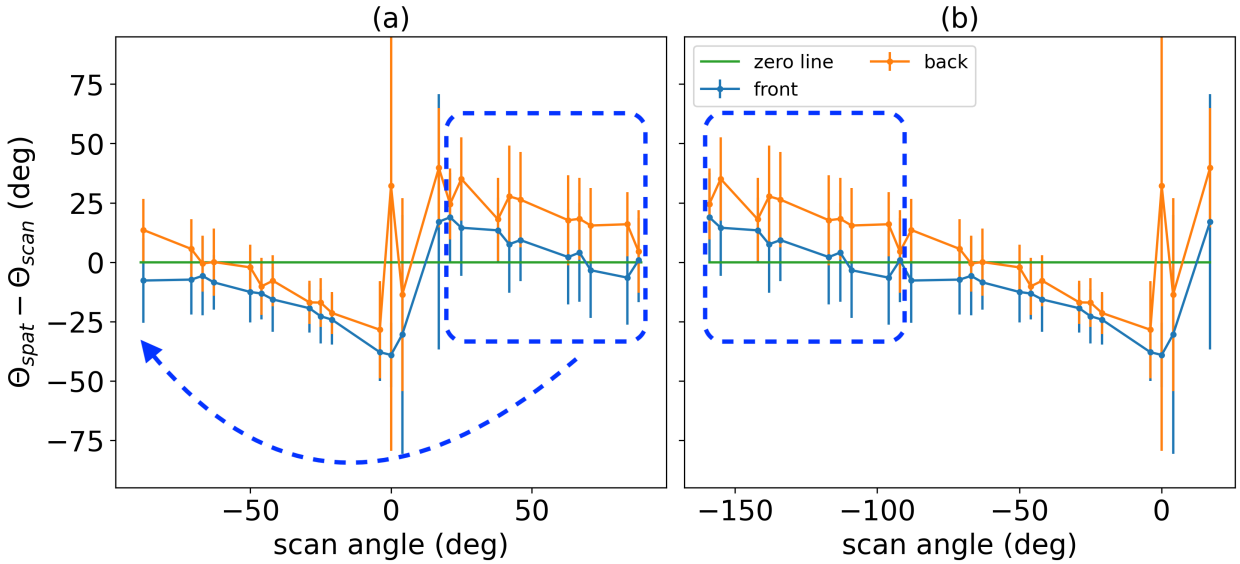

Figure 3.13: Domain rotation method for spatter angle difference from scan angle analysis. This shows the spatter angle difference from scan angle plot for Zone 0 both (a) prior to, and (b) following domain rotation.

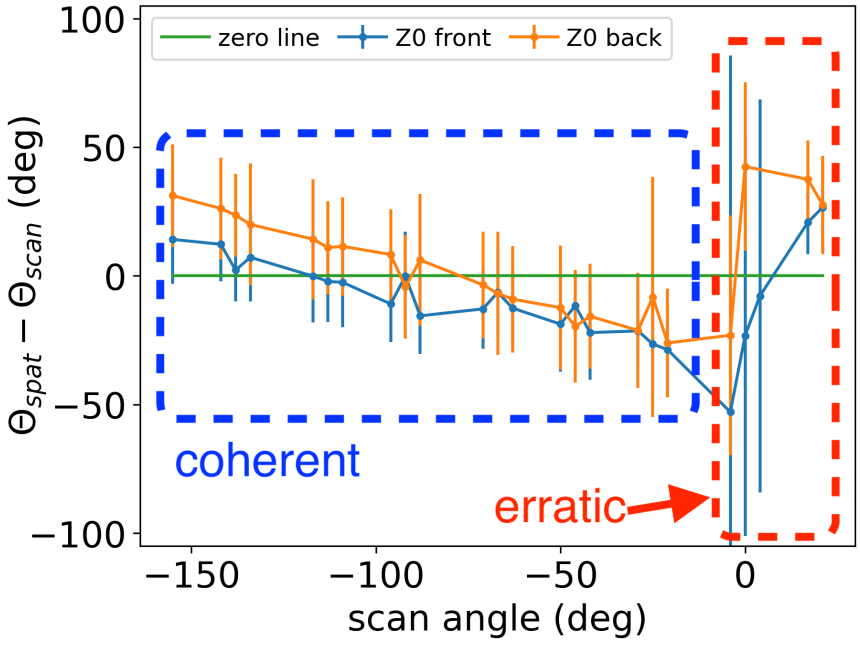

Figure 3.14: Coherent and erratic regions of the spatter angle difference data for Zone 0.

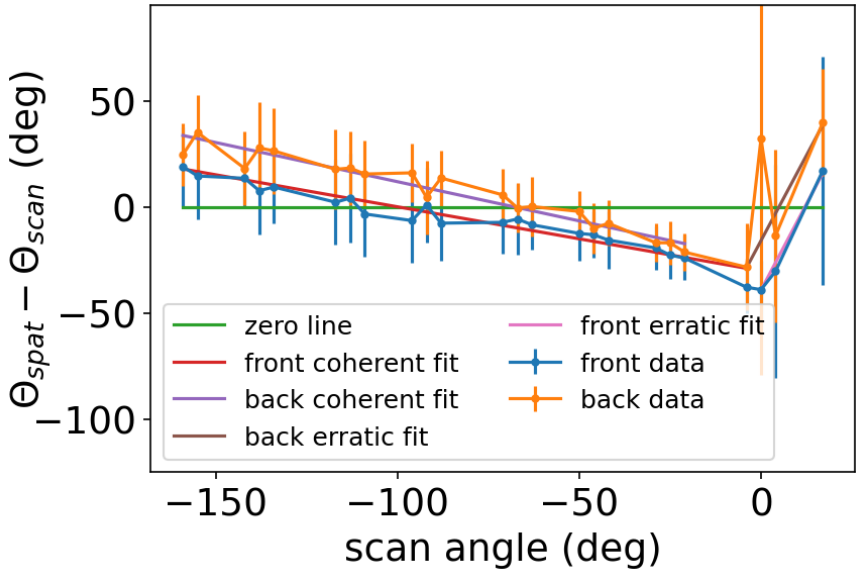

Figure 3.15: Linear fit for the direction of the spatter trajectories in Zone 0 in terms of the scan angle data. The domain of the data has been rotated so the linear regions can be presented uninterrupted. This data includes the spatter in the front and back ROIs.

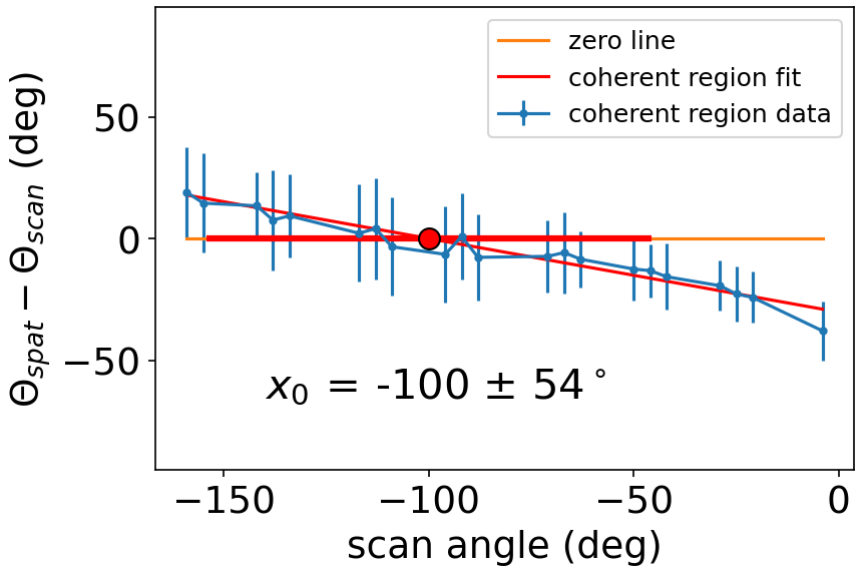

Figure 3.16: Linear fit of the spatter angle data for the front region of Zone 0 and the interpolated x-intercept.

than adjacent to the specimens. In addition, the inert gas flow acts to move spatter from where it originates at the specimens towards the outlet in the -y direction, away from the ISRs. If spatter motion was defined only by the force of the inert gas flow, spatter would only travel in straight lines parallel to the y-axis from the location of ejection towards the gas outlet. Any spatter that appears in the inter-specimen regions indicates the influence an ejection force, or another force other than gas flow. The grayscale intensity in the ISRs was initially evaluated in terms of the scan angle as shown in Figure 3.17. Briefly, the OT images were analyzed using an ImageJ macro where the average grayscale intensity in the ISRs i1-i4 (Figure 3.17) was measured. Then, the results from each location were averaged to provide an average inter-specimen intensity measurement for each layer. ISRs i0 and i5 were omitted for this analysis but were included in a subsequent analysis.

The results obtained by examining inter-specimen grayscale intensity revealed intensity minima at certain scan angles. Variations in spatter intensity will be more apparent under conditions when the average intensity is the lowest. As such, the observation of intensity minima at certain scan angles provides an opportunity to further examine inter-specimen grayscale intensity by assess-

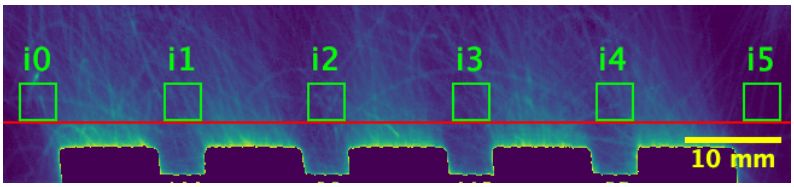

(a) back ROI ISRs

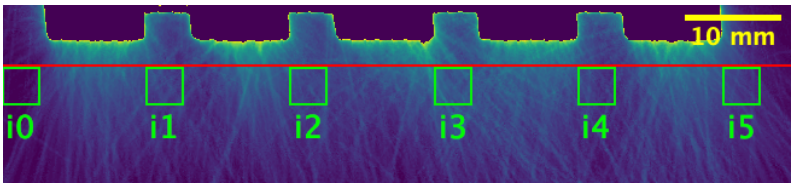

(b) front ROI ISRs

Figure 3.17: (a): Identification of inter-specimen regions (ISR) for back ROIs, Zone 0 shown. The area above the red line is not part of the ROI but included to show specimen locations. (b): Identification of inter-specimen regions (ISR) for front ROIs. The area below the red line is not part of the ROI but included to show specimen locations.

ing variations in grayscale intensity at the angle(s) of minimum average intensity. The grayscale intensity of spatter was also evaluated with respect to distance from the specimens by measuring the intensity in a series of smaller regions. The sub-ISRs, identified as such to distinguish them from the square ISRs defined in Figure 3.17, are distributed outward from the interior edges of the ROIs. By discretizing the ROIs in this manner, a higher spatial fidelity was achieved. The average grayscale intensity was measured for each sub-ISR in an individual layer, and the measurements were repeated for a series of sub-ISRs with increasing distances from the specimens, as shown in Figure 3.18. The variable distance from specimen inter-specimen grayscale intensity analysis was performed for a small number of select layer orientations only, rather than all layer orientations. Specifically, scan angles likely to exhibit greatest variation in grayscale intensity were chosen.

3.5.3 Comparison to Specimen Porosity

To pursue an identification of correlations between the spatter and porosity of the tensile specimens, a group of specimen spatter regions (SSR) were defined for the purpose of evaluating the grayscale intensity of spatter adjacent to the specimens. Selected areas were defined to quantify the average and standard deviation in grayscale intensity, and the maximum grayscale intensity, as shown in Figure 3.19 and 3.20. As evident in these two figures, 10 SSRs are defined corresponding to the 10 vertical specimens in each Zone; the SSRs s1 to s5 correspond to the back ROIs and s6 to s10 correspond to the front ROIs.

A smaller region was used to evaluate the average and standard deviation in grayscale intensity

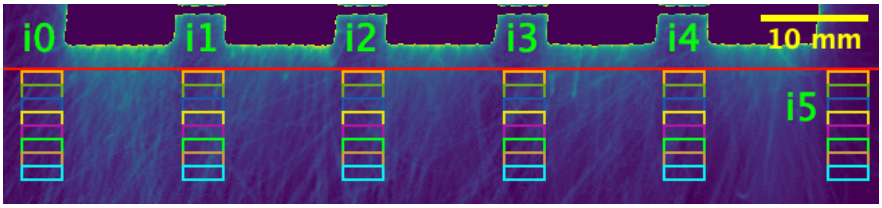

Figure 3.18: A description of the sub-inter-specimen regions (sub-ISRs) used to evaluate grayscale intensity as a function of distance from the printed tensile specimens of the build.

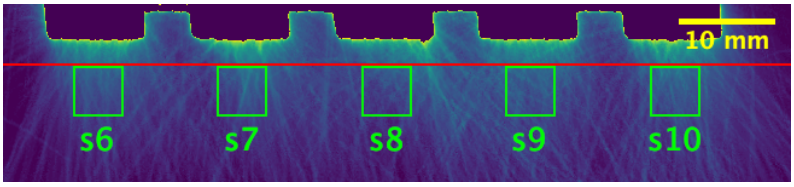

(a) SSRs for front ROIs

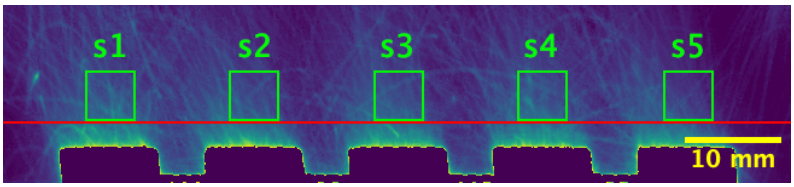

(b) SSRs for back ROIs

Figure 3.19: Identification of specimen spatter regions (SSR) for measuring average and standard deviation in grayscale intensity.

than that used to assess the maximum; these regions were 5 mm square in comparison to 12.5 mm square. The smaller area provides a better representation of spatter content limited to the specimen, and minimizes the influence of spatter generated from adjacent specimens. The smaller area also better represents the intensity of the spatter before it cools during flight and the observed intensity diminishes.

It was found that high intensity spatter features can appear as far as 8 mm or more from the meltpool of a specimen. Therefore, a larger region was used to evaluate the maximum grayscale intensity of the spatter than that used for average and standard deviation. These larger regions were 12.5 mm square. Because the "adjacent to specimen" spatter areas are larger than the areas used in evaluating the inter-specimen intensities, direct comparisons between these two grayscale intensity measures cannot be made. In addition, spatter is more abundant in the vicinity of the SSRs, in comparison to the ISRs, and so the observed grayscale intensity will likely be higher. Nevertheless, the SSRs provide a relevant representation of spatter generated during laser-powder-meltpool dynamics in printing of the specimens.

The spatter metrics for spatter content including average, standard deviation, and maximum

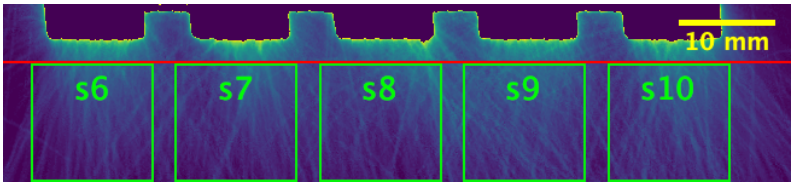

(a) SSRs for front ROIs

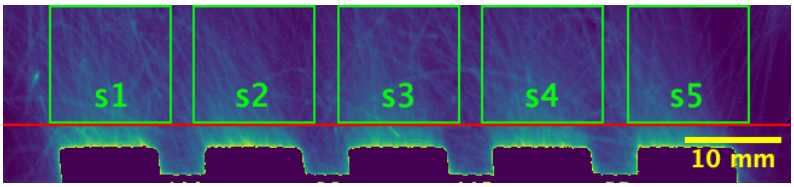

(b) SSRs for back ROIs

Figure 3.20: Identification of specimen spatter regions (SSR) for measuring maximum grayscale intensity.

grayscale intensity were evaluated for a selection of layers spanning the gauge section of the specimens, which spans approximately 500 layers. As a consequence, the dataset was limited to layers for which the scan angle was within 6 degrees of the y-axis (i.e. predominately in the direction of gas flow). With this restriction, the reduced number of layers consisted of about 30 images. Also of note, the grayscale intensity data for the A and B level specimens was evaluated separately, for a total of about 60 images per build.

The grayscale intensity of spatter in the SSR adjacent to each specimen was measured using an ImageJ macro. The following process was used for measuring the grayscale intensity of each image:

1. A Zone is selected from the layer of interest.

2. The average grayscale intensity, the standard deviation and maximum grayscale intensity for each of the 10 SSRs in that zone are measured.

3. The previous step is repeated for each of the 5 zones in the layer, for a total of 50 SSRs, one for each vertical specimen.

4. This process is repeated for each of the layers in the dataset. Note that the dataset comprises the range of layers spanning a single level. The layers corresponding to the second level are analyzed separately, as the second level corresponds to a separate set of 50 specimens.

5. Values for average grayscale intensity and standard deviation are averaged across layers, for each specimen. The maximum grayscale intensity is taken as the highest value across all layers in the dataset for each specimen.

6. The average grayscale intensity, standard deviation in grayscale intensity, and maximum grayscale intensity for each specimen are stored for further analysis.

μCT characterization of porosity

Porosity data was obtained from μCT scans of each tensile specimen. The μCT scanning was performed with an NSI Model X5000 imaging system, using a source energy of 204 kV and 44 μA [15]. A total of 5760 projections were captured at a rate of 2 frames/second using a helical scan path spanning the gauge section of the specimen, resulting in a voxel size of approximately 8 μm [15].

After reconstructing the scans, the resulting volumes were analyzed using the software package VGStudioMax [63] and the VGdefxOnlyThreshold porosity analysis algorithm. The μCT post-processing and analysis was performed to identify the pores in the specimen, and produced a set of metrics for each pore, including diameter, sphericity, distance from the nearest free surface, cross-sectional area, and other geometric attributes. The mean and coefficient of variation (standard deviation divided by mean) for pore diameter and sphericity were evaluated for the set of pores in each specimen. These statistical measures of porosity were then compared to the average, standard deviation, and maximum grayscale intensity of spatter content to investigate if there are relationships between spatter content and porosity.

Chapter 4. RESULTS

4.1 Direction of spatter trajectories

The direction of spatter emission was evaluated from the OT images according to the trajectory of the grayscale emission tracks. The angle of trajectory was estimated with respect to the scan angle for each ROI and in each layer. A representative distribution for the spatter angle and spatter scan angle difference vs. scan angle are shown for Zone 0 in Figures 4.1 (a) and 4.1 (b), respectively. These distributions were generated for a LPBF build performed with GA powder. Details of the treatments used in evaluating the spatter trajectory was described in Chapter 3.

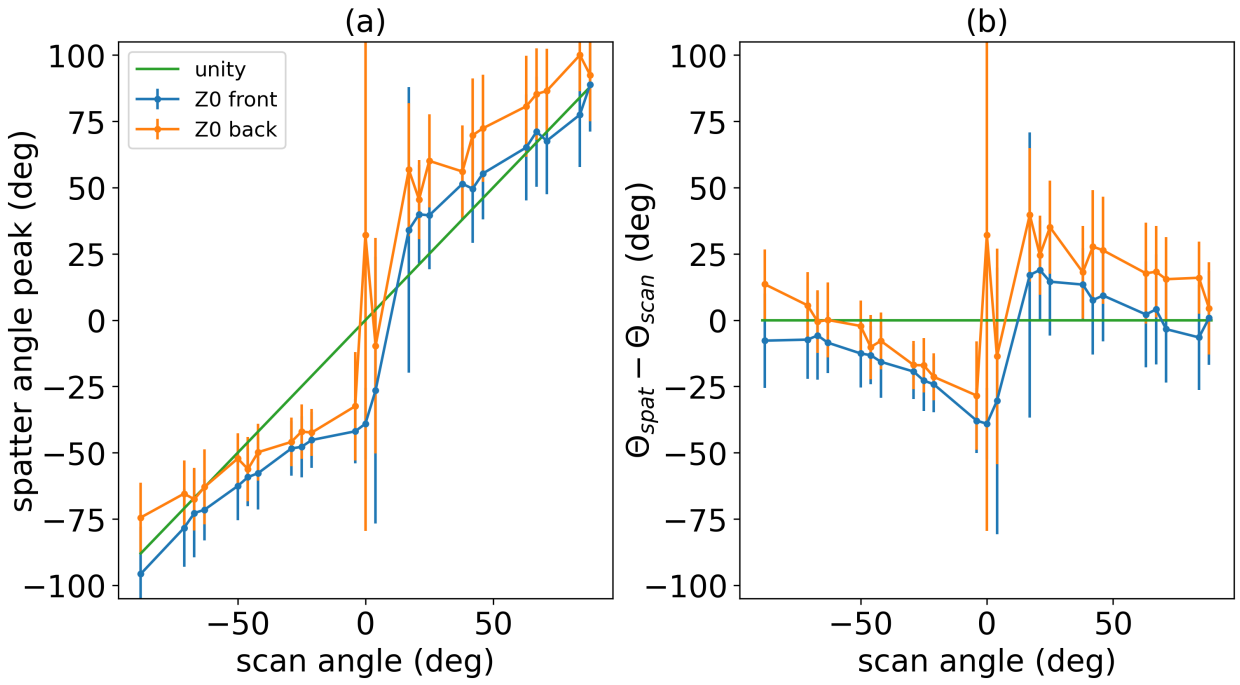

Figure 4.1: Results for (a) peak spatter angle and (b) spatter scan angle difference as a function of scan angle for Zone 0, for a build performed with **GA powder**. A scan angle of 0° is parallel to the x axis. This shows a coherent, linear relationship between spatter angle and scan angle for most of the angle range, except for an erratic region near 0°. Results are shown for both the back (towards the gas inlet) and the front (towards the operator.)

Figure 4.2 shows results of the form shown in Figure 4.1 (b) for Zones 1 to 4, and for a build performed with **GA powder**. In this figure the plots are arranged counter-clockwise from top left with Zones 1 to 4 shown in Figure 4.2 (a) to Figure 4.2 (d), respectively. This approach to presentation is consistent with the arrangement of the zones in the build space that are used in referring to the specimen clusters in the UW-Boeing Round Robin program [15]. As evident in Figure 4.2, Zones 1 to 4 exhibit a linear trend for the majority of the range in scan angle except for the region near 0°.

A linear fit was applied to the regions of the spatter angle difference plots that exhibited coherency, and linear fits were applied separately to the erratic portion near 0°, as shown in Figure 3.15. In both cases, the slope represents the ratio of change in spatter angle difference (°) to change in scan angle (°). Thus, the dimension of the slope is degrees per degree or unitless. The magnitude of both of these slopes provides a measure of deflection from the direction of ejection due to the influence of the gas flow. Measures of the best-fit slopes for these two regions are presented in Figures 4.3 and 4.4, respectively; the numeric values are listed in Tables C.1 and C.2, respectively, of Appendix C. In Figure C.2, Zone 1 exhibits a particularly high value for the slope due to the narrow width of the region near 0°. This behavior suggests comparatively high gas flow in this region. Note that while the slope in the linear regions is negative, the absolute value of the slope is plotted in Figures 4.3 and 4.4 for easier interpretation.

As previously described, the gas flow direction within each ROI was estimated from the interpolated x-intercept of the spatter angle difference plot. The estimated gas flow direction for each of the 10 ROIs in the build space is presented in Table 4.1. This data is presented visually in Figure 4.5. Overall, a greater degree of spatter deflection occurs in the back as expected and evident from the greater deviation from 90°.

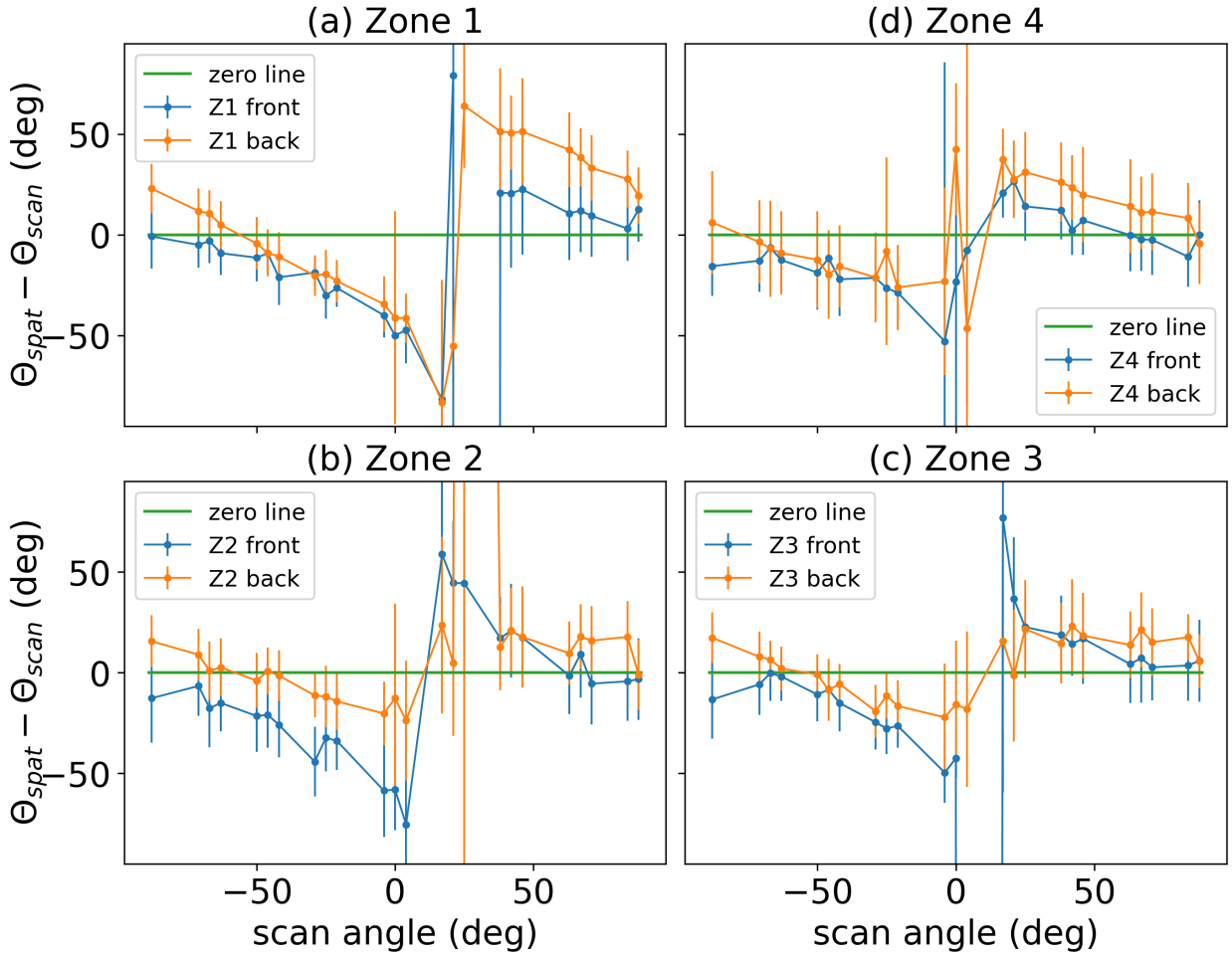

Figure 4.2: Difference between spatter angle and scan angle as a function of scan angle for Zones 1 to 4, labeled (a) to (d), respectively, for a build performed with **GA powder**. Results are shown for both the back (towards the gas inlet) and the front (towards the operator.)

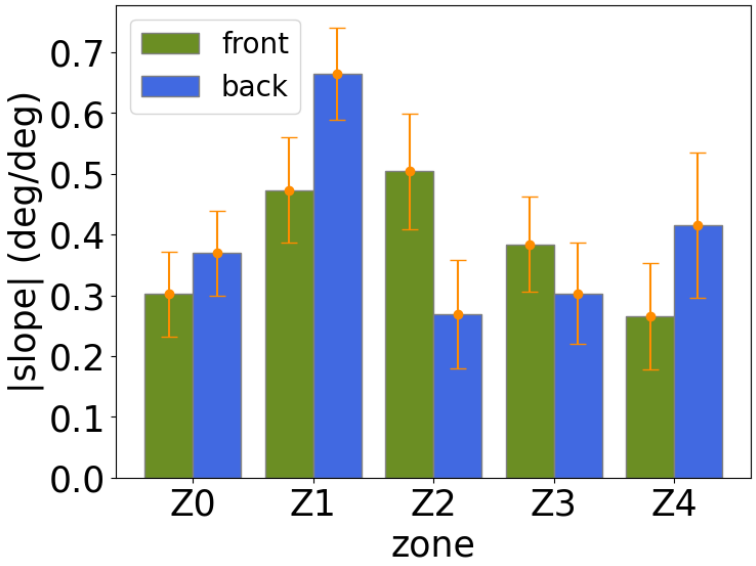

Figure 4.3: Absolute value of the slope of the coherent region of the spatter angle difference plots across Zones 0 to 4. The slope represents the height of the coherent regions of Figures 4.1 and 4.2 divided by the width of the same regions.

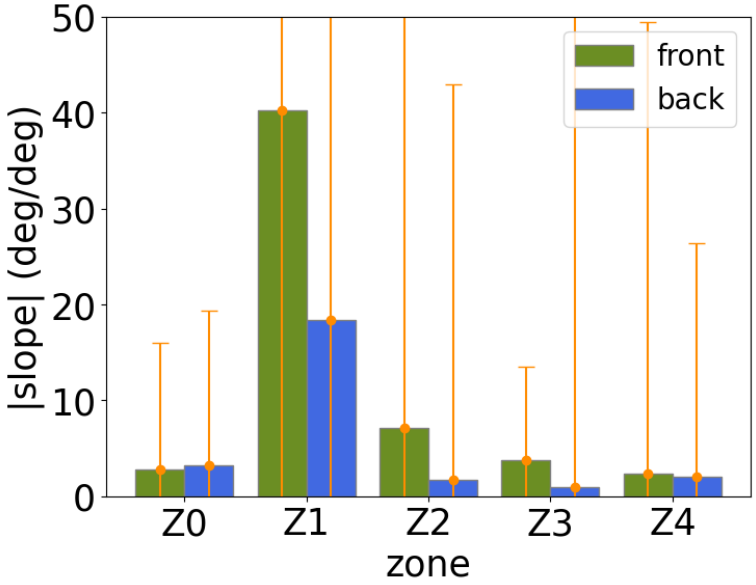

Figure 4.4: Absolute value of the slope of the erratic region of the spatter angle difference plots across Zones 0 to 4. The slope represents the height of the regions of Figures 4.1 and 4.2 near 0° divided by the width of the same regions.

Table 4.1: Estimated gas flow direction within the 5 Zones of the build plate by ROI. The trajectories of spatter ejected in these directions will not be deflected by the gas flow. An angle of 90° or −90° corresponds to gas flow parallel to the y axis and from the back to the front of machine.

zone	Front	Back
Z0	$-100 \pm 54°$	$-68 \pm 34°$
Z1	$-80 \pm 31°$	$-56 \pm 16°$
Z2	$-99 \pm 41°$	$-59 \pm 67°$
Z3	$-88 \pm 43°$	$-60 \pm 52°$
Z4	$-115 \pm 105°$	$-83 \pm 74°$

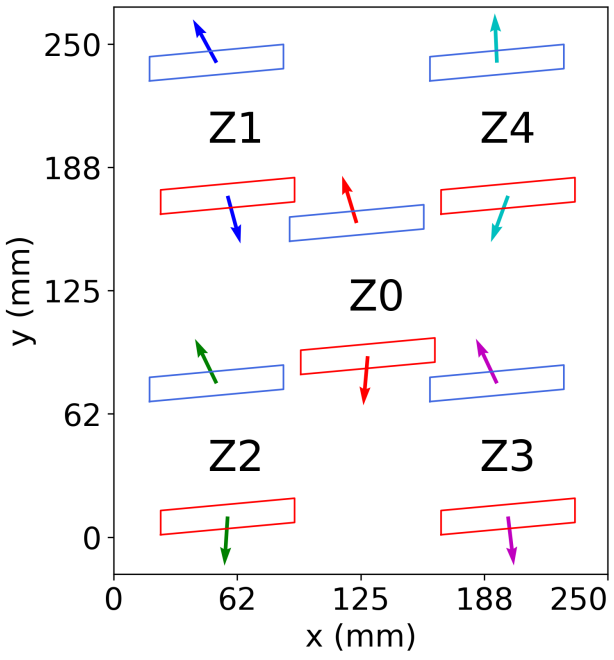

Figure 4.5: Estimated direction of gas flow in each ROI according to interpolation of the x-intercept of the spatter angle difference plots. This data was evaluated for a series of layers with varying scan angles. The trajectories of spatter ejected in these directions will not be deflected by the gas flow.

4.2 Area Intensity

4.2.1 Fixed Distance from Specimen

Figure 4.6 compares the average grayscale intensity in the (a) back and (b) front ROIs of Zone 0 as a function of scan angle for the builds performed using GA powder. The grayscale intensity for the back zones exhibits minima at 0° as well as at ±90°, and there are two maxima at ±45°. The front ROI shows a minimum grayscale intensity at a scan angle near 0°, and the grayscale intensity increases to a maximum at 90°, but there are no points of interest at ±45°. A similar comparison of the grayscale intensity distribution with scan angle is shown in Figure 4.7 for the builds performed using PA powder.

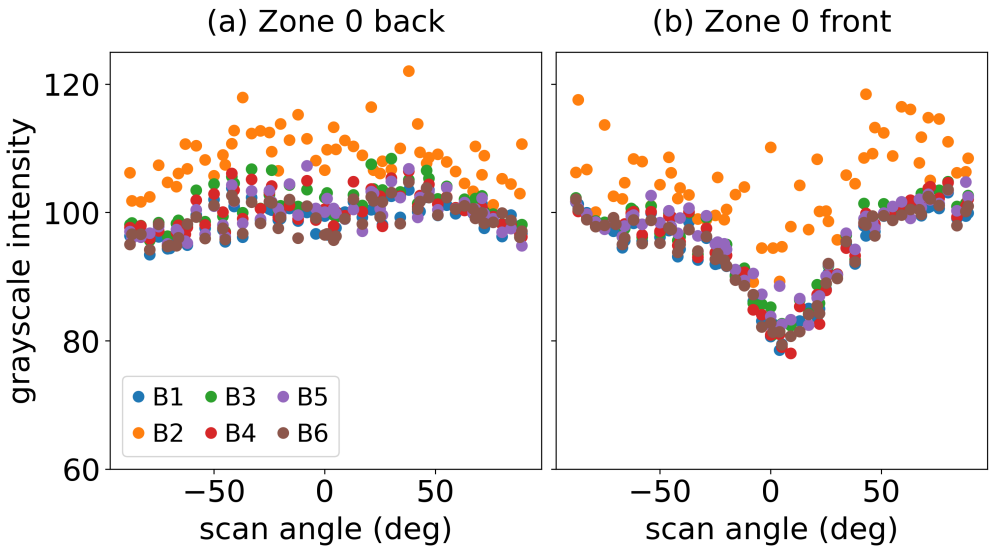

Figure 4.6: The distribution of inter-specimen grayscale intensity for the (a) back and (b) front regions of Zone 0, that resulted from the builds performed with **GA powder** and over the range in scan angles. The data presented here includes the grayscale intensity distributions for six builds.

Results for Zones 1 to 4 exhibit similar trends to those shown for Zone 0 in Figures 4.6 and 4.7. Note that while Zone 0 was printed in Builds 1 to 6, each of Zones 1 to 4 were printed in only 3

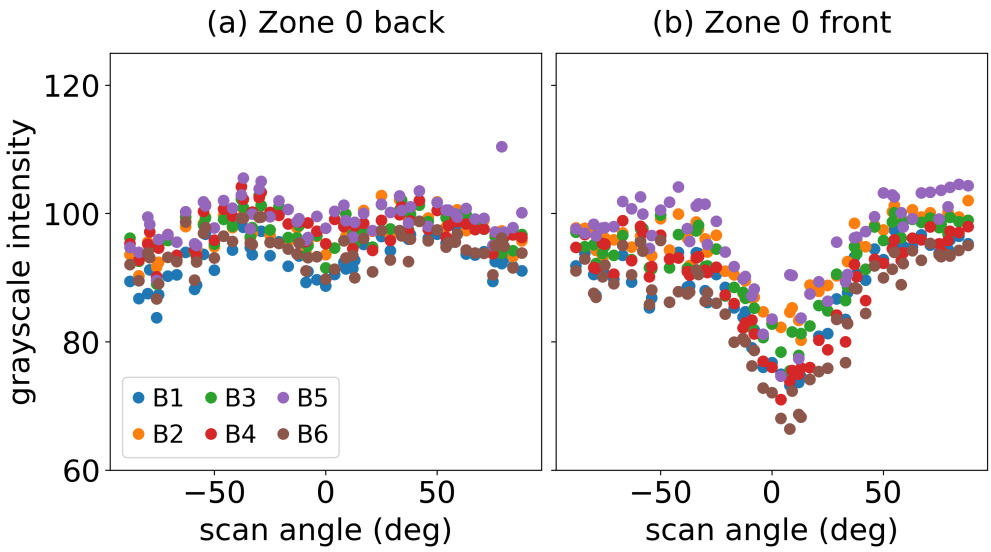

Figure 4.7: The distribution of inter-specimen grayscale intensity for the (a) back and (b) front regions of Zone 0, that resulted from the builds performed with **PA powder** and over the range in scan angles. The data presented here includes the grayscale intensity distributions for six builds.

builds, so the datasets for Zones 1 to 4 consist of 3 builds rather than 6. Table 3.1 provided details of the build and zone combinations.

Akin to Figure 4.7 for Zone 0, the grayscale intensity distribution for the back region of Zone 4 for the builds produced with GA powder is shown in Figure 4.8 (a); there is a clear bi-modal intensity distribution with respect to scan angle. The same distribution as that shown in Figure 4.8 is presented for the builds produced using PA powder in Figure 4.9 (a). In this figure the bi-modal distribution is not nearly as pronounced, as there is more random variation in the data. Grayscale intensity distributions for Zones 1 to 4 that were generated during builds with GA and PA powder can be found in Appendix C, Figures C.2 to C.5.

Figure 4.10 compares the inter-specimen grayscale intensity for the back ROI of Zone 0 and for builds performed with GA and PA powder. Most evident in comparing the distributions in Figure 4.10 (a) and (b), the GA powder has a higher average grayscale intensity. In addition, there is noticeable scatter in the data from Build 2 with respect to the other builds. However, apart from Build 2, the grayscale intensity distribution resulting from the GA powder shows less variation over

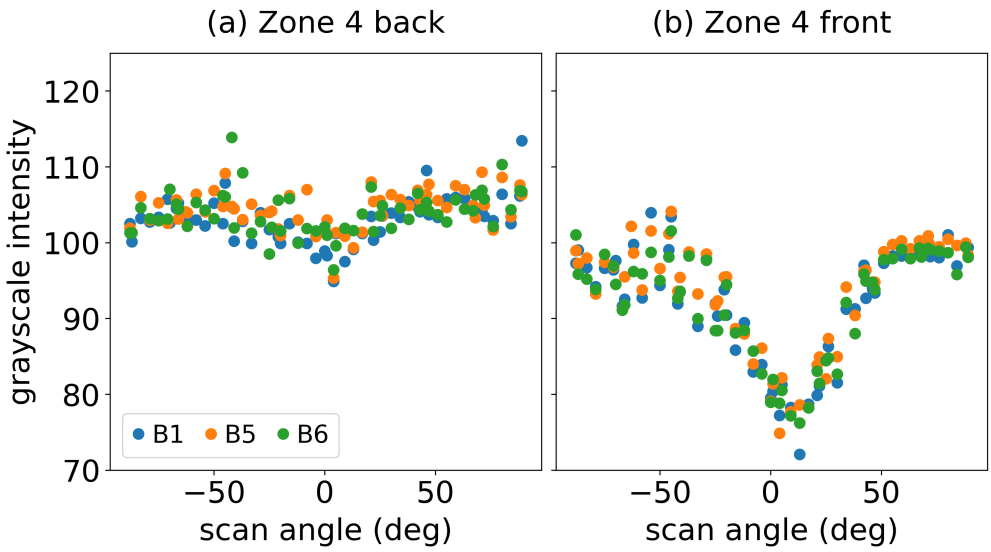

Figure 4.8: The distribution of inter-specimen grayscale intensity for the (a) back and (b) front regions of Zone 4, that resulted from the builds performed with **GA powder**. The data presented here includes the grayscale intensity distributions for Builds 1, 5, and 6.

the number of builds performed. The distribution within the same ROI for the PA powder shows more random variation, but still a trend similar to that exhibited by the GA powder as evident in Figure 4.10.

Figure 4.11 compares the inter-specimen grayscale intensity in the front region of Zone 0 as a function of scan angle for both GA and PA powders. The distribution is unique from that of the back ROI as it exhibits a clear trend with respect to scan angle. As observed earlier in Figure 4.10, the average grayscale intensity for the GA powder appears to be slightly higher than for the PA powder. In addition, apart from the larger relative variation in Build 2 performed with GA powder, the PA powder has greater random variation in grayscale intensity.

Figure 4.12 shows a comparison of the average inter-specimen grayscale intensity for each ROI by build. Results are presented for the gas atomized and plasma atomized powder in Figure 4.12 (a) and 4.12 (b), respectively. Through a comparison of this type, the trends in the data become more evident and the outliers can be more easily identified. For instance, the comparatively high average grayscale intensity is clearly evident in the results for Build 2 that was performed with the

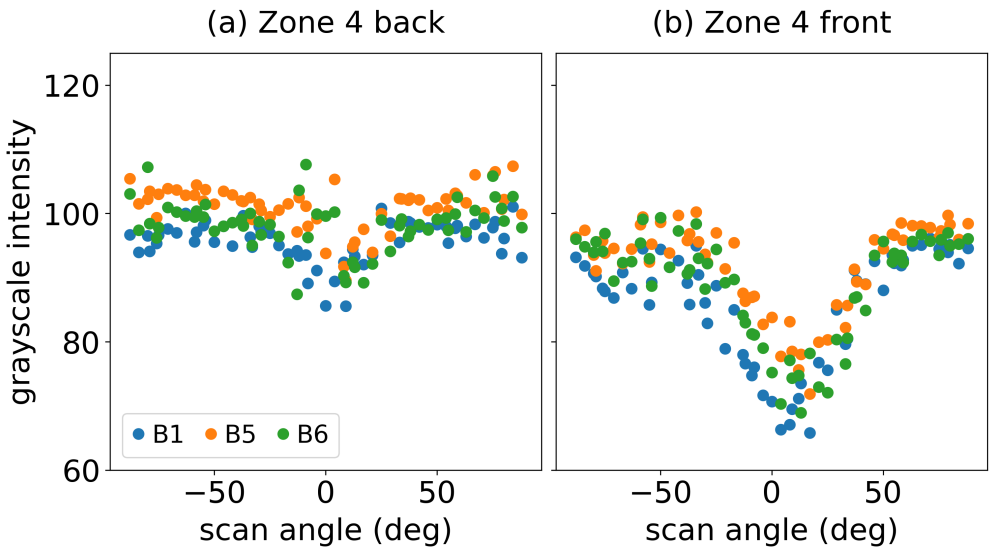

Figure 4.9: The distribution of inter-specimen grayscale intensity for the (a) back and (b) front regions of Zone 4, that resulted from the builds performed with **PA powder**. The data presented here includes the grayscale intensity distributions for Builds 1, 5, and 6.

GA powder. Contrary to expectations, the average inter-specimen grayscale intensity for the back ROIs is significantly greater than that of the front ROIs in builds performed with both GA and PA powder. That quality is most clear in the inter-build intensity averages for the front and back ROIs, which are denoted by the green and blue lines, respectively. Also important to note, the average grayscale intensities obtained for the GA powder are significantly higher (by approximately 30%) than those for the PA powder. That suggests that the GA powder results in a greater extent of spatter emission during the laser-powder interaction.

A comparison of the difference between the grayscale intensity from the back and front inter-specimen ROIs was performed as an alternate manner to identify spatial variation across the zones. Figure 4.13 shows a plot of the percent difference in average grayscale intensity between back and front ROIs for each of the five zones. As evident from these comparisons, the difference in average grayscale intensity between the back and front ROIs is largest in Zones 1 and 4, which are at the back of the print bed nearest the inert gas inlet grid nozzle. The grayscale intensity differences for Zones 0 (in the middle of the print bed) and Zones 2 and 3 (at the front of the print bed) are close to

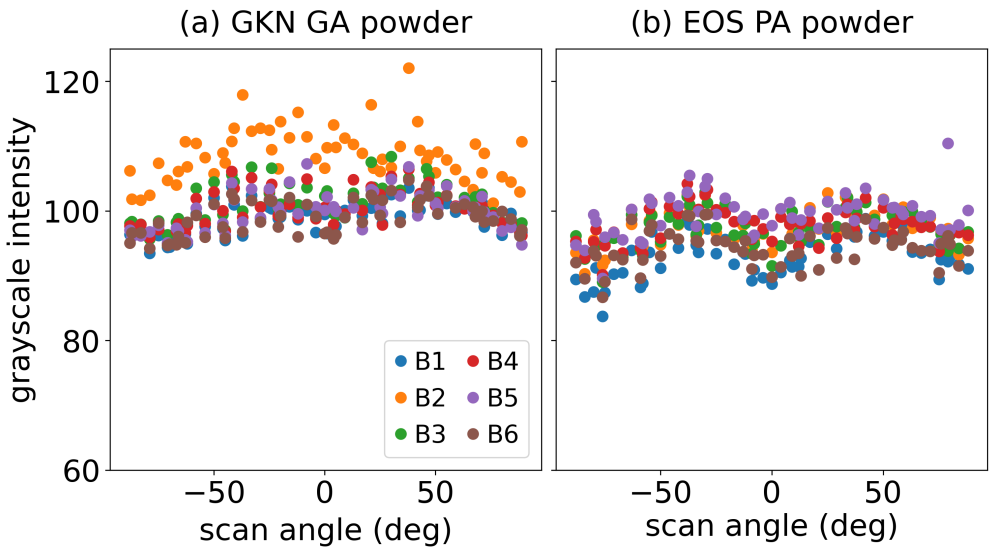

Figure 4.10: Comparison of the grayscale intensity within the back ROI of Zone 0 resulting from builds performed with the (a) GA and (b) PA powder.

zero for the builds performed with GA powder. However, for the PA powder the grayscale intensity difference for Zones 0, 2, and 3 are about half the difference for Zones 1 and 4 and much larger relative to the GA powder. Surprisingly, while the builds performed with GA powder exhibited an average inter-specimen grayscale intensity that was higher than that of the builds performed with PA powder, the percent difference in grayscale intensity between back and front ROIs is roughly equal for both the GA and PA powder in Zones 1 and 4.

4.2.2 Variation in spatter intensity with distance

Figure 4.14 shows the grayscale intensity behavior within the inter-specimen regions (ISRs) of Zone 0 as a function of distance from the specimen boundary; this data was generated in a build performed with PA powder and a scan angle of 0°. The intensity distributions are shown separately for the back and front regions in Figure 4.14 (a) and 4.14 (b), respectively. Note that the location of the ISRs is slightly offset in x between the back and front ROIs due to the 5° rotation of the specimen clusters on the build plate, which also applies to Zones 1 to 4. Clearly evident in this

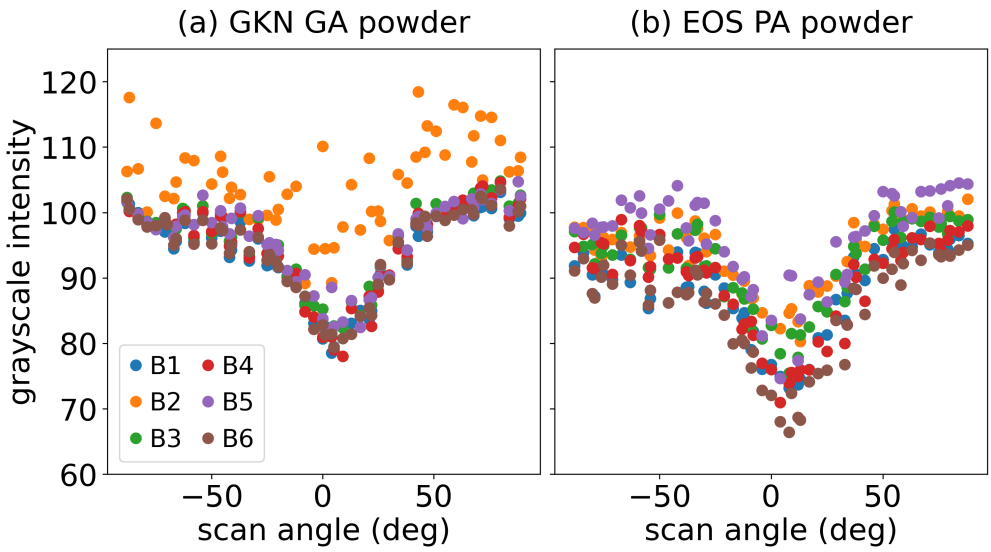

Figure 4.11: Comparison of the grayscale intensity within the front ROI of Zone 0 resulting from builds performed with the (a) GA and (b) PA powder.

distribution, there is a sharp decrease in the grayscale intensity with distance for both the back and front regions. In addition, the grayscale intensity adjacent to the specimens (i.e., distance from specimen = 0) for the back ROI is higher than for the front ROI. This is consistent with the average inter-specimen grayscale intensity measures presented in Figures 4.12 and 4.13. However, while the back ROIs exhibit higher inter-specimen grayscale intensity adjacent to the specimens, the grayscale intensity in the back ROI decreases more rapidly with increasing distance than for the front ROI. Indeed, spatter that is ejected into the back ROI is moving opposite the direction of gas flow. Drag forces will limit the distance it travels. In contrast, spatter ejected into the front ROI is travelling with the gas flow direction, resulting in spatter travelling longer distances before the observed grayscale intensity diminishes. For this study, the spatial variation in grayscale intensity of spatter was only characterized for the data obtained from builds performed with the PA powder. These spatial variations are expected to be consistent with those for GA powder as well.

The distribution in Figure 4.14 shows that for a scan angle of 0°, the inter-specimen grayscale intensity decreases rapidly, and in a nonlinear fashion with increasing distance from specimen. Consistent with the results of the average inter-specimen grayscale intensity difference between

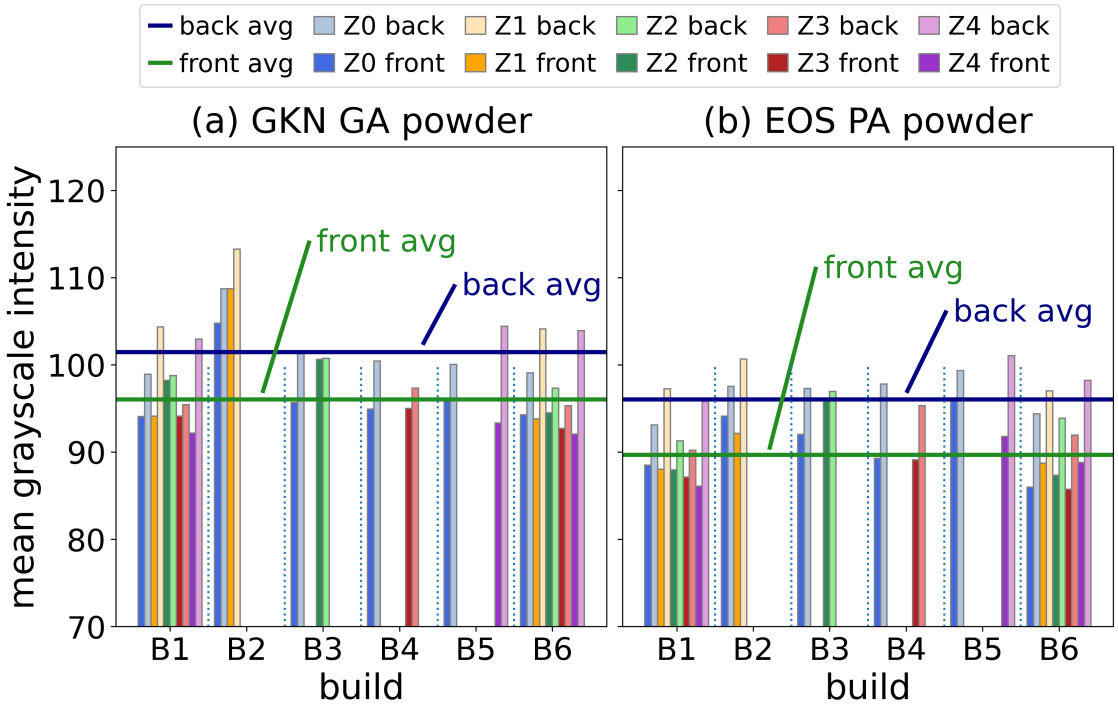

Figure 4.12: Comparison of the average inter-specimen grayscale intensity in spatter for builds performed with (a) GA and (b) PA powder. Both graphs show the average intensity for the front and back regions over the six builds.

the back and front ROIs, shown in Figure 4.13, the grayscale intensity adjacent to the specimens for the back ROI is higher than for the front ROI. Interestingly, the grayscale intensity adjacent to the specimens fluctuates with respect to the x axis in both the back and front ROIs in Figure 4.14. This variation could result from spatial irregularities in either gas flow or power delivered from the laser to the powder, or both. Similar to the distribution shown in Figure 4.14, the spatial distribution in inter-specimen grayscale intensity is shown in Zone 0 for a scan angle of 88° in Figure 4.15. The inter-specimen grayscale intensity distributions in Figures 4.6 and 4.7 showed that for a scan angle of 90°, the grayscale intensity in the back ROI is slightly less than it is in the front ROI. In Figure 4.15 it can also be seen that the inter-specimen grayscale intensity adjacent to the specimens is lower in the back ROI than in the front ROI, which is opposite to what was observed in Figure 4.14 at a scan angle of 0°. As evident from Figure 4.15, the grayscale intensity decreases with distance

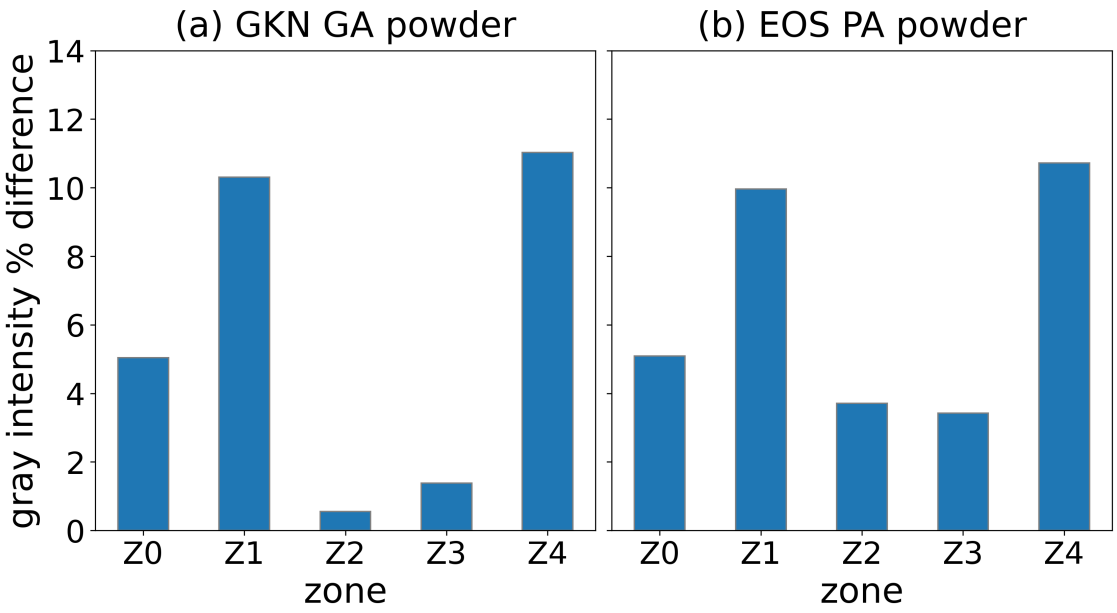

Figure 4.13: Difference in average inter-specimen grayscale intensity from the back and front ROIs for builds performed with the (a) GA and (b) PA powder. Note the larger differences in the intensity within Zones 1 and 4, which are near the gas inlet at the back of the machine.

but more gradually than noted previously for the 0° scan angle, as expected. In addition, the decay is more linear with increasing distance. Notably, the sub-ISRs corresponding to i5 for both the front and back ROIs exhibit nearly a constant level of grayscale intensity and limited variation with distance. It is possible that spatter generated in Zones 3 and 4 reaches these sub-ISRs, which are nearest the +x side of Zone 0. In the OT image for this layer there is indeed evidence that a considerable amount of spatter enters the Zone 0 back ROI from the Zone 4 front ROI. Similarly, spatter from Zone 3 back enters into Zone 0 front, though to a lesser degree, as shown in Figure 4.16. In addition, the grayscale intensity adjacent to the specimens does not exhibit the oscillation in +x that was observed for Zone 0 and a scan angle of 0° in Figure 4.14. Apparently, when the spatter is emitted from the melt pool with more momentum parallel to the gas flow, variations in the gas flow have less influence on the motion of spatter.

The grayscale intensity of the spatter documented in the back ROIs of Zones 1 to 4 is shown in Figure 4.17 (a) to (d), respectively. Note that the grayscale intensity adjacent to the specimens

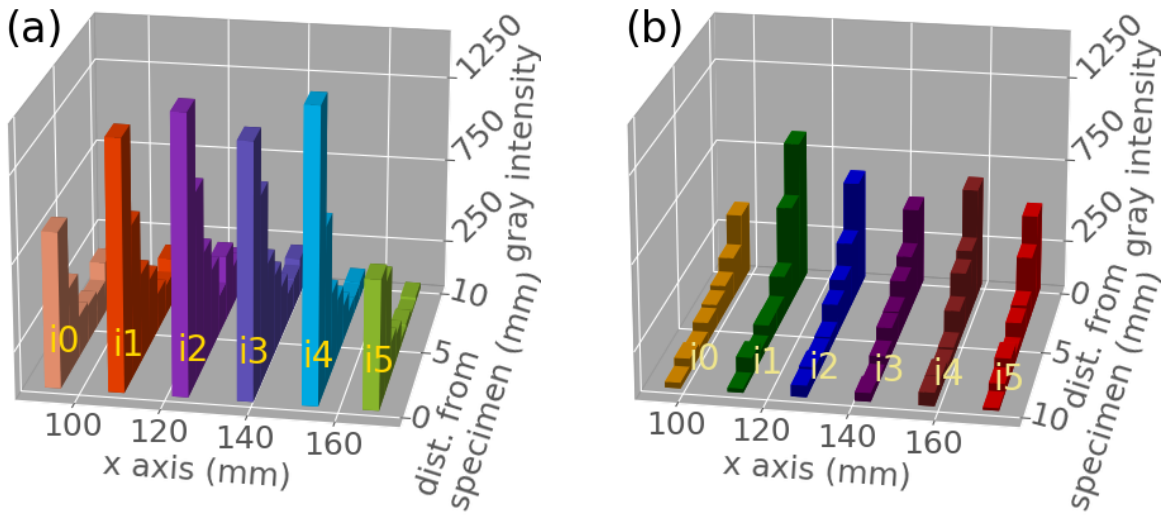

Figure 4.14: Spatial distribution in the inter-specimen grayscale intensity for Zone 0, and for a scan angle = 0°. Results for the (a) back and (b) front ROIs, that resulted from the builds performed with **PA powder**, are shown. This shows variation in grayscale intensity as a function of distance from the specimen, as well as for variation between the different sub-ISRs, labeled i0 to i5. Each color represents the grayscale intensity trend over distance from specimen for a single sub-ISR.

for the Zone 1 and Zone 4 ROIs in (a) and (d) is greater than that for Zone 2 and Zone 3, and that the grayscale intensity decreases rapidly and in a non-linear fashion with distance from the specimen. Zones 1 and 4 are located closest to the gas inlet nozzle. As such, the higher grayscale intensities could be related to a higher rate of gas flow or less stable flow nearest the gas nozzle. The results for Zones 1 and 4 as shown in Figures 4.17 and 4.18 are in agreement with the trends presented in Figure 4.13 in that the difference in grayscale intensity between the back and front ROIs is greatest in Zones 1 and 4, again, nearest the gas nozzle. The distributions in Zones 1 and 3 in Figure 4.18 (a) and (c), respectively also exhibit some oscillation in grayscale intensity with respect to the x-axis, similar to what was observed in Zone 4 in Figure 4.17 (d).

Figure 4.18 shows the grayscale intensity profiles in the front ROIs for Zones 1 to 4. These distributions have lower average intensity than in the back ROIs and show less variation between the five zones. The average grayscale intensity of the inter-specimen regions is approximately the

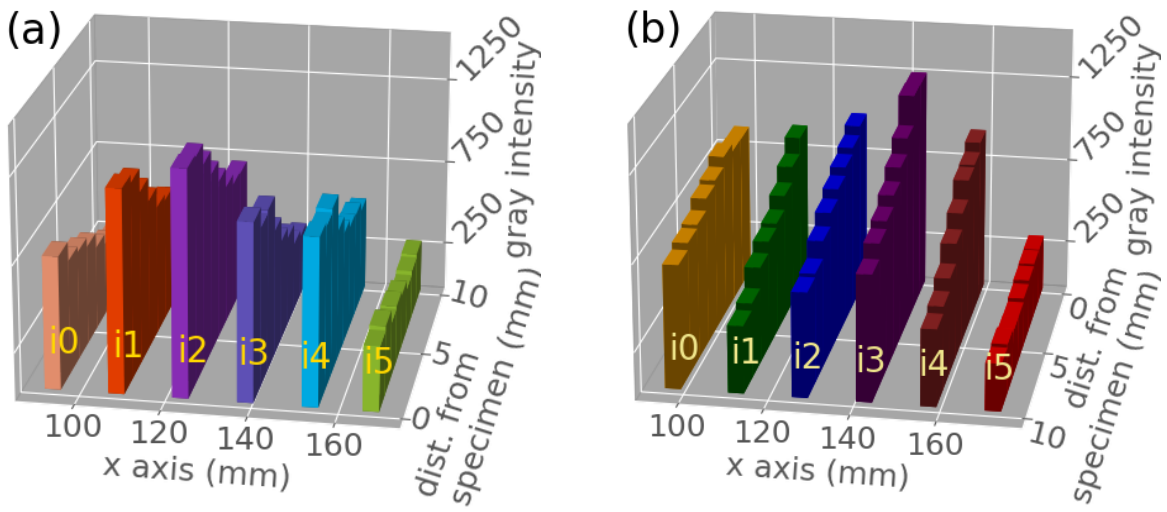

Figure 4.15: Spatial distribution in the inter-specimen grayscale intensity for Zone 0, and for a scan angle = 88°. Results for the (a) back and (b) front ROIs, that resulted from the builds performed with **PA powder**, are shown. This shows variation in grayscale intensity as a function of distance from the specimen, as well as for variation between the different sub-ISRs. Each color represents the grayscale intensity trend over distance from specimen for a single sub-ISR.

same for these 4 ROIs, and the grayscale intensity decreases in a manner similar to that observed in Figure 4.14. The grayscale intensity adjacent to the specimens is lowest in the front region of Zone 4, and highest for the front region of Zone 3, but the difference is small. Similar to the oscillation observed in Zone 0 (Figure 4.14) the grayscale intensity adjacent to the specimen in the front regions of Zones 1 and 3 oscillates with respect to the +x axis.

For completeness, results for Zones 1 through 4 corresponding to a scan angle of 88° can be found in Appendix C, Figures C.8 and C.9.

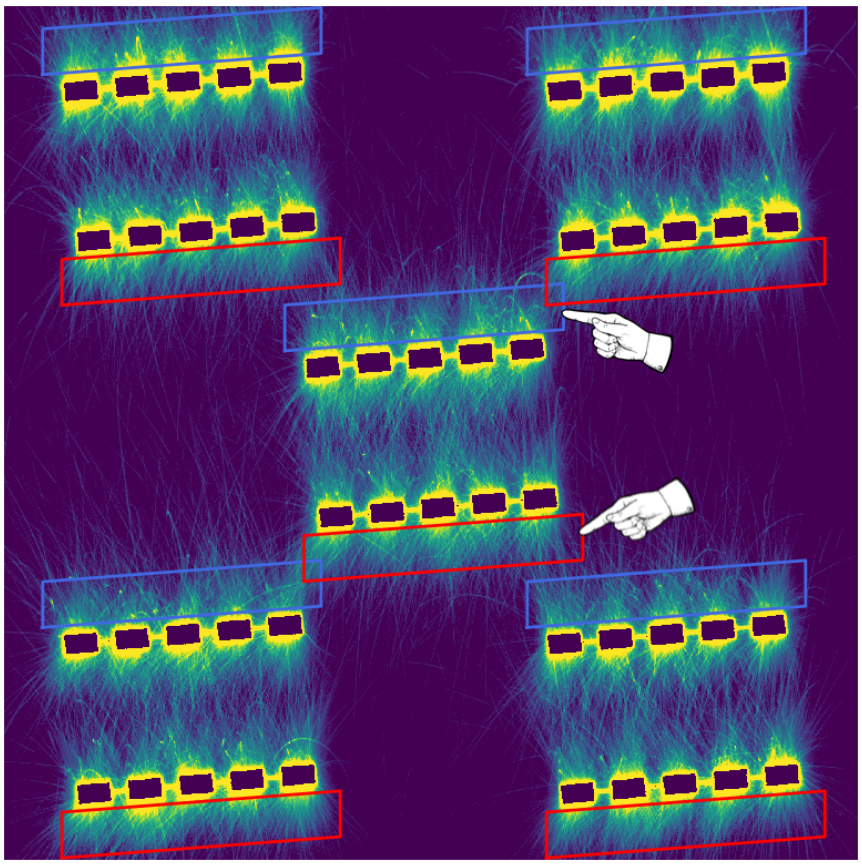

Figure 4.16: OT image for layer 3424 of Build 1 performed with PA powder, showing the presence of spatter in the Zone 0 ROIs that originated from the adjacent ROIs in Zones 3 and 4. ISRs i5 in both the back and front ROIs of Zone 0 are indicated. Brightness has been adjusted to highlight spatter features.

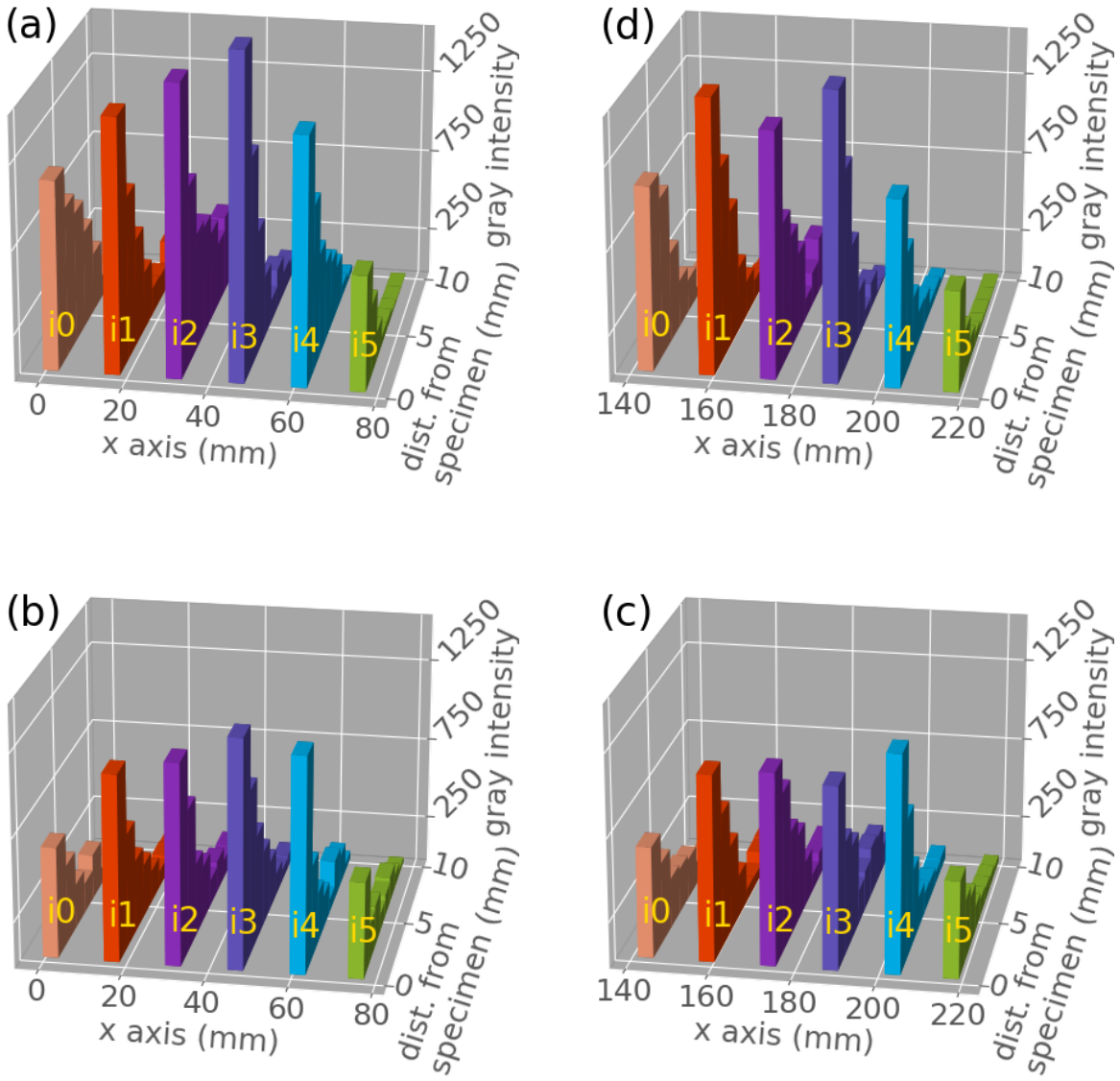

Figure 4.17: Inter-specimen grayscale intensity for Zones 1 to 4, shown in (a) to (d), respectively, in the back ROIs and in LPBF with a scan angle = 0°. This data is for builds produced with **PA powder**.

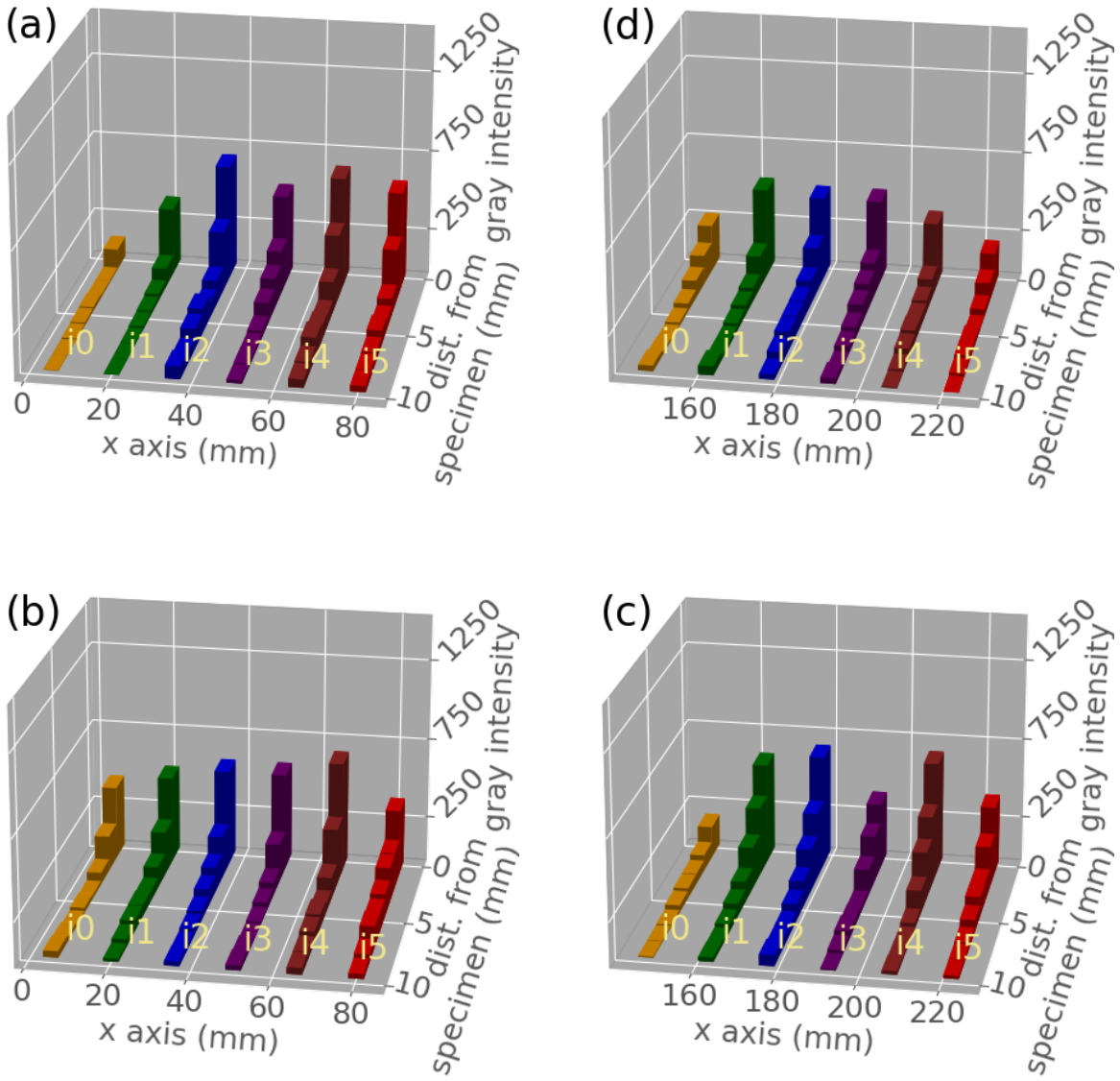

Figure 4.18: Inter-specimen grayscale intensity for Zones 1 to 4, shown in (a) to (d), respectively, in the front ROIs and in LPBF with a scan angle = 0°. This data is for builds produced with **PA powder**.

4.3 Comparison to Metal Porosity

Figure 4.19 shows the coefficient of variation (CoV) in pore diameter plotted in terms of the average grayscale intensity, standard deviation in grayscale intensity, and maximum grayscale intensity. These three assessments are presented in Figure 4.19 (a) to (c), respectively. Each point represents a single specimen, for which statistical metrics of porosity within the specimen as well as statistical metrics of spatter in the region near the specimen have been computed. Interestingly, the three plots show similar clustering arrangements of the points, but there doesn't appear to be a clear trend between the CoV for pore diameter and grayscale intensity of spatter.

Consistent with the spatter intensity metrics used in Figure 4.19, Figures 4.20 and 4.21 present the CoV in pore sphericity and the number of pores, respectively. There is no clear correlation evident with spatter intensity for either the CoV for pore sphericity, or the number of pores.

The average pore diameter and average pore sphericity were also evaluated with respect to the spatter grayscale intensity metrics, but the results were similarly inconclusive. These distributions are presented in Appendix C, Figures C.10 and C.11.

The spatial distribution of porosity was briefly examined to see if any trends were present. While only a portion of the specimens built in the Round Robin program were examined with μCT scanning, (1-2 vertical specimens per ROI) the spatial distribution of pore locations was examined for these specimens, included in Appendix C, Figures C.12 to C.14. The numbering convention used to identify the vertical specimens is shown in Figure 4.22. Figure 4.23 shows a map of pore locations for one of these specimens. There appears to be no distinguishable trend in porosity with respect to location.

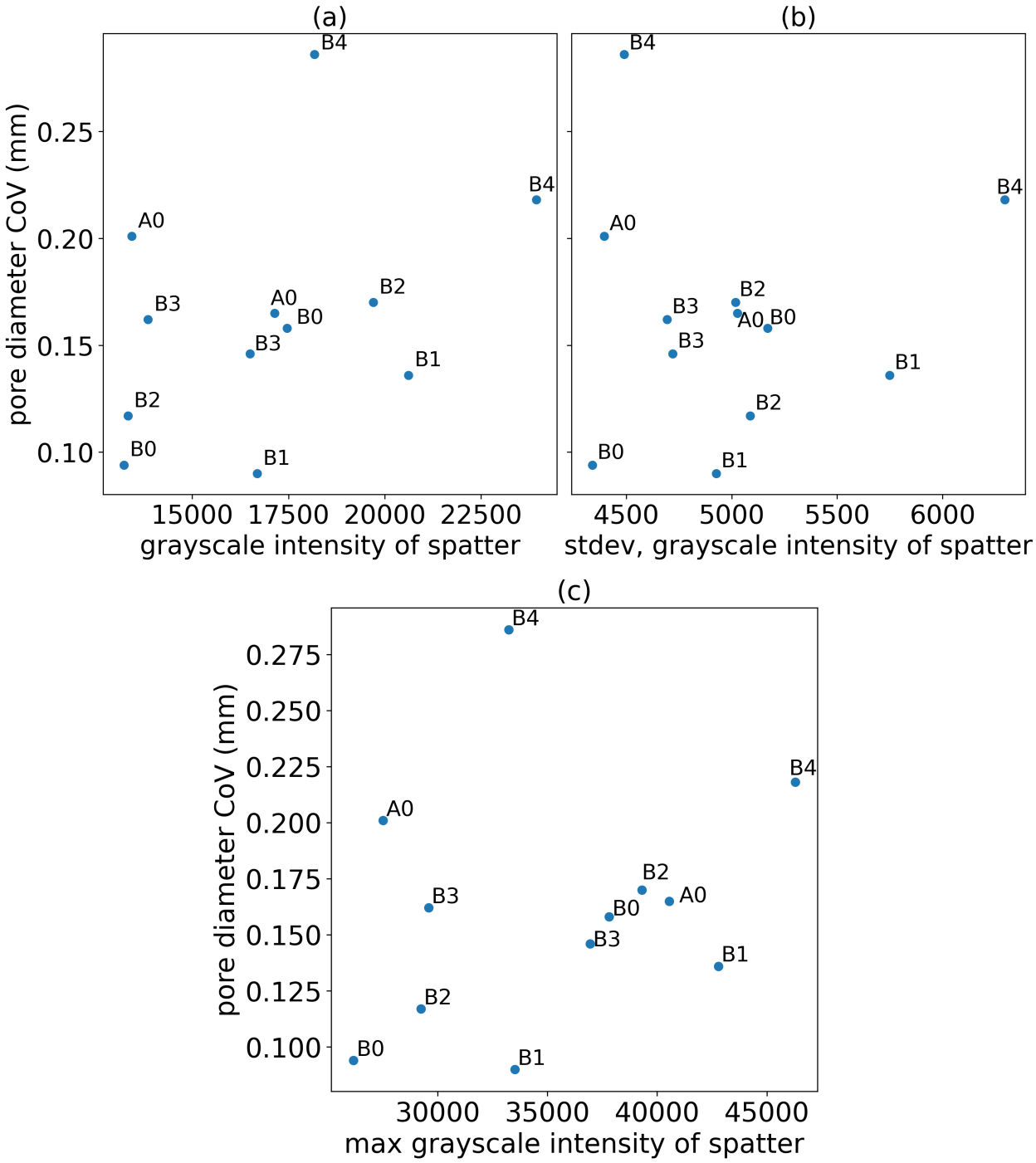

Figure 4.19: Evaluation of the CoV in pore diameter in terms of the (a) grayscale intensity, (b) standard deviation in grayscale intensity, and (c) maximum grayscale intensity.

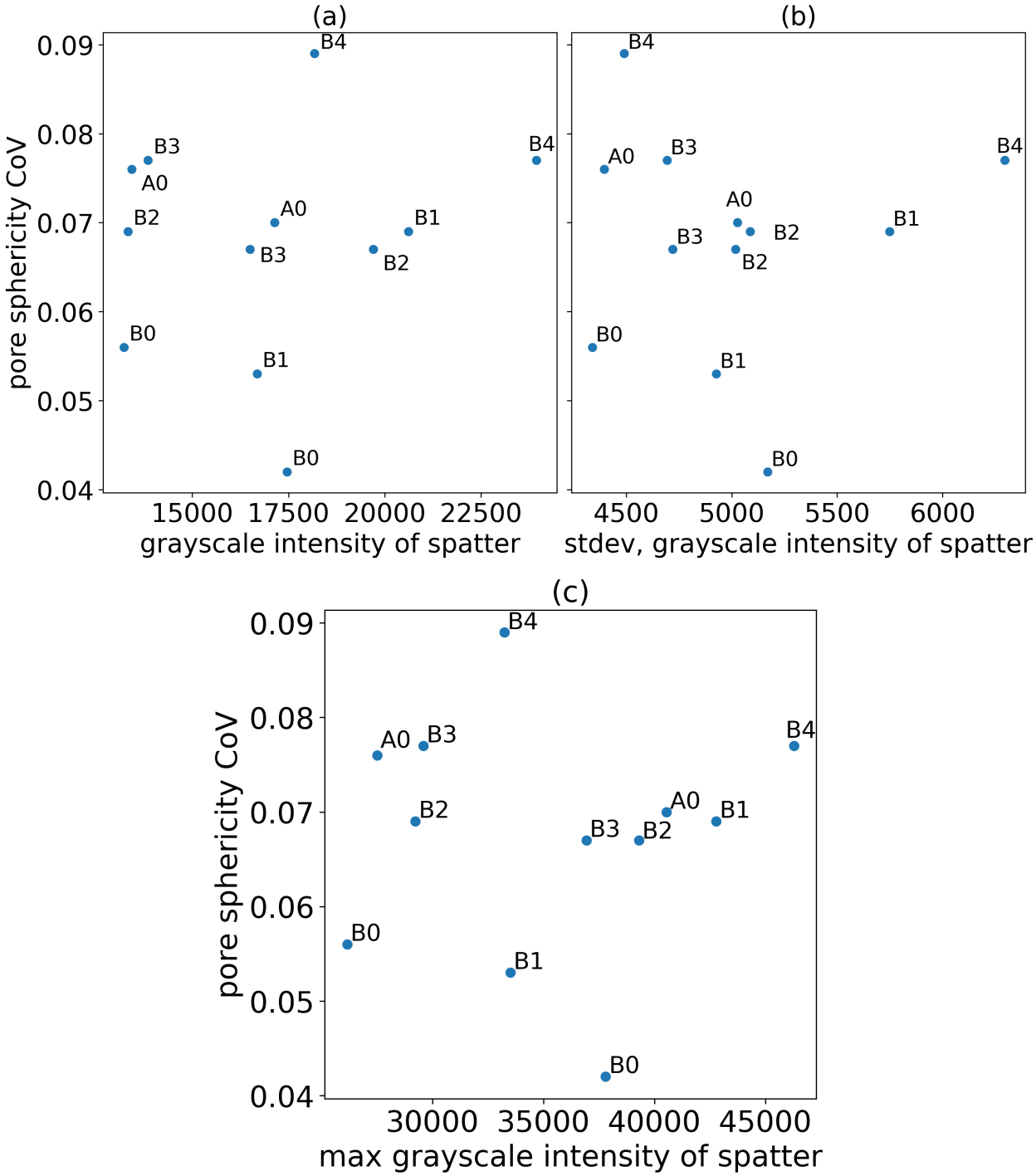

Figure 4.20: Evaluation of the CoV in pore sphericity in terms of the (a) grayscale intensity, (b) standard deviation in grayscale intensity, and (c) maximum grayscale intensity.

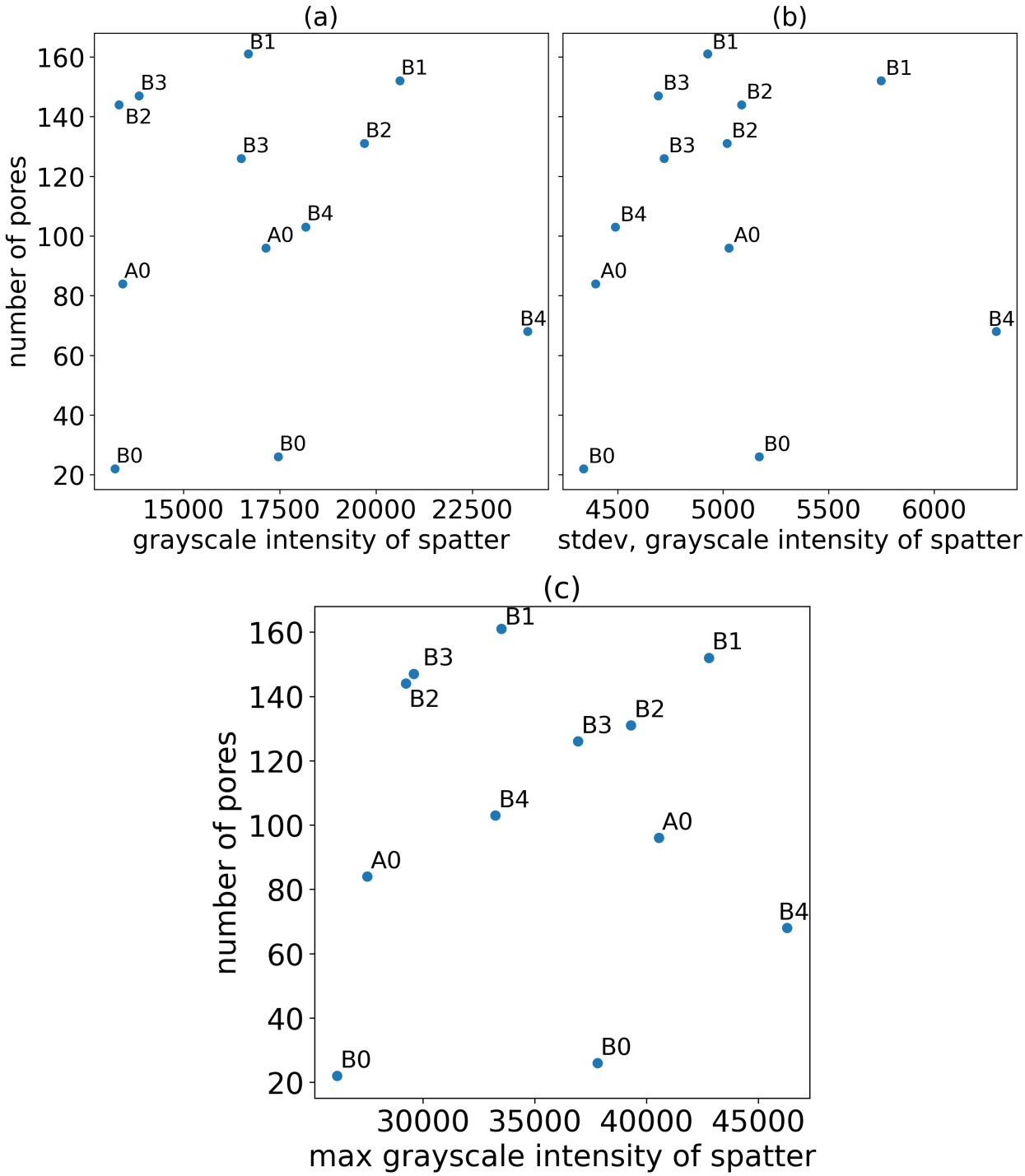

Figure 4.21: Evaluation of the pore count in terms of the (a) grayscale intensity, (b) standard deviation in grayscale intensity, and (c) maximum grayscale intensity.

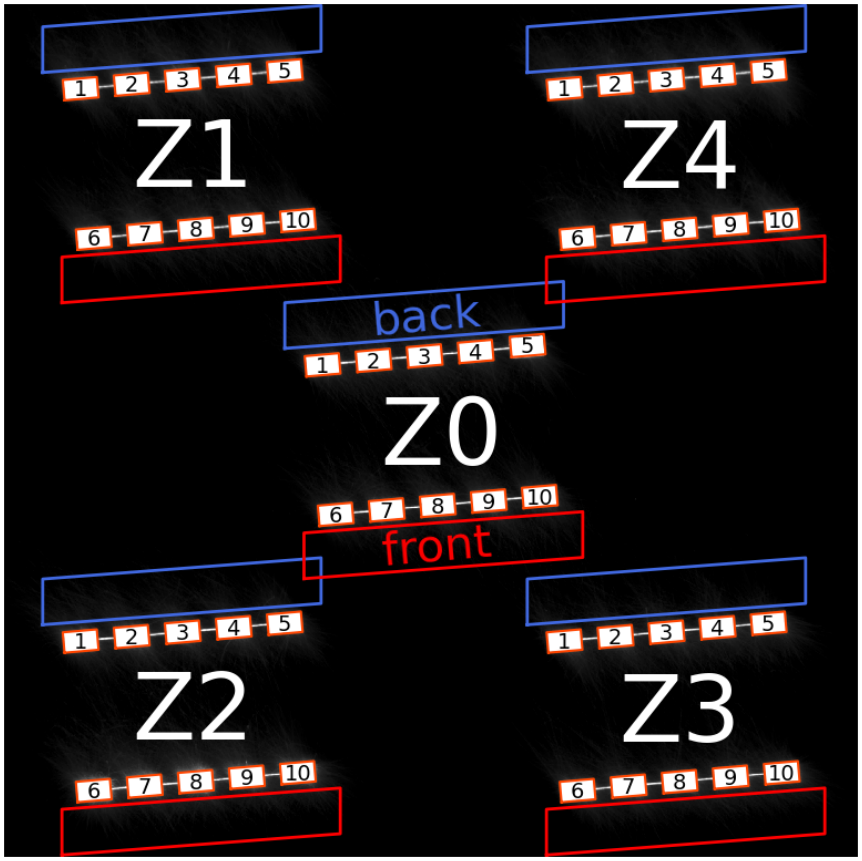

Figure 4.22: Identification of numbering convention for vertical specimens.

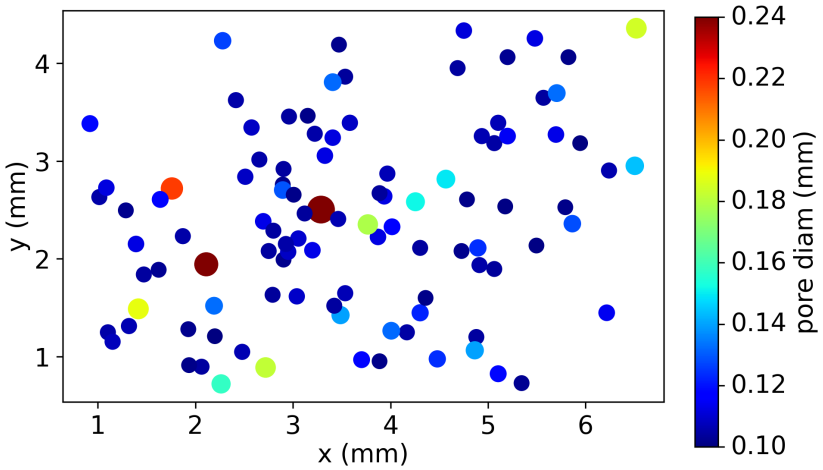

Figure 4.23: Pore locations in specimen s2 for Zone 4, B level, front ROI in UW Round Robin Build 6, performed with **PA powder**. This shows pores as observed along the axis of the vertical specimen. Pores with a circular equivalent diameter less than 100 μm have been omitted.

Chapter 5. DISCUSSION

5.1 Spatter trajectories

One of the primary objectives of this research was to identify relationships between the inert gas flow distribution and both the development of spatter and its trajectory in the build chamber. It was found that two process attributes have a significant influence on the motion of spatter in the build chamber, namely scan angle and gas flow. Overall, the results of this study identify a relationship between laser scan orientation and the ejection angle of spatter particles, and these results provide a means for estimating the direction of gas flow in the build chamber.

Based on the results shown in the spatter angle difference plots, the orientation of spatter trajectories is largely parallel to the scan orientation. In fact, a linear relationship between peak spatter angle and scan orientation was found for the majority of range in scan angle, which was somewhat unexpected. The inert gas flow causes deflection of the spatter trajectories, which is evident from the curvature. In addition, gravity has an influence on the motion of spatter, although to a lesser degree since gravity acts perpendicular to the build plane and the OT images provide planar views that capture grayscale intensity within the build plane.

Due to the physics of the melt pool, as illustrated in Figure 1.3, spatter is ejected primarily anti-parallel to the direction of laser scanning. Being that a bi-directional scan strategy was used for the experiments in this research, spatter will also be ejected bi-directionally. Thus, differences of 180° in angles are disregarded as they identify the same orientation, but opposite direction. In turn, within some degree of variation, the initial velocity of the spatter particle is defined by the scan angle. Once ejected from the meltpool, the particle is subject to drag forces imposed by the gas flow, which act to deflect the direction of travel towards the outlet. That has a large influence on particle motion according to the perspective of the part relative to the gas flow. Particles ejected within the upstream perspective of the metal specimens into the back ROIs will propagate along paths of noticeable curvature, as the y-component of their motion is opposite the direction of gas flow, as represented in Figure 5.1 (a). In this region, the y-component of motion is more or less anti-parallel to the direction of gas flow, and the gas flow serves as a headwind that will reverse the

direction of particle motion during the course of the particle's flight. Conversely, particles ejected within the downstream perspective of the metal specimens into the front ROIs will travel along paths with limited curvature, as represented in Figure 5.1 (b).

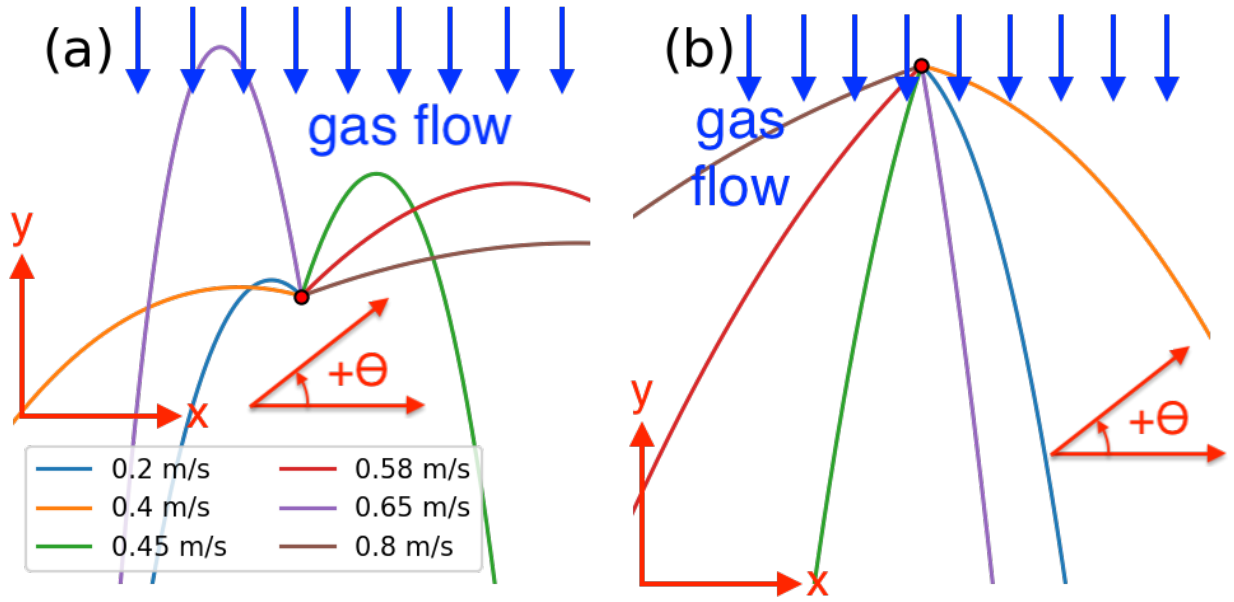

Figure 5.1: Simulated representation of (a) backward ejected particles, and (b) frontward ejected particles. Similarly colored trajectories have the same magnitude of ejection velocity.

In evaluation of the spatter angle difference plots in Figures 4.1 and 4.2, there was a range of scan angles close to 0° where the observed trajectories of the spatter particles are incoherent, and not described by a single primary direction of spatter. Consider the case of bidirectional ejection of particles from the meltpool resulting from scanning with a scan angle of 0° (parallel to the x axis) as detailed in Figure 5.2. If there are no external forces acting on the particles, they will simply travel parallel to the x axis, anti-parallel to the direction of scanning. Now consider the same scenario except with the distributed inert gas flow in the -y direction. The trajectories of the spatter particles will be deflected from the +x and -x directions by the force exerted by the gas. If angles are defined counter-clockwise from the +x axis, the ejection angles of the particles would

be 0° and 180°. Under the force created by the gas flow, the trajectories of the particles would be deflected to within a range of $0° \leq \theta \leq 180°$, respectively, as illustrated in Figure 5.2. A histogram of the spatter orientation should exhibit a bimodal distribution, in which a single normal Gaussian will produce poor results. As such, the degree of uncertainty for the direction of spatter trajectories for scan angles close to 0° is very high.

There are multiple findings of value that can be extracted from the data presented in the spatter angle difference plots. For instance, a higher rate of gas flow will result in a greater deflection of the particles from the angle of ejection, which is primarily parallel to the scan angle. Regions with larger spatter deflection will exhibit a larger difference between spatter angle and scan angle in the spatter angle difference plots and an **increased** amplitude of the erratic region. As such, regions of the build envelope with higher gas flow should also exhibit higher amplitude of the erratic regions of spatter angle difference (near 0°). In the case of a very strong gas flow, all spatter trajectories should be reoriented parallel to the direction of the gas flow, regardless of the angle they were ejected. For lower gas flow rates, a group of spatter ejection angles would be reoriented *closer* to the gas flow direction, thereby reducing the angular variation between spatter trajectories. An example of particles traveling in a gas flow field is illustrated in Figure 5.3 for two different magnitudes of gas flow velocity. Spatter paths should become more coherent with increasing gas flow, and in turn **reduce** the width of the incoherent erratic region. Hence, a higher rate of gas flow is expected to increase the amplitude and decrease the width of the erratic region in the spatter angle difference plots. As such, a positive correlation between the gas flow rate and the slope of the erratic region is expected. Figure 4.4 shows the highest slope of the erratic region for Zone 1, which along with Zone 4 is nearest the gas inlet, a region where higher gas flow velocity is expected. A map of gas flow velocity that was obtained from an experimental analysis of a mock build chamber designed to replicate the gas flow conditions of an EOS M290 printer is shown in Figure 5.4. According to this map, the region of highest gas flow velocity across the build plate occurs in Zone 1.

One concern is that the uncertainty in the estimated gas flow directions presented in Table 4.1 is fairly large. This is not unexpected considering that the spatter trajectories reflected in this

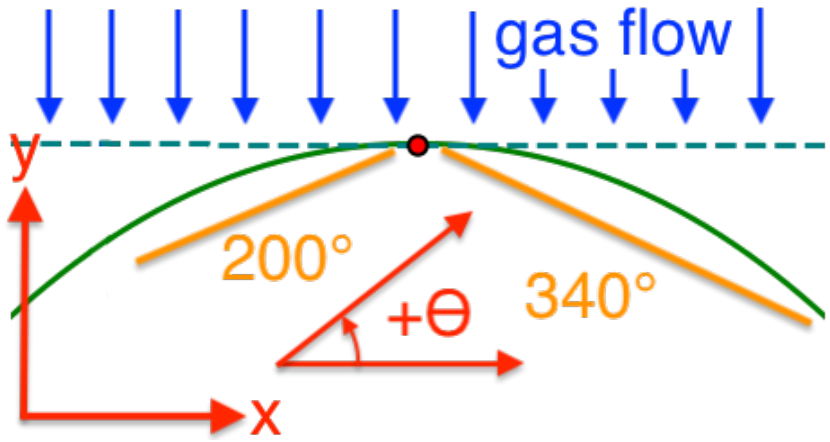

(a) Deflection of spatter for a scan angle = 0°

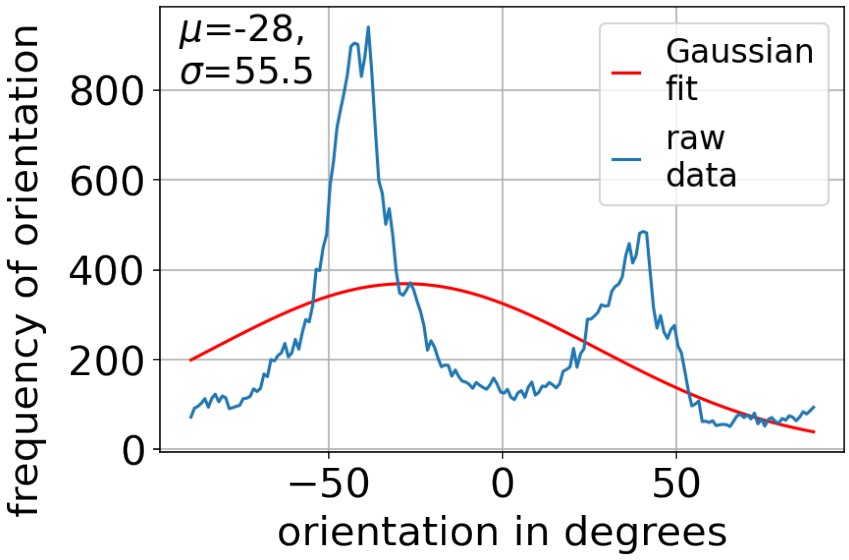

(b) Bi-modal histogram for ROI

Figure 5.2: (a) Illustration of spatter ejection at a scan angle of 0°. The dotted turquoise line represents the path spatter particles would travel in the absence of gas flow, and the solid green line shows the deflected path due to the influence of gas flow. The red dot indicates the origin of the spatter ejections (i.e. the meltpool.) (b) Histogram of spatter trajectory angle for Layer 1071, Z0 front, scan angle = 4°. For this scan angle, the distribution of spatter trajectories exhibits two peak orientations. A single normal Gaussian fit does not give good results for this data.

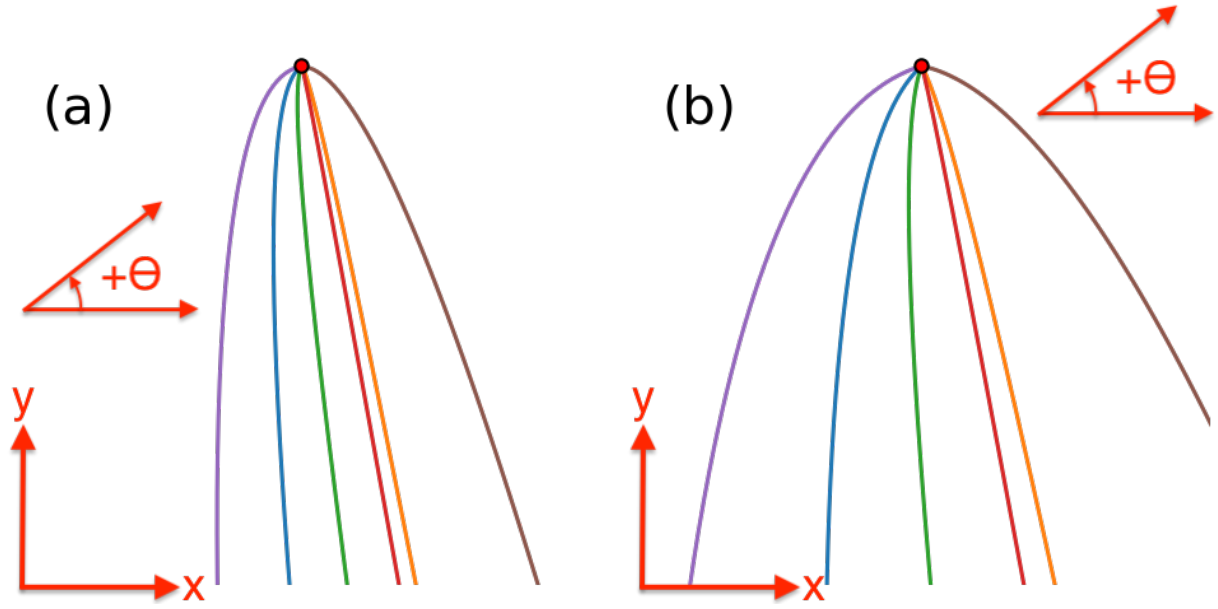

Figure 5.3: Simulated representation of spatter trajectory variation under the influence of (a) a higher rate of gas flow, and (b) a lower rate of gas flow. Similarly colored trajectories have the same magnitude and direction of ejection velocity. Note the tendency in both cases for the effect of gas flow to reduce the angular variation in spatter trajectory.

plot correspond to the entire ROI, which is approximately 70 mm across. In addition, there is a relatively large fluctuation in the gas flow velocity over time within each zone of the build plate that contributes as well. Based on these two contributions, the gas flow could vary significantly throughout each of the ROIs. While Figure 5.4 shows an above average gas flow rate in the Zone 1 front ROI, the gas flow rate in the back ROI of Zone 1, along with the back ROI of Zone 4, is lower than for any of the other ROIs. Since the slope of the erratic region of the spatter-scan angle difference plots is expected to exhibit a direct correlation to the gas flow rate for the corresponding ROI, the slope of the erratic region in the spatter-scan angle difference plot for the Zone 1 back ROI (along with Zone 4 back, which exhibits a similar gas flow rate in Figure 5.4) should be lower than for any of the other ROIs. However, the slope of the erratic region of the spatter-scan angle difference plot for Zone 1 back is higher than that of any of the ROIs of the other 4 zones. While this finding cannot be explained by the distribution of inert gas flow at z = 8 mm alone,

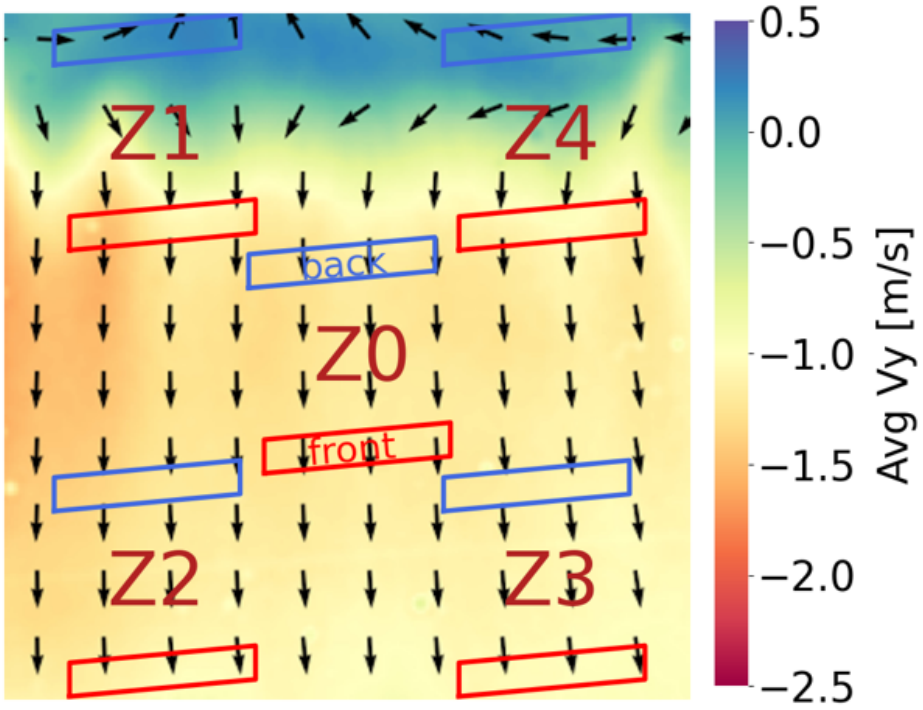

Figure 5.4: Locations of the ROIs superimposed on a map of average gas flow velocity inside the EOS M290 under standard operating conditions. This plot shows gas flow as a function of XY position measured using particle image velocimetry in a plane 8 mm above the build surface [13]. The gas flow data was obtained experimentally using an apparatus designed to replicate the build chamber gas flow profile of an EOS M290 as closely as possible.

there may be variations in the inert gas flow distribution at higher distances from the build plate that result in higher deflection of spatter. An additional possibility is that the spatter particles ejected in the vicinity of Zone 1 are smaller and thus more susceptible to deflection by the inert gas flow. Additional work in this area will support a better understanding of how spatter and other laser-powder interactions are influenced by the inert gas flow.

It is important to note that the view of spatter trajectories (i.e. the camera perspective) is not perpendicular to the build plane but is actually a geometrically transformed projection of spatter trajectories viewed from an angle offset from the build plate normal by approximately 20°. Since the laser lens is located directly above the center of the build plate and cannot be obstructed, the OT camera is mounted off-axis from the center. Due to this angular offset of the OT camera, the

spatter trajectories are distorted from their true shape. Most commercial LPBF systems offer native in-situ data collection tools that can be used to extract relevant process signatures from the data resulting from a build. The aforementioned concern is quite ubiquitous among the commercial systems. However, researchers are aware of this limitation and active research in spatter motion typically uses multiple view angles to resolve the trajectories of spatter in 3D [9, 53]. Future development of the EOS M290 in-situ monitoring suite would benefit from the implementation of two OT cameras on opposing sides of the laser lens. Ideally, this improved hardware configuration would be accompanied by an algorithm capable of resolving the differences in perspective between the two cameras into a single image that shows spatter as if the field of view was parallel to the build plate normal. By resolving the location of spatter features with respect to x and y, comparisons of spatter between different regions of the build can be made with greater accuracy. As a result, the accuracy of the observed spatter trajectory angles would also be improved.

5.2 Area Intensity

The inter-specimen grayscale intensity of spatter content evaluated in this research provides an indirect measure of the amount of spatter generated during the LPBF process. This is based on the assumption that an increase in spatter generation will result in an increase in radiant emissions observed in the OT images. The increase in radiant emissions could be due to either an increase in the number of spatter particles ejected, or due to the spatter particles traveling at a lower velocity and spending more time in the ROIs. In the case of the latter, the time-integrated OT images will exhibit higher grayscale intensities if the slower moving spatter particles are emitting IR radiation within a given area for a longer period of time. Since larger spatter particles tend to travel slower than smaller particles [30], higher grayscale intensity in the OT images is considered to be representative of either higher numbers of spatter particles, or spatter particles that are larger in size. In turn, with greater volumetric spatter content, a greater incidence of defects is expected.

The measures of inter-specimen grayscale intensity quantitatively describe the spatter content present outside the printed regions and were used to evaluate the variation in spatter content as a function of scan angle, location in the build space, and type of powder feedstock. Due to the

concern that spatter particles deflected onto the powder bed can contribute to the generation of metal defects, these measures provide insight into features that can contribute to build quality and reliability.

5.2.1 Variation with Scan Angle

As shown in Figure 4.6, the inter-specimen grayscale intensity depends on the scan angle. This is not surprising since several authors have identified that spatter is primarily ejected anti-parallel to the direction of the laser path [3, 7, 20], which establishes a relationship between scan angle and spatter angle. Interestingly, the inter-specimen grayscale intensity within the front and back ROIs exhibits a different response, which is most significant at 0°. When the laser is scanning (bidirectionally) at an angle of 0°, spatter will also be ejected in this direction within some range, as shown in Figure 5.5. Spatter trajectories that have a small component of motion in the -y direction will continue in this direction and farther from the laser due to the inert gas flow. On the other hand, spatter trajectories that initially have a small component of motion in the +y direction will undergo a reversal in their trajectory due to the force of the inert gas flow.

One interesting observation in comparing the spatter intensity from the back and front perspectives in Figure 4.6 is that the inter-specimen intensity at 0° is higher for the back ROIs relative to the front. ISRs in the back perspective of the build have an offset in the +y direction with respect to the laser incidence and the spatter that enters them was ejected opposite to the direction of the gas flow (upwind). Anwar and Pham [7] observed that when spatter is ejected upwind it can reenter the path of the laser and be re-melted, which results in more spatter. As shown in Figure 5.6, the upwind-directed spatter particle may be re-exposed to the laser after it changes direction and begins moving downwind. If the particle is ejected downwind, it is much less likely to be re-exposed because the stripe velocity, or the rate of advancement of the stripe edge (perpendicular to the scan direction, as shown in Figure 3.1) is typically around 1 to 1.5 m/s [36], whereas spatter particles tend to travel 1 to 5 m/s [9].

Since only the upwind-ejected spatter particles may be re-exposed and produce more spatter, the inter-specimen grayscale intensity at 0° should be higher for the back ROIs than the front ROIs.

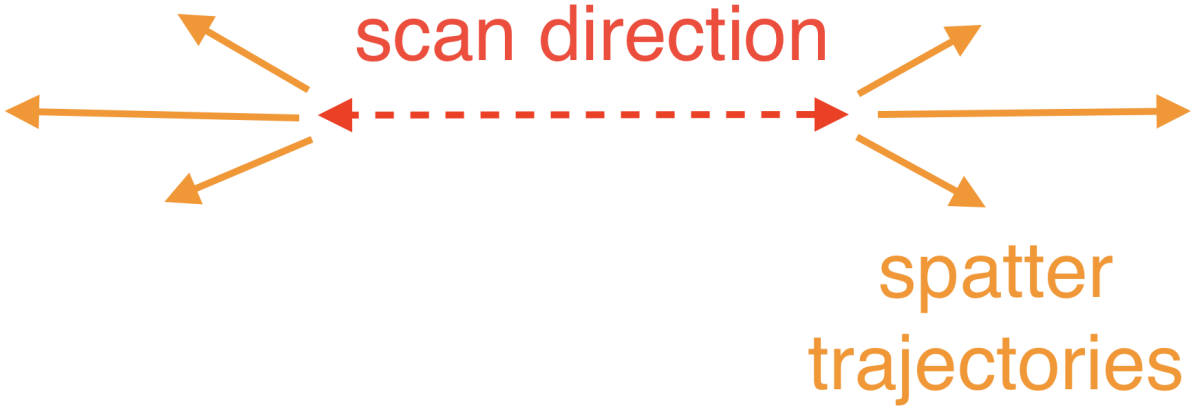

Figure 5.5: Schematic showing trend of spatter ejection direction for a scan angle of 0°.

Indeed, that is reflected in the results presented in Figure 4.6. In fact, the effect is so prominent that it can also be observed in the OT images for scan angles of 0°. As shown in Figure 5.7, the OT image shows greater thermal emissions on the upwind sides of the specimens, from the back perspective of the machine, when compared to the downwind sides. This imbalance in grayscale intensity is consistent across the 0° layers. Two additional layers with a 0° scan angle from Round Robin Build 6 produced with PA powder are shown in Appendix C (Figures C.6 and C.7).

The re-introduction of spatter particles with the laser is also possible when the beam is scanning with 90° angles, which is parallel to the y axis, as shown in Figure 5.8. However, it is less likely due to the direction of the spatter particle velocity and geometry of the emission region.

For a scan angle of $\pm 90°$, only spatter that is emitted in the +y direction has potential for being

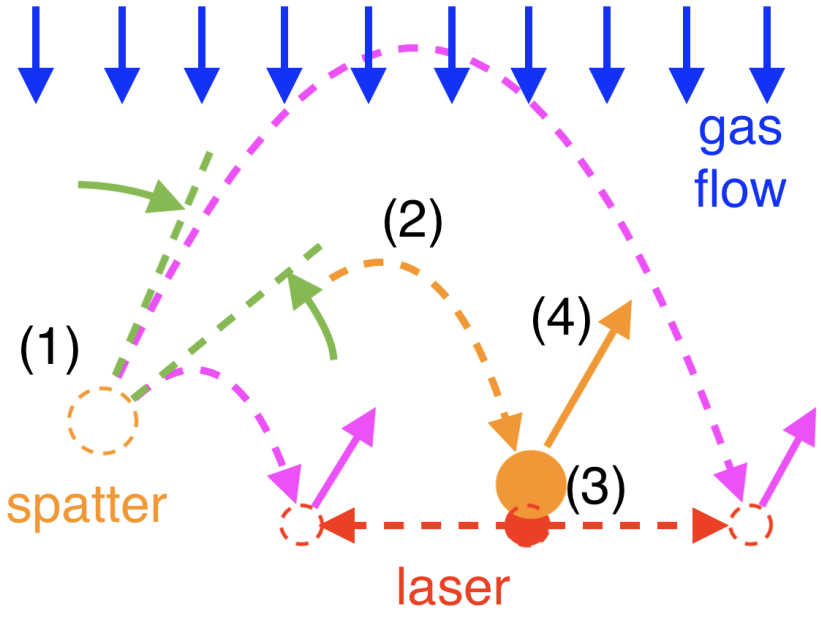

Figure 5.6: Schematic illustrating conditions of multiple incidence of a spatter particle with the laser beam for a scan angle of 0°. (1) Initial emission of spatter particle with partially upwind trajectory. (2) Spatter trajectory is deflected downwind under the influence of the inert gas flow. (3) Downwind side of spatter particle re-encounters the laser beam, resulting in an upwind-directed vapor recoil force. (4) Spatter particle is redirected upwind following re-exposure. Magenta paths identify the limits in trajectory that will result in re-exposure, and green lines indicate the range of ejection angles for the spatter particle that will result in re-exposure.

re-introduced with the laser beam. As described schematically in Figure 5.9, the range of spatter trajectories that will lead to re-incidence with the laser beam is more narrow for a scan angle of 90° than for 0°, and it is more likely that the spatter particle will miss the laser path.

At scan angles of ±90° (same orientation since the difference is 180°) the inter-specimen grayscale intensity of the front ROIs is slightly greater than the intensity of the back ROIs. This suggests that when the laser is scanning parallel to the y axis, the inert gas flow displaces spatter farther from the metal and towards the front of the machine, which results in greater thermal emissions observed on the downwind side of the specimens. The effects of upwind redirection of spatter particles and the re-introduction with the laser beam appear to be less significant at this scan angle in comparison to that at 90°. Therefore, shallow scan angles near 0° are much more likely to

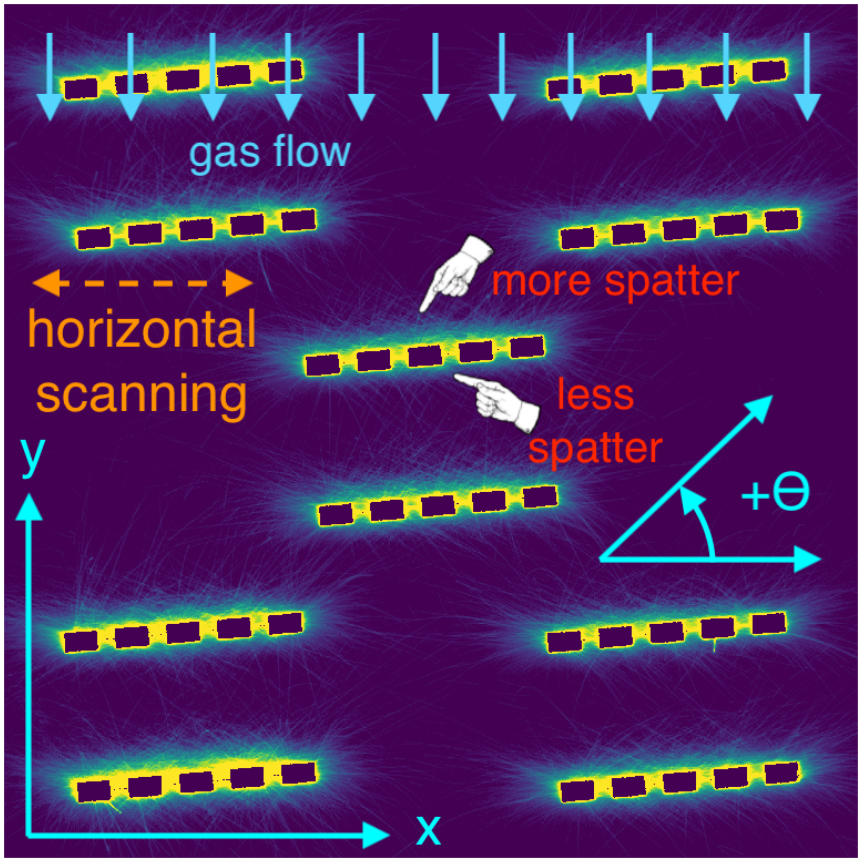

Figure 5.7: OT image of build space at a scan angle of 0° (horizontal). Note that there is more spatter content on the back-facing sides of the specimens than on the front-facing sides. This image is from layer 1079 of Build 1 performed with GA powder.

result in higher spatter entrainment in metal on the back perspective of components.

There is more to consider. If spatter is indeed re-introduced to the laser more often on the upwind side of the specimens than the downwind sides, then it is reasonable to expect a greater incidence of lack-of-fusion defects on the upwind sides of the specimens. Lack-of-fusion defects can result from inadequate volumetric energy density (VED) to achieve complete fusion of the powder. Strategies for mitigating this issue may include the use of scan angles anti-parallel to the direction of gas flow, or are as close to 90° as possible, such that the spatter is ejected downwind and will not be re-exposed to the laser.

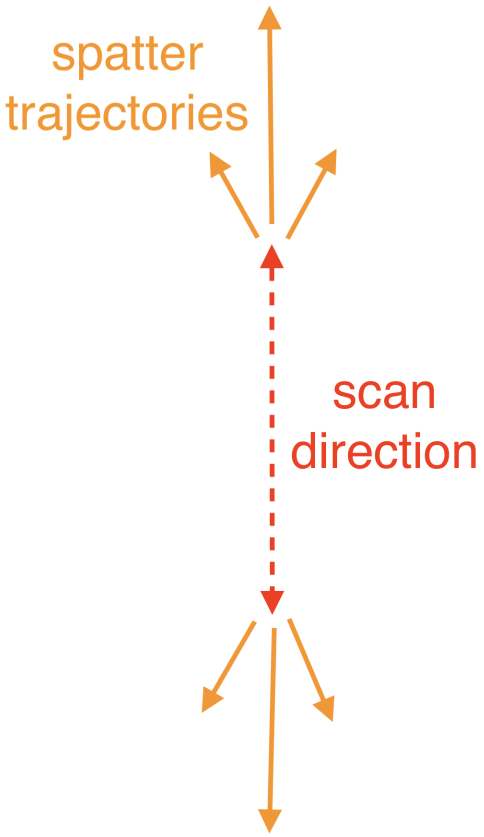

Figure 5.8: Schematic showing trend of spatter ejection direction for a scan angle of 90°.

5.2.2 Variation due to Powder Type

The powder feedstock is one of the primary contributions to cost in the manufacturing of components by LPBF [64]. Powder produced by gas atomization is an economical alternative to powder produced by plasma atomization due to the lower cost of the materials and processing needed. Moreover, the studies by Kassym et al. and Chen et al. [65, 66] showed that the static strength of parts produced with GA powder are not significantly different from that of parts produced with PA powder. That might not be true for the fatigue behavior. However, in the evaluation of inter-specimen grayscale intensity for builds from the UW Round Robin study, the average grayscale intensity was higher for builds performed with GA powder than when performed with PA powder,

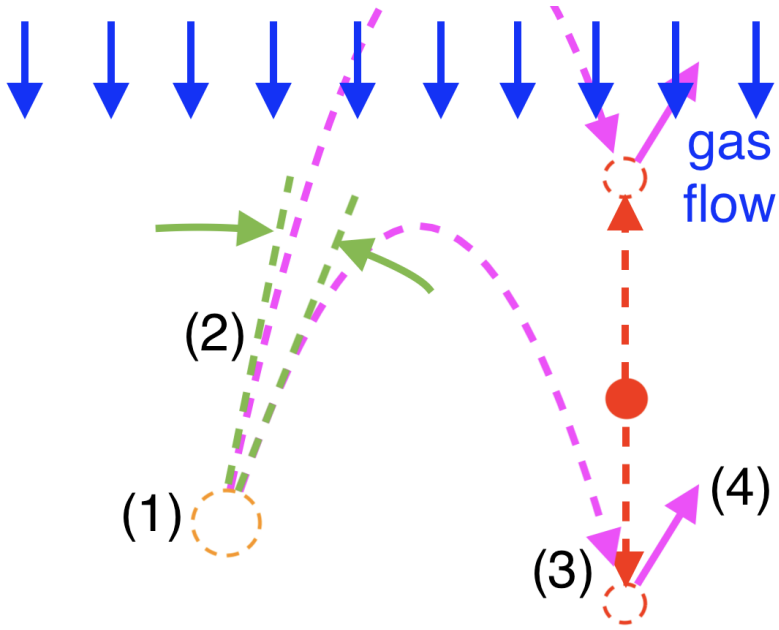

Figure 5.9: Schematic showing trend of spatter ejection direction for a scan angle of 90°. 1) Initial upwind trajectory of spatter particle. (2) Only a very narrow range of trajectory angles (green lines) will result in (3) re-incidence with the laser beam. (4) Spatter particle is redirected upwind following re-exposure. Magenta paths identify the limits in trajectory that will result in re-exposure, and green lines indicate the range of ejection angles for the spatter particle that will result in re-exposure. Compared to Figure 5.6, the range of trajectory angles that will result in re-exposure to the laser when scanning at 90° is narrower than when scanning at 0°. Alternatively, a laser scanning at 90° is a harder target for the spatter particle to hit.

(Figure 4.13). Clearly, more spatter is generated in LPBF of Ti6Al4V when using GA powder than for PA powder. High VED, which leads to spatter formation, often leads to the formation of gas porosity as well [16]. While low levels (<2% by volume) of porosity do not have a significant influence on the static tensile properties of as-printed parts [67], the fatigue strength can be reduced significantly by porosity [68, 69]. Previous studies have shown that spatter contributes to the formation of LOF defects and porosity [3]. Therefore, spatter is also expected to cause a decrease in fatigue strength. Schur [15] reported that both the ductility and porosity of tensile specimens produced with PA powder of Ti6Al4V exhibited similar variation with respect to the location of the build envelope, thereby suggesting a possible relationship between ductility and

porosity. Kasperovich and Hausmann [70] showed that hot isostatic pressing (HIP) treatment can improve the ductility and fatigue strength of Ti6Al4V components produced by LPBF, but at the cost of reduced ultimate strength, as well as additional time and expense. In applications where parts will not experience cyclic loadings, GA powder could be a viable alternative. Nevertheless, results from spatter activity suggest that the fatigue life and ductility will be lower for parts produced with GA powder. Future work may be warranted.

More spatter is emitted in builds performed with GA powder relative to PA powder despite the use of equivalent build design and process parameters. Why is this? A comparison of powder surface texture and morphology resulting from different methods of production is shown in Figure 5.10. GA and PA powders are primarily differentiated by their morphology. In general, GA powder particles are less spherical and have more satellite particles attached, as evident in Figure 5.10 (b). There are a few reasons why the differences in morphology could result in more spatter of GA powder. Irregularly shaped particles have less surface area in contact with each other and may not undergo uniform laser melting. As a result, the particles are more easily displaced by the vapor recoil pressure, and cause emission of spatter. Indeed, the apparent density for the GA powder, listed in Appendix A, is lower than that of the PA powder, suggesting reduced inter-particle contact. Furthermore, a lower apparent density of the powder leads to more gas between the powder particles that can be entrapped in the meltpool and cause gas porosity. In addition, the satellite protrusions noted on the GA powder particles have lower mass and poor thermal contact with the main particles. The smaller size and thermal isolation could result in excessive heating and temperature increase during laser exposure of the satellite particles, which could promote excessive recoil force and cause ejection of nearby powder particles and/or a portion of the meltpool. Finally, GA powder with higher surface roughness would potentially not spread as uniformly as PA powder during recoating, thereby resulting in an uneven layer thickness and further contributing to meltpool instability. Unfortunately, the only flowability metrics available for the powders in the UW Round Robin study were angle of repose for the GA powder and Hall flow rate for the PA powder, which cannot be directly compared.

The particle size distribution metrics reported in Appendix A identify a distribution of smaller

particle sizes for the GA powder as compared to the PA powder. A powder bed of a smaller size distribution has a higher absorptivity than a powder bed composed of larger particles, due to the increased number of laser ray reflections as well as reduced thermal conductivity resulting from a smaller contact area [4]. In this case, the effective incident laser power is higher in the case of GA powder, which could be independently responsible for the increase in spatter generated [4, 39, 20].

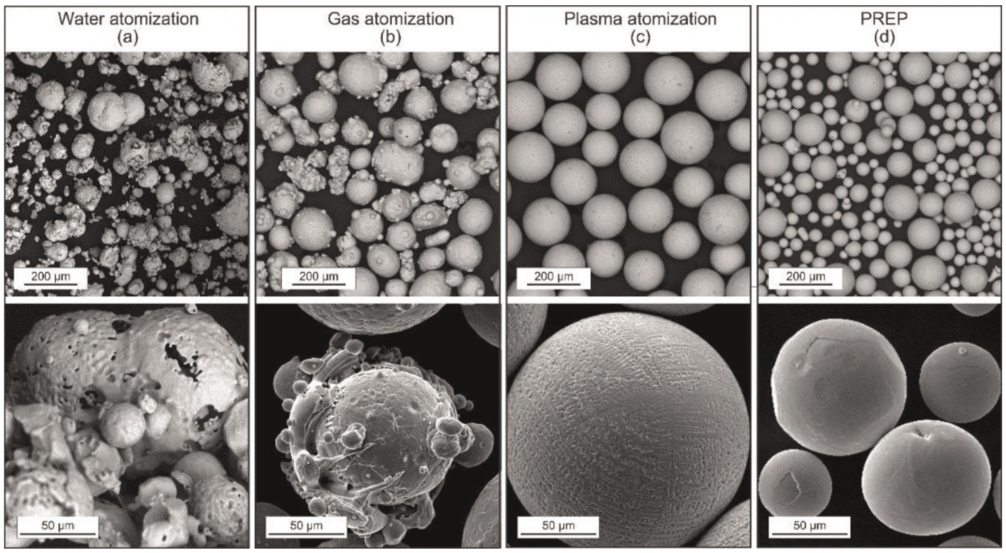

Figure 5.10: Powder surface and morphology for powder produced by various methods. [14]. (a) iron powders produced by water atomization, (b) 316 L powders produced by gas atomization, (c) 316 L powders produced by plasma atomization, and (d) Ti-6Al-4 V powders produced by plasma rotating electrode process (PREP).

While the comparison of results of the spatter distributions for builds performed with the GA and PA powders in this study suggest the likelihood of defects is greater in the builds performed with GA powder, that may not apply universally. Meier et al. [71] reported that certain PA powders had inferior sphericity or a significant oxide layer as compared to the comparable GA powders. In fact, particular GA powders performed better than other PA powders in terms of overall metal part density as well as ductility [71]. The oxide layer and parent metal possess different melting points and absorptivities, which may cause uneven energy intake, melt pool instability, and result

in diminished part properties [71]. An OEM interested in economic powder choices will need to investigate the properties of available certified powders and choose the most affordable option that provides adequate performance that can be qualified for the application.

Process variability is currently the greatest obstacle to widespread adoption of AM. Towards this goal, controlling process variability begins with understanding process variability. A basic understanding of process variability can be developed by utilizing in-situ monitoring tools to monitor spatter. Operating parameters such as laser power [39], scan speed [7], hatch spacing [72] and gas flow [7, 6] are known to have an influence on the mechanical properties of parts. By printing a series of geometrically identical specimens with different combinations of operating parameters for each specimen, i.e. power, speed, hatching parameters, and gas flow rates, the characteristics of the spatter generated using each set of parameters can be evaluated. Such an investigation will yield a set of parameters associated with minimum spatter generation, which can aid in selecting optimum printing parameters, along with consideration of ex-situ mechanical properties or other performance-related characteristics. This method of optimization can be used in reverse as well. In a setting where parts of a fixed geometry are printed in volume with fixed printing parameters, spatter can be monitored through OT imaging and used as a gauge for when evaluation of part performance is necessary. For example, Build 2 of the builds performed with PA powder in this research exhibited above average grayscale intensity of spatter as well as significant random variation in the grayscale intensity levels with respect to scan angle. A sudden variation in spatter characteristics could be an indicator of a process variation that will cause undesirable variation in part performance and needs to be corrected. By monitoring spatter, an OEM can make better informed decisions about process control. With a well-developed understanding of the relationship between spatter and part performance, process variations can be identified sooner and minimized to optimize part performance. This is critical in order for LPBF to maintain an edge as a manufacturing solution.

5.3 Comparison to Metal Porosity

As shown in Figure 5.11, parts produced by laser-directed energy deposition (L-DED) with GA and plasma rotating electrode process (PREP, similar to PA) powder show that parts produced with GA powder may have much higher levels of porosity.

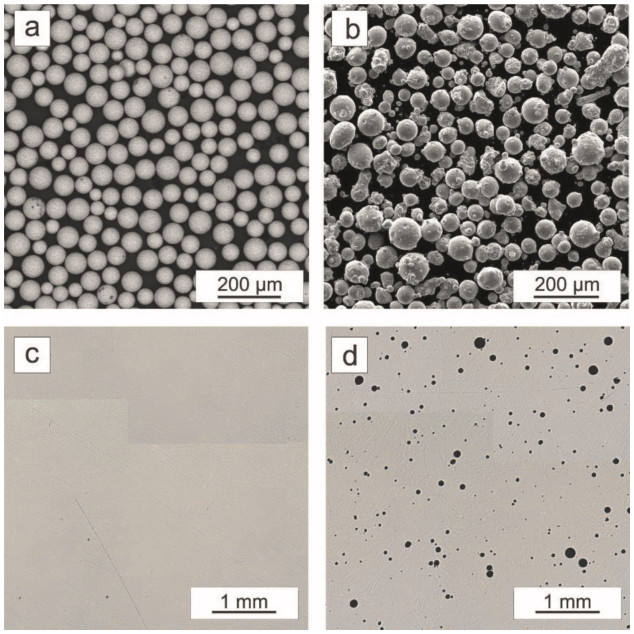

Figure 5.11: Inconel 718 powder produced by PREP and GA [14]. (a) Powder produced by PREP, (b) powder produced by GA, (c) microstructure of parts produced from PREP powder using the L-DED process, and (d) microstructure of parts produced from GA powder using the L-DED process. Note the drastic differences in porosity between (c) and (d).

However, in results from the present study, there was no clear trend between the spatter content gleaned from evaluation of the OT images with the specimen porosity. One limitation of this study in characterizing porosity is that the surface of the specimens was machined prior to μCT scanning. Diehl and Nassar [72] identified that near-surface porosity, located within 400 μm of the surface of LPBF parts can be 4 to 8 times higher than in the bulk. Ghods et al. [73] also found that the porosity in 6 mm diameter cylinders produced by EB-PBF reached a maximum about 500-1000

μm from the surface of the part. This is about the thickness of material that was removed from the surface of the gauge section of the tensile specimens in the RR study, which was necessary to reduce the surface roughness and prevent premature crack initiation in tensile testing. While porosity in the bulk material would still remain after machining, the bulk porosity may not exhibit a large enough range to distinguish the variation between the specimens.

The present approach to analysis provides a representation of the bulk volume of spatter content in the regions adjacent to the specimens. Because spatter events that lead to the formation of porosity may be better defined by spatter that is more energetic, a method to distinguish between spatter that travels short and long distances may be more effective. However, examination of spatter in regions farther from the specimens presents a couple of complications. Moving the ROI farther from the exposed region will capture a greater proportion of spatter from adjacent exposed regions, meaning the data will provide a less localized representation of ejection events. In addition, the size of spatter particles tends to decrease with increasing particle size [30]. As a result, spatter particles that travel farther distances will be more difficult to resolve with the OT camera, not only because of their smaller size but also because they will experience an increased rate of cooling during flight and exhibit radiant emissions captured by the camera for a shorter period of time. Resolving the paths of individual spatter particles from images taken with the OEM OT camera on the EOS M290, while possible, is a difficult task. Tracking the motion of spatter could be facilitated in future studies with higher resolution real-time stereo imaging, as was performed by Barrett et al. in [74].

5.4 Limitations

Despite the advancements made in understanding spatter generated in LPBF of Ti6Al4V with PA and GA powders, there are limitations to the present study that are important to consider. The grayscale intensity of spatter features in the OT images was examined on the assumption that the grayscale intensity has a relationship to the volume of spatter content. While the spatter features observed in the OT images do indicate the presence of spatter, it would be premature to conclude a linear relationship betweeen the inter-specimen grayscale intensity and the actual volume of

spatter produced. For example, the OT camera only detects emission wavelengths between 400 and 900 nm; spatter that has cooled significantly may not be detected. Furthermore, the emissivity of Ti6Al4V depends approximately linearly on temperature [75], and exhibits further variation during thermal oxidation [76]. While OT imaging is indicative of variations in spatter content, the approach in this research cannot be used to directly evaluate and compare the volume of spatter generated in a build.

The OT camera is mounted at an angle off the build plate normal and as such does not provide an accurate representation of the build space as viewed from directly above the build chamber. The camera must be mounted off axis because the laser lens is located directly above the center of the build plate and mounting the camera directly above the center of the build plate would obstruct the laser beam. As such, the OT camera is mounted on the ceiling of the build chamber but is shifted towards the front of the machine with respect to the laser lens. Due to this off-axis camera configuration, only features close to the build surface will be represented accurately. Features located a significant distance above the build surface such as spatter particles in flight will be projected further in the +y direction than they are actually located due to the off axis projection view of the build plate. This results in the observation of more spatter in the back ROIs than would be observed if the OT images were captured viewing the powder bed surface along the build plate normal. An illustration of this effect is shown in Figure 5.12 The perspective effect results in the observation of more spatter in the back ROIs, and less spatter in the front ROIs than is actually present.

One of the goals of the UW-Boeing Round Robin study [15] was to monitor changes in the mechanical properties of printed parts with powder reuse. Build 1 was performed with virgin powder, but the powder used in each subsequent build was reused, i.e., after being filtered through a sieve to remove particles of excessive size. The variability in the condition of the powder feedstock for each build limits the ability to make direct comparisons between builds, as powder reuse is known to have an influence on build results [64]. Ideally, all of these builds would have been performed using powder from the same initial batch and powder would not have been reused between builds. While no trends in spatter content were observed over the six builds, the μCT results show

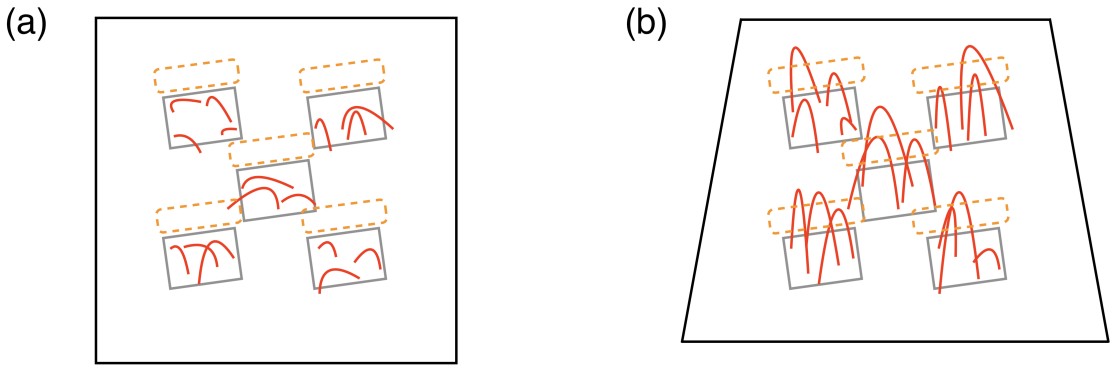

Figure 5.12: Schematic illustration of spatter trajectories as viewed along the (a) build plate normal and (b) from the perspective of the OT camera. The perspective of the OT camera results in vertical motion of spatter particles being projected in the +y direction.

a notable increase in the number of pores between builds 1 and 6.

Spatter is a complex process that is sensitive to a number of process variables, including temporal variations in the inert gas flow distribution [13], the temperature of the printed metal, the amount of oxygen and other gases in the process environment, and more. Future studies could benefit from either controlling or monitoring these process attributes more closely to better understand the degree of influence they have on the LPBF process.

Chapter 6. CONCLUSIONS AND FUTURE WORK

6.1 Conclusions

A series of LPBF builds comprised of identical tensile specimens printed in five different zones of the build chamber were performed on an EOS M290. Builds were performed using both gas atomized (GA) and plasma atomized (PA) powders. During the builds, optical tomography (OT) time-integrated in-situ imaging data was collected for each print layer. The data was analyzed to evaluate variations in spatter with respect to position within the build space, the direction of spatter trajectories, and metal porosity. Analysis of the in-situ data leads to the following conclusions regarding spatter in LPBF:

1. The direction of spatter trajectories emitted from the meltpool is largely parallel to the direction of laser scanning. For the majority of the scan angle range, there is a coherent trend exhibiting a small deviation between the scan angle and the angle of the spatter trajectory, caused by the inert gas flow redirecting spatter towards the exhaust outlet. Near a scan angle of 0°, the relationship between scan and spatter direction is more erratic.

2. Evaluating the difference between the spatter angle and the scan angle as a function of scan angle yields a distribution as shown in Figure 3.14. The x-intercept of the coherent section of this distribution can be used to approximate the direction of gas flow in the ROI, and the slope of the erratic section near 0° is higher in regions of higher inert gas flow. Zone 1 (in the back left corner of the build chamber) exhibits both the highest slope of the erratic region as well as the highest gas flow velocity.

3. In a fixed region adjacent to printed features of components, the grayscale intensity of spatter varies with scan angle. The grayscale intensity is a minimum when the scan orientation is parallel to the x axis for regions upwind as well as downwind of printed specimens. The grayscale intensity in regions upwind of printed specimens exhibits maxima when scanning at approximately $\pm 45°$ with respect to the +x axis, and the grayscale intensity in regions

downwind of the printed specimens exhibits a maximum when scanning parallel to the y axis.

4. The percent difference in average grayscale intensity between the back and front ROIs is greatest where the gas flow velocity is highest. This occurs in Zone 1 and Zone 4, near the back of the build chamber.

5. When the laser scan direction is parallel to the x axis, the grayscale intensity of spatter adjacent to the upwind and downwind sides of printed regions is higher on the upwind side. The origin of this phenomenon was not identified.

6. The builds produced with gas atomized (GA) powder exhibited greater spatter content than those performed with plasma atomized (PA) powder. The cause appears to be due to the effect of powder particle morphology on LPBF processing. While GA powder may be a more economical option, more spatter content indicates an increased likelihood of defects.

6.2 Future Work

Khairallah et al. [5, 20] showed that simulation of the LPBF process with ALE3D (Arbitrary Lagrangian-Eulerian multi-physics numerical simulation software) can reveal complex phenomena of spatter generation that are missed in simplified simulations. Their studies showed that fine details such as distribution of particle sizes in the powder bed and the energy intensity profile of the laser spot have significant influence on simulation results, which highlight the opportunity to learn more through detailed simulation models. Simulation results could be used to guide the design of LPBF builds that are tuned to achieve better understanding of the in-situ data obtained from the build. This is a rich area for future work.

Variation in gas flow is understood to have a significant effect on build quality in the LPBF process [7]. A brief comparison between experimental data for gas flow and spatter identified a correlation, which merits further investigation. Experimentally obtained gas flow data could aid in design of realistic simulations of spatter motion, and support evaluation of trends in spatter with

respect to gas flow and its impact on build design and build quality. Future work in this area could also be fruitful.

It was discovered that the observed grayscale intensity of the images produced by the OT camera varies in intensity with respect to the distance from the camera. This spatial aspect of the grayscale intensity was corrected by applying a polynomial fit to the intensity pattern of the images as described in Appendix B. Using this method of data correction in future analysis of in-situ data will produce more accurate results than by using raw data.

This study was primarily performed to advance understanding of variations in spatter intensity within the build space and to use that knowledge to interpret variations in gas flow across the build space. A study of the effects of spatter will be continued as part of a broader effort using the Peregine software package developed by researchers in the Manufacturing Demonstration Facility (MDF) group at Oak Ridge National Laboratory (ORNL) [28]. The purpose of this future work is to pursue a deeper understanding of the relationships between part defects and the LPBF process anomalies that can be observed through in-situ imaging. Peregrine will be used to label anomalies observed in in-situ imaging data and the annotations will be used to train a dynamically segmented convolutional neural network used to predict process anomalies from additional in-situ data. This approach will support incorporation of part geometry and ex-situ μCT data as well to both validate and improve the accuracy of the results. The findings of this thesis will serve as the foundation for future studies.

BIBLIOGRAPHY

[1] LISI Aerospace Additive Manufacturing, "LISI makes large additive manufacturing parts a reality," https://www.lisi-aerospace-am.com/en/2019/05/22/lisi-makes-large-additive-manufacturing-parts-a-reality/, 2022.

[2] J. Smith, "Sigma Labs' in-process technology to overcome barriers in metal 3D printing," May 2015. [Online]. Available: https://3dprint.com/67882/sigma-labs-eta-3d-print/

[3] J. Yin, D. Wang, L. Yang, H. Wei, P. Dong, L. Ke, G. Wang, H. Zhu, and X. Zeng, "Correlation between forming quality and spatter dynamics in laser powder bed fusion," *Additive Manufacturing*, vol. 31, p. 100958, Jan. 2020. [Online]. Available: https://linkinghub.elsevier.com/retrieve/pii/S2214860419317415

[4] J. Liu and P. Wen, "Metal vaporization and its influence during laser powder bed fusion process," *Materials & Design*, vol. 215, p. 110505, Mar. 2022. [Online]. Available: https://linkinghub.elsevier.com/retrieve/pii/S0264127522001265

[5] S. A. Khairallah, A. T. Anderson, A. Rubenchik, and W. E. King, "Laser powder-bed fusion additive manufacturing: Physics of complex melt flow and formation mechanisms of pores, spatter, and denudation zones," *Acta Materialia*, vol. 108, pp. 36–45, 2016. [Online]. Available: https://www.sciencedirect.com/science/article/pii/S135964541630088X

[6] X.-X. Chen and W.-C. Wang, "The applications of particle image velocimetry (PIV) to experimentally observe the flow behaviors inside the Selective Laser Melting (SLM) working chamber," *Flow Measurement and Instrumentation*, vol. 73, p. 101738, Jun. 2020. [Online]. Available: https://linkinghub.elsevier.com/retrieve/pii/S0955598620300868

[7] A. B. Anwar and Q.-C. Pham, "Selective laser melting of AlSi10Mg: Effects of scan direction, part placement and inert gas flow velocity on tensile strength," *Journal of Materials Processing Technology*, vol. 240, pp. 388–396, 2017. [Online]. Available: https://api.semanticscholar.org/CorpusID:138013033

[8] EOS GmbH, *Basic training EOS M 290*, 2017.

[9] R. D. Fischer, M. Moaven, D. Kelly, S. Morris, B. Thurow, and B. C. Prorok, "3D tracking velocimetry of L-PBF spatter particles using a single high-speed plenoptic camera," *Additive Manufacturing Letters*, vol. 3, p. 100083, Dec. 2022. [Online]. Available: https://linkinghub.elsevier.com/retrieve/pii/S2772369022000524

[10] H. T. Tran and A. C. To, "Cracking prediction at solid-tooth support interface during laser powder bed fusion additive manufacturing," *Journal of Science: Advanced Materials and Devices*, vol. 8, no. 4, p. 100615, 2023. [Online]. Available: https://www.sciencedirect.com/science/article/pii/S2468217923000849

[11] Z. lv, J. G. Santos Macías, A. Dolimont, A. Simar, and E. Riviere, "Comparison of residual stresses obtained by the crack compliance method for parts produced by different metal additive manufacturing techniques and after friction stir processing," *Additive Manufacturing*, vol. 36, 07 2020.

[12] A. Montelione, "M290 gas nozzles," 2024, image of the build chamber of a EOS M290 printer.

[13] A. Abeyta, "An Experimental Approach for Characterizing Gas Flow in the Build Chamber of Laser Powder Bed Fusion Systems Utilizing Particle Image Velocimetry," Master's thesis, University of Washington, 2024.

[14] M. Gushchina, O. Klimova-Korsmik, and G. Turichin, "Features of the powder application in direct laser deposition technology," Feb 2023. [Online]. Available: http://dx.doi.org/10.5772/intechopen.108853

[15] R. Schur, "Laser Powder Bed Fusion of Ti-6Al-4V: A round robin analysis of mechanical property variability," Ph.D. dissertation, University of Washington, 2023.

[16] T. DebRoy, H. Wei, J. Zuback, T. Mukherjee, J. Elmer, J. Milewski, A. Beese, A. Wilson-Heid, A. De, and W. Zhang, "Additive manufacturing of metallic components – process, structure and properties," *Progress in Materials Science*, vol. 92, pp. 112–224, 2018. [Online]. Available: https://www.sciencedirect.com/science/article/pii/S0079642517301172

[17] M. Eryıldız, "Effect of build orientation on mechanical behaviour and build time of FDM 3D-printed PLA parts: An experimental investigation," *European Mechanical Science*, vol. 5, no. 3, p. 116–120, 2021.

[18] W. E. Frazier, "Metal additive manufacturing: A review," *Journal of Materials Engineering and Performance*, vol. 23, no. 6, pp. 1917–1928, Jun 2014. [Online]. Available: https://doi.org/10.1007/s11665-014-0958-z

[19] M. Hannibal and G. Knight, "Additive manufacturing and the global factory: Disruptive technologies and the location of international business," *International Business Review*, vol. 27, no. 6, pp. 1116–1127, 2018. [Online]. Available: https://www.sciencedirect.com/science/article/pii/S0969593117306856

[20] S. Khairallah, A. Martin, J. Lee, G. Guss, N. Calta, J. Hammons, M. Nielsen, K. Chaput, E. Schwalbach, M. Shah, M. Chapman, T. Willey, A. Rubenchik, A. Anderson, Y. Wang, M. Matthews, and W. King, "Controlling interdependent meso-nanosecond dynamics and defect generation in metal 3D printing," *Science*, vol. 368, pp. 660–665, 05 2020.

[21] P. Deng, M. Karadge, R. B. Rebak, V. K. Gupta, B. C. Prorok, and X. Lou, "The origin and formation of oxygen inclusions in austenitic stainless steels manufactured by laser powder bed fusion," *Additive Manufacturing*, vol. 35, p. 101334, 2020. [Online]. Available: https://www.sciencedirect.com/science/article/pii/S2214860420307065

[22] H. Chen and W. Yan, "Spattering and denudation in laser powder bed fusion process: Multiphase flow modelling," *Acta Materialia*, vol. 196, pp. 154–167, 2020. [Online]. Available: https://www.sciencedirect.com/science/article/pii/S1359645420304687

[23] A. Gasper, B. Szost, X. Wang, D. Johns, S. Sharma, A. Clare, and I. Ashcroft, "Spatter and oxide formation in laser powder bed fusion of Inconel 718," *Additive Manufacturing*, vol. 24, pp. 446–456, 2018. [Online]. Available: https://www.sciencedirect.com/science/article/pii/S2214860418304524

[24] J. A. Slotwinski, E. J. Garboczi, P. E. Stutzman, C. F. Ferraris, S. S. Watson, and M. A. Peltz, "Characterization of metal powders used for additive manufacturing," *Journal of Research of the National Institute of Standards and Technology*, vol. 119, p. 460–493, Sep 2014.

[25] M. Taheri Andani, R. Dehghani, M. R. Karamooz-Ravari, R. Mirzaeifar, and J. Ni, "Spatter formation in selective laser melting process using multi-laser technology," *Materials & Design*, vol. 131, pp. 460–469, 2017. [Online]. Available: https://www.sciencedirect.com/science/article/pii/S0264127517306238

[26] V. Gunenthiram, P. Peyre, M. Schneider, M. Dal, F. Coste, I. Koutiri, and R. Fabbro, "Experimental analysis of spatter generation and melt-pool behavior during the powder bed laser beam melting process," *Journal of Materials Processing Technology*, vol. 251, pp. 376–386, 2018. [Online]. Available: https://www.sciencedirect.com/science/article/pii/S0924013617303606

[27] R. Cunningham, C. Zhao, N. Parab, C. Kantzos, J. Pauza, K. Fezzaa, T. Sun, and A. D. Rollett, "Keyhole threshold and morphology in laser melting revealed by ultrahigh-speed x-ray imaging," *Science*, vol. 363, no. 6429, pp. 849–852, 2019. [Online]. Available: https://www.science.org/doi/abs/10.1126/science.aav4687

[28] Z. Snow, L. Scime, A. Ziabari, B. Fisher, and V. Paquit, "Scalable in situ non-destructive evaluation of additively manufactured components using process monitoring, sensor fusion,

and machine learning," *Additive Manufacturing*, vol. 78, p. 103817, Sep. 2023. [Online]. Available: https://linkinghub.elsevier.com/retrieve/pii/S221486042300430X

[29] Y. Liu, Y. Yang, S. Mai, D. Wang, and C. Song, "Investigation into spatter behavior during selective laser melting of AISI 316L stainless steel powder," *Materials & Design*, vol. 87, pp. 797–806, 2015. [Online]. Available: https://www.sciencedirect.com/science/article/pii/S0264127515303361

[30] M. Yoshida, T. Furumoto, K. Sakuma, K. Kawasaki, and K. Itagaki, "Experimental investigation of spatter particle behavior and improvement in build quality in PBF-LB," *International Journal of Automation Technology*, vol. 17, no. 4, pp. 335–345, 2023. [Online]. Available: https://www.fujipress.jp/ijat/au/ijate001700040335

[31] Z. A. Young, Q. Guo, N. D. Parab, C. Zhao, M. Qu, L. I. Escano, K. Fezzaa, W. Everhart, T. Sun, and L. Chen, "Types of spatter and their features and formation mechanisms in laser powder bed fusion additive manufacturing process," *Additive Manufacturing*, vol. 36, p. 101438, 2020. [Online]. Available: https://www.sciencedirect.com/science/article/pii/S2214860420308101

[32] R. G. Tryon, R. McDaniels, A. Chern, M. Oja, A. Dey, I. Awad, and C. Duty, *Probabilistic Computational Fatigue and Fracture Modeling of Additive Manufactured Components*. ASTM International, 2020.

[33] R. McCann, M. A. Obeidi, C. Hughes, É. McCarthy, D. S. Egan, R. K. Vijayaraghavan, A. M. Joshi, V. Acinas Garzon, D. P. Dowling, P. J. McNally, and D. Brabazon, "In-situ sensing, process monitoring and machine control in Laser Powder Bed Fusion: A review," *Additive Manufacturing*, vol. 45, p. 102058, Sep. 2021. [Online]. Available: https://linkinghub.elsevier.com/retrieve/pii/S2214860421002232

[34] S. M. Estalaki, C. S. Lough, R. G. Landers, E. C. Kinzel, and T. Luo, "Predicting defects in laser powder bed fusion using in-situ thermal imaging data and machine learning," *Additive Manufacturing*, vol. 58, p. 103008, Oct. 2022. [Online]. Available: https://linkinghub.elsevier.com/retrieve/pii/S2214860422004018

[35] G. Mohr, S. J. Altenburg, A. Ulbricht, P. Heinrich, D. Baum, C. Maierhofer, and K. Hilgenberg, "In-situ defect detection in laser powder bed fusion by using thermography and optical tomography—comparison to computed tomography," *Metals*, vol. 10, no. 1, p. 103, 2020.

[36] C. Pauzon, B. Hoppe, T. Pichler, S. Dubiez-Le Goff, P. Forêt, T. Nguyen, and E. Hryha, "Reduction of incandescent spatter with helium addition to the process gas during laser powder bed fusion of Ti-6Al-4V," *CIRP Journal of Manufacturing*

Science and Technology, vol. 35, pp. 371–378, 2021. [Online]. Available: https://www.sciencedirect.com/science/article/pii/S1755581721001206

[37] J. Greses, P. A. Hilton, C. Y. Barlow, and W. M. Steen, "Plume attenuation under high power Nd:yttritium–aluminum–garnet laser welding," *J. Laser Appl.*, vol. 16, no. 1, pp. 9–15, Feb. 2004.

[38] A. T. Sutton, C. S. Kriewall, M. C. Leu, J. W. Newkirk, and B. Brown, "Characterization of laser spatter and condensate generated during the selective laser melting of 304L stainless steel powder," *Additive Manufacturing*, vol. 31, p. 100904, 2020. [Online]. Available: https://www.sciencedirect.com/science/article/pii/S2214860419302787

[39] D. Wang, S. Wu, F. Fu, S. Mai, Y. Yang, Y. Liu, and C. Song, "Mechanisms and characteristics of spatter generation in slm processing and its effect on the properties," *Materials & Design*, vol. 117, pp. 121–130, 2017. [Online]. Available: https://www.sciencedirect.com/science/article/pii/S0264127516315866

[40] Z. Wu, Z. Xu, and W. Fan, "Online detection of powder spatters in the additive manufacturing process," *Measurement*, vol. 194, p. 111040, 2022. [Online]. Available: https://www.sciencedirect.com/science/article/pii/S0263224122003062

[41] K. Mumtaz and N. Hopkinson, "Selective laser melting of thin wall parts using pulse shaping," *Journal of Materials Processing Technology*, vol. 210, no. 2, pp. 279–287, 2010. [Online]. Available: https://www.sciencedirect.com/science/article/pii/S0924013609003422

[42] D. Gu, D. Dai, W. Chen, and H. Chen, "Selective laser melting additive manufacturing of hard-to-process tungsten-based nanocomposites with novel crystalline growth morphology and enhanced performance," *Journal of Manufacturing Science and Engineering*, vol. 138, 12 2015.

[43] S. Feng, Z. Chen, B. Bircher, Z. Ji, L. Nyborg, and S. Bigot, "Predicting laser powder bed fusion defects through in-process monitoring data and machine learning," *Materials & Design*, vol. 222, p. 111115, 2022. [Online]. Available: https://www.sciencedirect.com/science/article/pii/S0264127522007377

[44] J.-P. Kruth, P. Mercelis, J. Van Vaerenbergh, and T. Craeghs, *Feedback control of Selective Laser Melting*. KU Leuven, Sep 2007, pp. 521–527. [Online]. Available: https://lirias.kuleuven.be/retrieve/110134

[45] J. Yin, W. Zhang, L. Ke, H. Wei, D. Wang, L. Yang, H. Zhu, P. Dong, G. Wang, and X. Zeng, "Vaporization of alloying elements and explosion behavior during laser powder bed fusion of Cu–10Zn alloy," *International Journal of Machine*

Tools and Manufacture, vol. 161, p. 103686, 2021. [Online]. Available: https://www.sciencedirect.com/science/article/pii/S089069552030701X

[46] C. Zhao, Q. Guo, X. Li, N. Parab, K. Fezzaa, W. Tan, L. Chen, and T. Sun, "Bulk-explosion-induced metal spattering during laser processing," *Phys. Rev. X*, vol. 9, p. 021052, Jun 2019. [Online]. Available: https://link.aps.org/doi/10.1103/PhysRevX.9.021052

[47] W.-C. Wang and C.-Y. Chang, "Flow analysis of the laminated manufacturing system with laser sintering of metal powder. part i: flow uniformity inside the working chamber," *The International Journal of Advanced Manufacturing Technology*, vol. 92, 09 2017.

[48] J. Albert, O. Hermann, S. Purschke, D. Rule, and C. Fleck, "Investigation on process stability and part positioning influence on the relative density of designed materials via laser-based powder bed fusion of metals on a multi-laser machine," *Advanced Engineering Materials*, vol. 24, no. 1, p. 2100635, 2022. [Online]. Available: https://onlinelibrary.wiley.com/doi/abs/10.1002/adem.202100635

[49] A. Montelione, S. Ghods, R. Schur, C. Wisdom, D. Arola, and M. Ramulu, "Powder reuse in Electron Beam Melting Additive Manufacturing of Ti6Al4V: Particle microstructure, oxygen content and mechanical properties," *Additive Manufacturing*, vol. 35, p. 101216, 2020. [Online]. Available: https://www.sciencedirect.com/science/article/pii/S2214860420305881

[50] P. Yuan and D. Gu, "Molten pool behaviour and its physical mechanism during selective laser melting of TiC/AlSi10Mg nanocomposites: simulation and experiments," *Journal of Physics D: Applied Physics*, vol. 48, no. 3, p. 035303, jan 2015. [Online]. Available: https://dx.doi.org/10.1088/0022-3727/48/3/035303

[51] V. Semak and A. Matsunawa, "The role of recoil pressure in energy balance during laser materials processing," *Journal of Physics D: Applied Physics*, vol. 30, no. 18, p. 2541, sep 1997. [Online]. Available: https://dx.doi.org/10.1088/0022-3727/30/18/008

[52] A. Kaplan, "A model of deep penetration laser welding based on calculation of the keyhole profile," *Journal of Physics D: Applied Physics*, vol. 27, no. 9, p. 1805, sep 1994. [Online]. Available: https://dx.doi.org/10.1088/0022-3727/27/9/002

[53] D. Kelly, R. D. Fischer, M. Moaven, S. Morris, B. C. Prorok, and B. Thurow, "Simultaneous 3D tracking and temperature measurements of L-PBF spatter particles using a single camera," *Additive Manufacturing Letters*, vol. 6, p. 100134, Jul. 2023. [Online]. Available: https://linkinghub.elsevier.com/retrieve/pii/S2772369023000154

[54] A. du Plessis, M. Tshibalanganda, and S. le Roux, "Not all scans are equal: X-ray tomography image quality evaluation," *Materials Today Communications*, vol. 22, p. 100792, 2020. [Online]. Available: https://www.sciencedirect.com/science/article/pii/S2352492819308694

[55] R. Wang, D. Garcia, R. R. Kamath, C. Dou, X. Ma, B. Shen, H. Choo, K. Fezzaa, H. Z. Yu, and Z. J. Kong, "In situ melt pool measurements for laser powder bed fusion using multi sensing and correlation analysis," *Scientific Reports*, vol. 12, no. 1, p. 13716, Aug 2022. [Online]. Available: https://doi.org/10.1038/s41598-022-18096-w

[56] H. Zhang, C. K. P. Vallabh, and X. Zhao, "Influence of spattering on in-process layer surface roughness during Laser Powder Bed Fusion," *Journal of Manufacturing Processes*, vol. 104, pp. 289–306, 2023. [Online]. Available: https://www.sciencedirect.com/science/article/pii/S1526612523008484

[57] G. Repossini, V. Laguzza, M. Grasso, and B. M. Colosimo, "On the use of spatter signature for in-situ monitoring of Laser Powder Bed Fusion," *Additive Manufacturing*, vol. 16, pp. 35–48, Aug. 2017. [Online]. Available: https://linkinghub.elsevier.com/retrieve/pii/S2214860416303402

[58] EOS GmbH, *Operating Manual EOS M 290*, 2019.

[59] *EOS Titanium Ti64 Grade 5*, EOS GmbH, 4 2024. [Online]. Available: https://store.eos.info/products/eos-titanium-ti64-grade-5

[60] *Ancor Ti Alloys*, GKN Powder Metallurgy, 5 2024. [Online]. Available: https://www.gknpm.com/globalassets/downloads/additive-manufacturing/datasheets-am-materials/datasheets---titanium-alloys/ancorti-cp-6ai4v_a4.pdf/

[61] D. Sage, "OrientationJ: A series of ImageJ plugins for directional image analysis," https://bigwww.epfl.ch/demo/orientation/, 2017–2020, version 2.0.4.

[62] W. Rasband, "ImageJ," https://imagej.net/, 1987–2024, version 2.0.14/1.54f.

[63] Volume Graphics, *VG Studio Max v3.1*, 2019.

[64] J. H. Warner, S. P. Ringer, and G. Proust, "Strategies for metallic powder reuse in powder bed fusion: A review," *Journal of Manufacturing Processes*, vol. 110, pp. 263–290, 2024. [Online]. Available: https://www.sciencedirect.com/science/article/pii/S1526612523011714

[65] K. Kassym and A. Perveen, "Atomization processes of metal powders for 3d printing," *Materials Today: Proceedings*, vol. 26, pp. 1727–1733, 2020, 10th International Conference of Materials Processing and Characterization. [Online]. Available: https://www.sciencedirect.com/science/article/pii/S2214785320311196

[66] G. Chen, S. Zhao, P. Tan, J. Wang, C. Xiang, and H. Tang, "A comparative study of Ti-6Al-4V powders for additive manufacturing by gas atomization, plasma rotating electrode process and plasma atomization," *Powder Technology*, vol. 333, pp. 38–46, 2018. [Online]. Available: https://www.sciencedirect.com/science/article/pii/S0032591018302857

[67] E. Liverani, S. Toschi, L. Ceschini, and A. Fortunato, "Effect of selective laser melting (slm) process parameters on microstructure and mechanical properties of 316l austenitic stainless steel," *Journal of Materials Processing Technology*, vol. 249, pp. 255–263, 2017. [Online]. Available: https://www.sciencedirect.com/science/article/pii/S0924013617302169

[68] A. Kaletsch, S. Qin, S. Herzog, and C. Broeckmann, "Influence of high initial porosity introduced by Laser Powder Bed Fusion on the fatigue strength of Inconel 718 after post-processing with hot isostatic pressing," *Additive Manufacturing*, vol. 47, p. 102331, 2021. [Online]. Available: https://www.sciencedirect.com/science/article/pii/S2214860421004899

[69] M. Thöne, S. Leuders, A. Riemer, T. Tröster, and H. Richard, "Influence of heat-treatment of selective laser melting products-eg ti6al4v," *Texas ScholarWorks*, 2012.

[70] G. Kasperovich and J. Hausmann, "Improvement of fatigue resistance and ductility of tial6v4 processed by selective laser melting," *Journal of Materials Processing Technology*, vol. 220, pp. 202–214, 2015. [Online]. Available: https://www.sciencedirect.com/science/article/pii/S0924013615000278

[71] B. Meier, F. Warchomicka, J. Petrusa, P. Angerer, J. Wosik, R. Kaindl, V. Petrovic, W. Waldhauser, and C. Sommitsch, "Influence of powder production process and properties on material properties of ti6al4v manufactured by l-pbf," *The International Journal of Advanced Manufacturing Technology*, vol. 123, no. 5, pp. 1577–1588, Nov 2022. [Online]. Available: https://doi.org/10.1007/s00170-022-10250-y

[72] B. Diehl and A. Nassar, "Reducing near-surface voids in metal (Ti-6Al-4V) powder bed fusion additive manufacturing: the effect of inter-hatch travel time," *Additive Manufacturing*, vol. 36, p. 101592, 2020. [Online]. Available: https://www.sciencedirect.com/science/article/pii/S2214860420309647

[73] S. Ghods, R. Schur, E. Schultz, R. Pahuja, A. Montelione, C. Wisdom, D. Arola, and M. Ramulu, "Powder reuse and its contribution to porosity in additive manufacturing of Ti6Al4V," *Materialia*, vol. 15, p. 100992, 2021. [Online]. Available: https://www.sciencedirect.com/science/article/pii/S2589152920304087

[74] C. Barrett, C. Carradero, E. Harris, K. Rogers, E. MacDonald, and B. Conner, "Statistical analysis of spatter velocity with high-speed stereovision in laser powder bed fusion,"

Progress in Additive Manufacturing, vol. 4, no. 4, pp. 423–430, 2019. [Online]. Available: http://link.springer.com/10.1007/s40964-019-00094-6

[75] L. González-Fernández, E. Risueño, R. Pérez-Sáez, and M. Tello, "Infrared normal spectral emissivity of Ti–6Al–4V alloy in the 500–1150k temperature range," *Journal of Alloys and Compounds*, vol. 541, pp. 144–149, 2012. [Online]. Available: https://www.sciencedirect.com/science/article/pii/S0925838812011085

[76] L. Li, K. Yu, K. Zhang, and Y. Liu, "Study of Ti–6Al–4V alloy spectral emissivity characteristics during thermal oxidation process," *International Journal of Heat and Mass Transfer*, vol. 101, pp. 699–706, 2016. [Online]. Available: https://www.sciencedirect.com/science/article/pii/S0017931015310735

[77] J. Hatch, "GKN powder angle of repose," angle of repose for GKN powder used for UW 2020/2021 Capstone Builds.

[78] A. Montelione, "EOS powder Hall flow rates," hall flow rates for EOS powder used for UW RR Phase 1 builds.

Appendix A. PROPERTIES OF FEEDSTOCK POWDERS

A.1 GKN GA powder

Table A.1: Select properties of GKN GA powder used for printing.

GKN GA Powder AncorTi Ti6Al4V Grade 5A	HC Order Number: 100000014	Lot no: A 482001		
	Properties (Test Method)	Results (units)	min	max
Physical Analysis				
	Apparent Density (ASTM B212)	2.33 (g/cm^3)	-	-
Flowability				
	Angle of Repose (ASTM C1444-00)	36 (°) [77]	-	-
Particle Size Distribution				
	D10	15 (um)	7	17
	D50	28 (um)	20	30
	D90	45 (um)	40	50
Chemical Analysis				
	Aluminum	6.30 (%)	5.5	6.75
	Vanadium	4.1 (%)	3.5	4.5
	Iron	0.19 (%)	-	0.40
	Carbon	0.01 (%)	-	0.08

CERTIFICATE OF ANALYSIS

No. 20316 DATE: 03/19/20

Rev. 0

HOEGANAES SPECIALTY METAL POWDERS

Purchaser: University of Washington
Address: Nano Engineering & Sciences Building
3946 W Stevens Way NE
Seattle, WA 98195

PO Number: EI1089958

1001 Taylors Lane
Cinnaminson, NJ 08077
United States of America
Phone: 856-829-2220
Internet: www.gkn.com/hoeganaes/

Material Specifcation: AncorTi Ti6Al4V Grade 5A HC Order Number: 100000014

Lot No. 2007910001

Delivery Condition: Titanium Metal Powder - 10 to 45 micron Shipped Weight 40 kg

	PROPERTIES (Test Method)	*RESULTS*	*UNIT OF MEASURE*	*SPECIFICATIONS* Min	Max
Physical Analysis	Apparent Density (ASTM B212)	2.33	g/cm^3		
Particle Size Distribution					
	D10	15	µm	7	17
	D50	28	µm	20	30
	D90	45	µm	40	50
Chemical Analysis					
	Aluminum	6.30	%	5.5	6.75
	Vanadium	4.10	%	3.5	4.5
	Iron	0.19	%		0.40
	Carbon	0.01	%		0.08
	Nitrogen	0.01	%		0.05
	Oxygen	0.09	%		0.20
	Hydrogen	0.002	%		0.015
	Titanium	Balance			

Terms of Delivery: Specification
We hereby certify that the material described above has been tested and complies with the terms of the order.

REMARKS: FR0129/4

David Cernava

Approved By: David Cernava
Senior Advanced Powders Engineer

AP-003 REV 0 5/2015

Figure A.1: Certificate of analysis for GKN GA powder.

A.2 EOS PA powder

Table A.2: Select properties of EOS PA powder used for printing.

EOS PA Powder EOS Titanium Ti64	EOS product no. 9011-0039	Lot no: 2007910001		
	Properties (Test Method)	Results (units)	min	max
Physical Analysis				
	Apparent Density (ASTM B212)	2.59 (g/cm^3)	2.40	2.80
Flowability				
	Hall flow rate (ASTM B213-20)	27.5 (s/50 g) [78]	-	-
Particle Size Distribution				
	D10 (Dynamic Image Analysis)	30 (um)	22	32
	D50 (Dynamic Image Analysis)	41 (um)	34	44
	D90 (Dynamic Image Analysis)	57 (um)	49	61
Chemical Analysis				
	Aluminum (ICP-OES)	6.32 (%)	5.50	6.75
	Vanadium (ICP-OES)	4.02 (%)	3.50	4.50
	Iron (ICP-OES)	0.21 (%)	-	0.25
	Carbon (Combustion)	0.01 (%)	-	0.08
	Oxygen (Fusion)	0.15 (%)	-	0.15
	Titanium (ICP-OES)	Balance		

Inspection Certificate

EOS Titanium Ti64

Inspection certificate according to EN 10204, type 3.1

Trade name	EOS Titanium Ti64	Manufacturing method	Plasma atomized
EOS product no.	9011-0039	Date of manufacturing	11.12.2020
Lot number	A 482001		
Manufacturer	Electro Optical Systems Finland Oy Lemminkäisenkatu 36 FI-20520 Turku Finland Tel.: +358 (0)20 765 91 40 Quality_Control_FINLAND@eos.info	Supplier	EOS GmbH Electro Optical Systems Robert-Stirling-Ring 1 D-82152 Krailling Germany Tel.: +49 89 893 36 0

Declaration of conformance

As part of EOS quality assurance, the powder lot has been analyzed for powder properties and has been tested to work in EOS M machine. Parts built with this lot have been tested against EOS criteria and standard requirements.

Powder lot conforms to EOS requirements for powder, machine behavior, and solid part properties. The chemical composition and mechanical properties are in accordance with standards ISO 5832-3, ASTM F1472, ASTM F2924 and ASTM F3302.

Date: 11.12.2020

Approved by:

Marjaana Hovi

QA Specialist

Electro Optical Systems Finland Oy

Figure A.2: Certificate of analysis for EOS PA powder.

Inspection Certificate

Analyses of Powder (see page 4 for analysis details)

Sampling and Analysis Sample Preparation
Sampling of the quality assurance test batch and analysis sample preparation done according to ASTM B215.

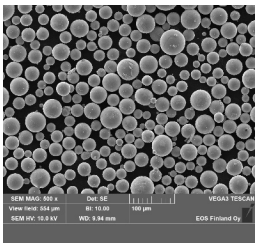

Cleanliness of Powder
Powder is visually free from foreign materials and uniform in condition.

Morphology
Powder is predominantly spherical with low levels of deformed particles.

Particle Size Distribution Analysis

Test method	Size characteristic	Limits	Result	✔/✖	Test Method	Size charateristic	Result
Laser diffraction	d10 **[µm]**	**22 - 32**	30	✔	Dynamic image analysis X_{Cmin}	x10 **[µm]**	24
	d50 **[µm]**	**34 - 44**	41	✔		x50 **[µm]**	37
	d90 **[µm]**	**49 - 61**	57	✔		x90 **[µm]**	50

Sieve Analysis

Fraction retained	Test Method	Limits	Result	✔/✖
≥ 63 µm **[wt%]**	Laboratory sieving	**Max. 0.5**	0.0	✔

Powder Density Analysis

Property	Test Method	Limits	Result	✔/✖
Apparent density **[g/cm³]**	ASTM B212	**2.40 - 2.80**	2.59	✔
Skeletal density **[g/cm³]**	Gas displacement	**N/A**	4.416	**N/A**

Powder Water Content Analysis

Property	Test Method	Limits	Result	✔/✖
Water content **[ppm]**	Coulometric KF titration	**Max. 125**	40	✔

Chemistry Analysis (External ISO 17025 accredited laboratory)

Element	Test Method	Limits [wt.%]	Result	✔/✖	Element	Test Method	Limits [wt.%]	Result	✔/✖
Ti	ICP-OES	**Balance**	Bal.	✔	N	Fusion	**Max. 0.04**	0.02	✔
Al	ICP-OES	**5.50 - 6.75**	6.32	✔	H	Fusion	**Max. 0.012**	0.002	✔
V	ICP-OES	**3.50 - 4.50**	4.02	✔	Y	ICP-OES	**Max. 0.005**	<0.001	✔
Fe	ICP-OES	**Max. 0.25**	0.21	✔	OE, each	ICP-OES	**Max. 0.10**	<0.10	✔
O	Fusion	**Max. 0.15**	0.15	✔	OE, total	ICP-OES	**Max. 0.40**	<0.40	✔
C	Combustion	**Max. 0.08**	0.01	✔					

Figure A.2: Certificate of analysis for EOS PA powder. (cont.)

Inspection Certificate

Analyses of Solid Part Properties (see page 4 for analysis details)

Following properties for this lot have been determined on additively manufactured solid parts using following system setup:

EOS M Machine: EOS M 290 400W
EOS Parameter Set: Ti64_PerformanceM291 1.1
Post Processing: Heat treatment 2 hours at 800 °C

Chemistry Analysis (External ISO 17025 accredited laboratory)

Element	Test Method	Limits [wt.%]	Result	✔/✖	Element	Test Method	Limits [wt.%]	Result	✔/✖
Ti	ICP-OES	**Balance**	Bal.	✔	N	Fusion	**Max. 0.05**	0.04	✔
Al	ICP-OES	**5.50 - 6.75**	6.20	✔	H	Fusion	**Max. 0.015**	0.004	✔
V	ICP-OES	**3.50 - 4.50**	4.00	✔	Y	ICP-OES	**Max. 0.005**	<0.001	✔
Fe	ICP-OES	**Max. 0.30**	0.19	✔	OE, each	ICP-OES	**Max. 0.10**	<0.10	✔
O	Fusion	**Max. 0.20**	0.16	✔	OE, total	ICP-OES	**Max. 0.40**	<0.40	✔
C	Combustion	**Max. 0.08**	0.01	✔					

Density

Density	Test Method	Limit	Result	✔/✖
Solid density **[g/cm³]**	ISO 3369	**Min. 4.4**	4.4	✔

Mechanical Properties (External ISO 17025 accredited laboratory)

Property	Test Method	Limit	Result	✔/✖
Yield strength, Rp0.2 **[MPa]**	ISO 6892-1 A14	**Min. 860**	1018	✔
Tensile strength, Rm **[MPa]**		**Min. 930**	1123	✔
Elongation, A **[%]**		**Min. 10**	13	✔

Figure A.2: Certificate of analysis for EOS PA powder. (cont.)

Appendix B. GRAYSCALE INTENSITY VARIATION CORRECTION

The images produced by the in-situ OT imaging system on the EOS M290 have a variation in brightness that depends on the distance between the location in the build space and the OT camera. However, it is possible to correct the images based on a polynomial fit of features in the image. A correction was applied to the data used in this research in order to more accurately quantify variations in grayscale intensty. The process for correcting images is presented here in the interest of producing future in-situ data that is more accurately representative of the LPBF process.

In case trends in grayscale intensity vary with build height, data from two different ranges of layer height was evaluated. The minimum and maximum height values for the layers examined are listed in Table B.1.

Figure B.1 identifies the footprints of the vertical specimens in the build space. There are 10 vertical specimens in each zone for 50 vertical specimens in total. The average grayscale intensity of each specimen footprint is identified as follows:

1. The average grayscale intensity for a single vertical specimen location for a single layer

Table B.1: Summary of image data examined for correction of grayscale intensity variation.

	Build / Set	Layer height minimum	Layer height maximum
EOS PA Powder	B1S1	203.4 (mm)	206.94 (mm)
	B6S1	203.4 (mm)	206.94 (mm)
	B1S2	215.04 (mm)	218.58 (mm)
	B6S2	215.04 (mm)	218.58 (mm)
GKN GA Powder	B1S1	64.26 (mm)	67.80 (mm)
	B6S1	64.26 (mm)	67.80 (mm)
	B1S2	75.24 (mm)	78.96 (mm)
	B6S2	75.24 (mm)	78.96 (mm)

image is measured.

2. The average grayscale intensity for the same vertical specimen location is measured for the remaining layer images.

3. The grayscale measurements obtained for the vertical specimen location of interest are averaged across layers to obtain an average grayscale intensity measurement for the given vertical specimen location.

4. Steps 1 through 3 are repeated for the remaining vertical specimen locations.

This produces a measurement of the average grayscale intensity for each of the 50 vertical specimens in a build. A relative representation of the intensity magnitude of each of the vertical specimens is shown in Figure B.2. The figure shows a trend in grayscale intensity that is greatest approximately in the center of the image and diminishes with increasing distance from the center. A generalized second-order polynomial function of x and y is defined in Equation B.1, where **A**-**I** are fit coefficients. Using the form defined by equation B.1, a fit in x and y is applied to the data to determine fit coefficients **A**-**I**.

$$f(x,y) = \mathbf{A} + \mathbf{B}x + \mathbf{C}y + \mathbf{D}x^2 + \mathbf{E}x^2y + \mathbf{F}y^2 + \mathbf{G}xy^2 + \mathbf{H}xy + \mathbf{I}x^2y^2 \tag{B.1}$$

The resulting fit for the data in UW Round Robin Build 1 is plotted in Figure B.3.

A correction factor is defined by equation B.2 where $f(x,y)$ is the interpolated grayscale intensity defined by equation B.1 with the fit coefficients calculated earlier. The correction factor is applied to each pixel in the layer image of interest as follows:

1. The average vertical specimen grayscale intensity, denoted as *avg. intensity*, is evaluated from the combined average of the average grayscale intensity of each of the 50 vertical specimen locations.

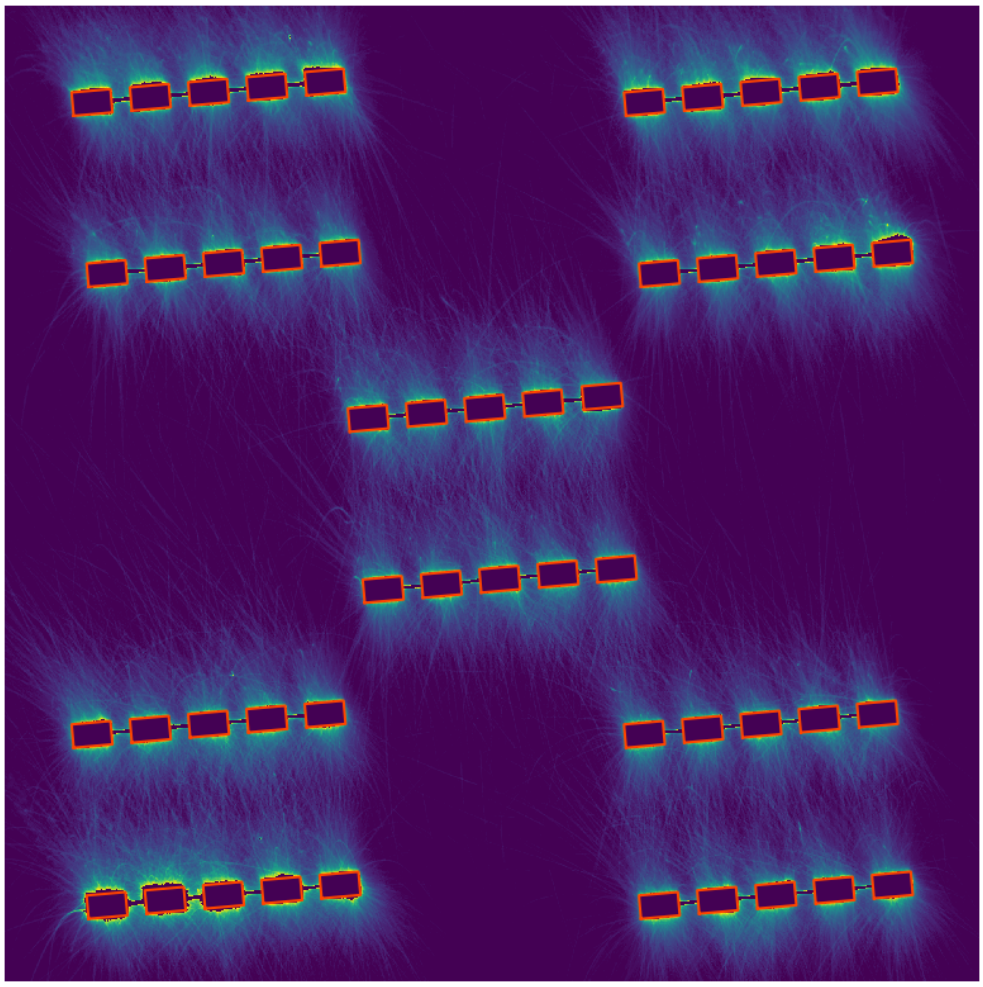

Figure B.1: Locations of vertical specimens in build space, boxed in orange.

2. The grayscale intensity of each pixel in the image is multiplied by the correction factor in equation B.2, where $f(x, y)$ is the fit polynomial defined by equation B.1.

3. Following correction of all pixels in the image, the same correction process is applied to the pixels in each of the remaining images.

4. To normalize the grayscale intensity of the set of images, first the average grayscale intensity for the set of images is evaluated.

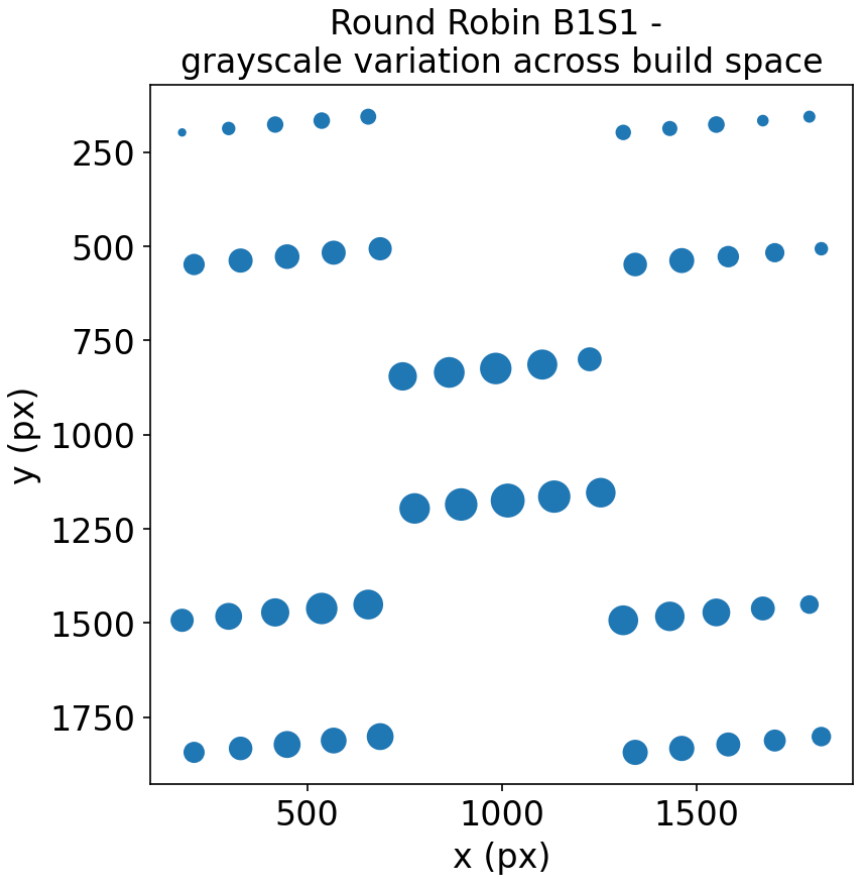

Figure B.2: Relative magnitude of vertical specimen grayscale intensity for UW Round Robin Build 1.

5. Next, the average grayscale intensity for the current layer is evaluated.

6. Each pixel in the current layer is multiplied by the normalization factor (average for all layers/average for current layer).

7. Steps 5 and 6 are repeated for the rest of the layer images.

$$\text{correction factor} = \frac{\text{avg. intensity}}{f(x,y)} \tag{B.2}$$

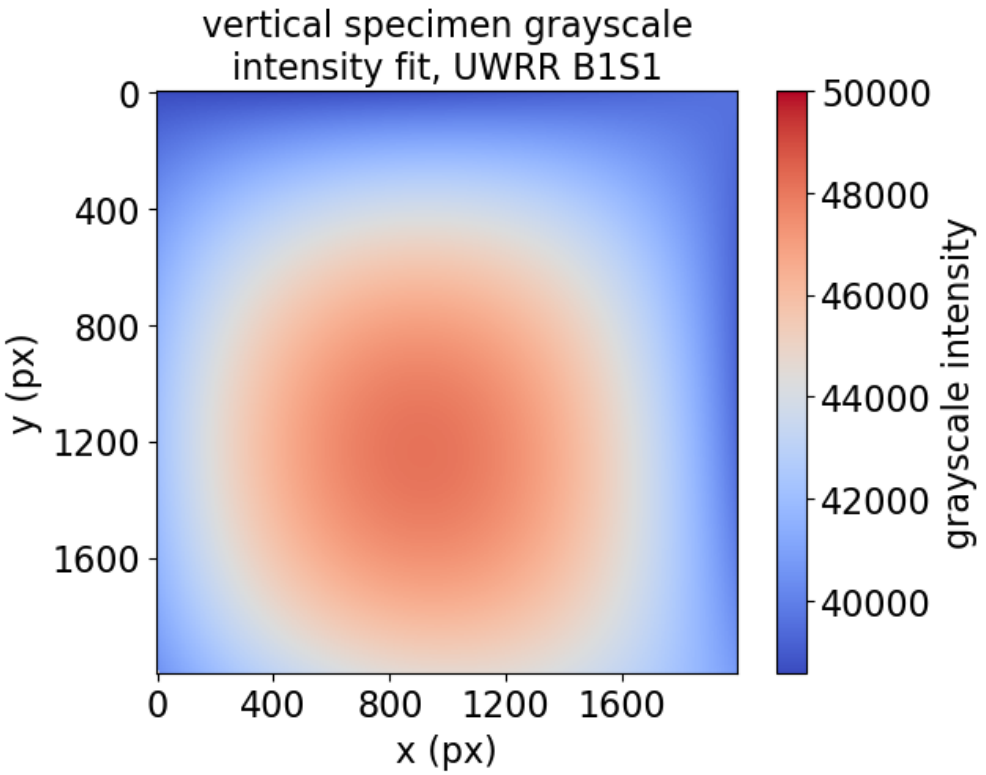

Figure B.3: Trend in spatial distribution of the grayscale intensity for UW Round Robin Build 1.

Following correction of the build data, a polynomial fit of the corrected data is presented in Figure B.4, plotted on the same scale as Figure B.3. The fit of the corrected vertical specimen grayscale intensity data has an RMSE of approximately 1.5% of the average value, and the difference between the minimum and maximum intensities is less than 8% of the average value. The uncorrected data has a difference between minimum and maximum intensities that is approximately 22% of the average value. While the vertical specimen grayscale intensity trend for the corrected data is still not completely uniform with no trend, the variation in grayscale intensity is about one-third as much.

In Figure B.3, there is a point of maximum grayscale intensity. Similar to a center of mass calculation, a center of intensity can be calculated using equation B.3, representing the point in the build space the OT camera is most sensitive to. Here Q_i represents the grayscale intensity of the

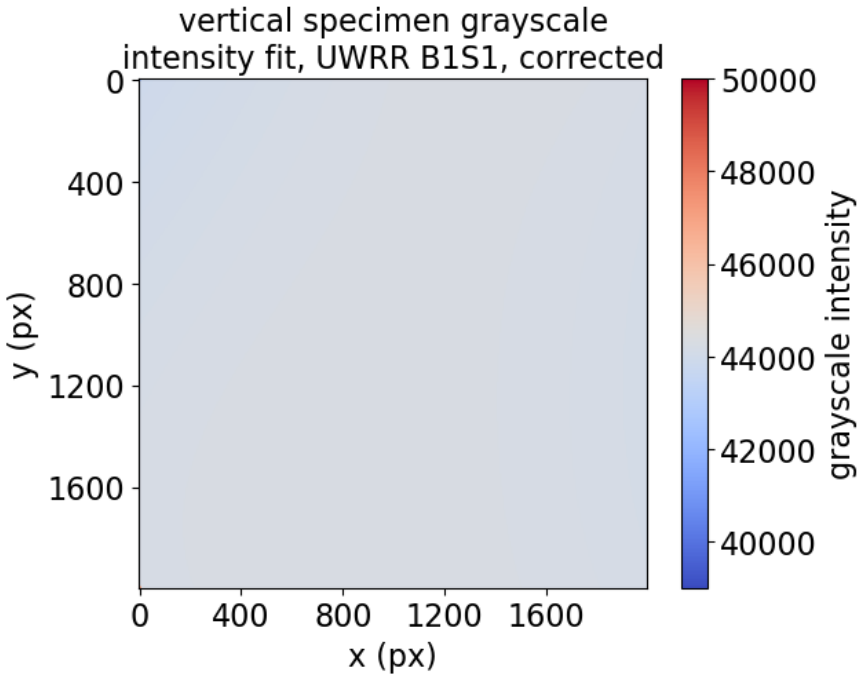

Figure B.4: Trend in grayscale intensity for UW Round Robin Build 1 following intensity variation correction.

pixel of interest, and x_i and y_i represent the x and y coordinates of the pixel.

$$x_{CM} = \frac{\sum Q_i x_i}{\sum Q_i}$$
$$y_{CM} = \frac{\sum Q_i y_i}{\sum Q_i}, \tag{B.3}$$

By plotting the grayscale intensity of the vertical specimen regions as a function of distance from the center of intensity, the dimensionality of the data is reduced from 2 to 1, facilitating comparison before and after the data is corrected for spatial variation in grayscale intensity. As shown in Figure B.5, after correction, the trend with respect to distance from the center of intensity is very nearly flat.

As mentioned previously, two sets of imaging data with different layer height ranges were analyzed in order to determine if similar trends exist at different build heights. An evaluation of

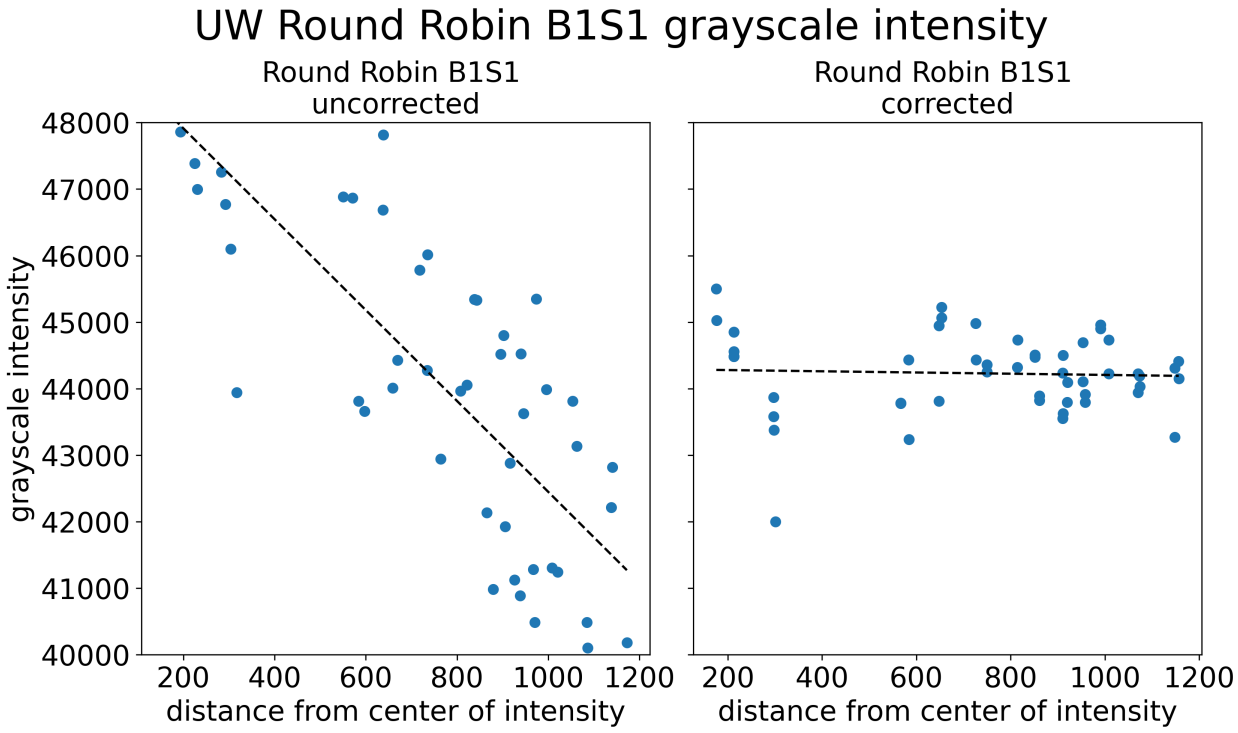

Figure B.5: Comparison of trend in vertical specimen grayscale intensity for UW Round Robin B1S1, before and after correcting for variation in grayscale intensity.

datasets 1 and 2 for Build 1 is shown in Figure B.6. In the plots shown, the size of the bubble represents the difference between the grayscale intensity of the corresponding vertical specimen and the average vertical specimen intensity. Orange indicates a grayscale intensity that is above average, and blue a grayscale intensity that is below average.

The two plots shown in Figure B.6 are similar, though there is variation. While the bubble representation shown in Figure B.6 is better at representing variations in intensity across the build space, it is easier to compare variations between datasets using the 1 dimensional form shown in Figure B.5.

Though the average grayscale intensity of the vertical specimen locations varies between builds, variations from average are of interest and build data can be adjusted to make direct comparisons. To do this, the data shown in Figure B.5 is evaluated for Build 1 Set 1 and Build 1 Set 2, and

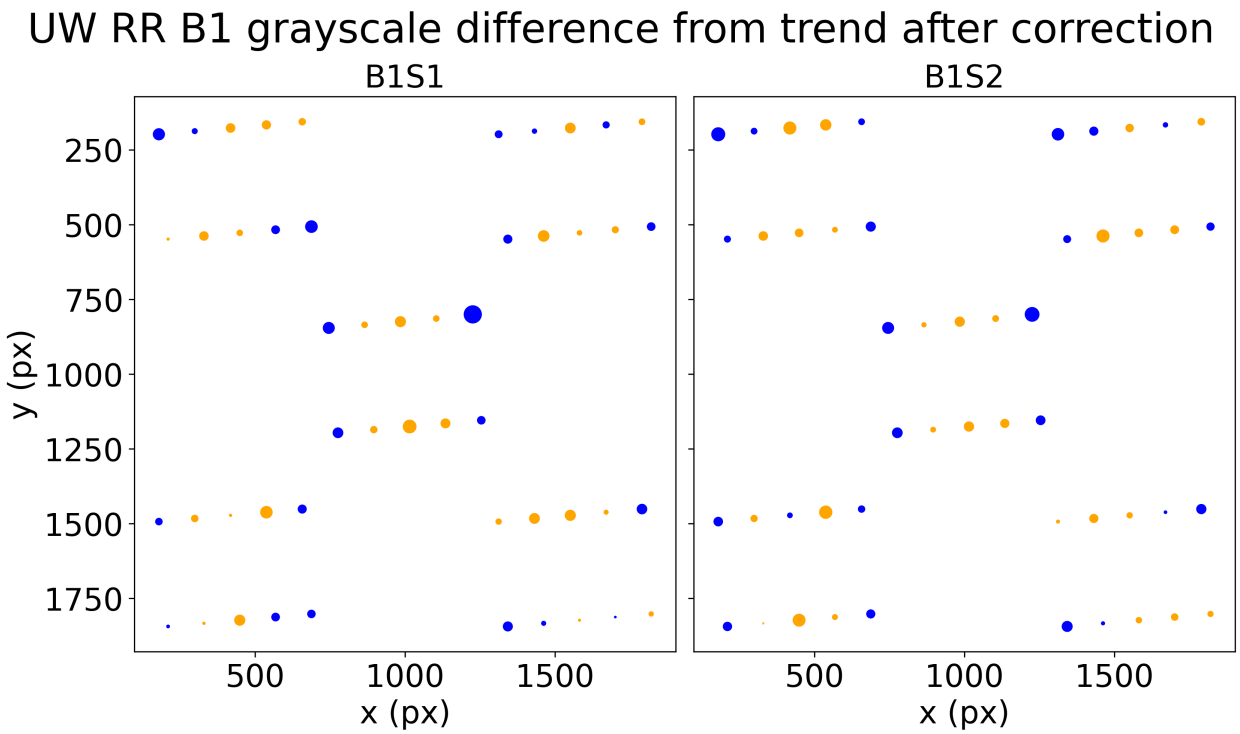

Figure B.6: UW Round Robin Build 1 Grayscale Intensity Variation Difference from Average.

the resulting data for Build 1 Set 1 is scaled such that the trendline for Build 1 Set 1 matches the trendline for Build 1 Set 2. This is shown in Figure B.7.

A similar trend is present in the data for Build 6, presented in Figure B.8.

The pattern of variation in vertical specimen grayscale intensity is persistent across different layer heights as well as between different builds. The nature of variation, particularly the oscillation in grayscale intensity with increasing distance from the center of intensity suggests there are influencing factors beyond variation in the distance from the camera. The origin of the additional factors is unknown at this time but this is a subject worthy of future investigation.

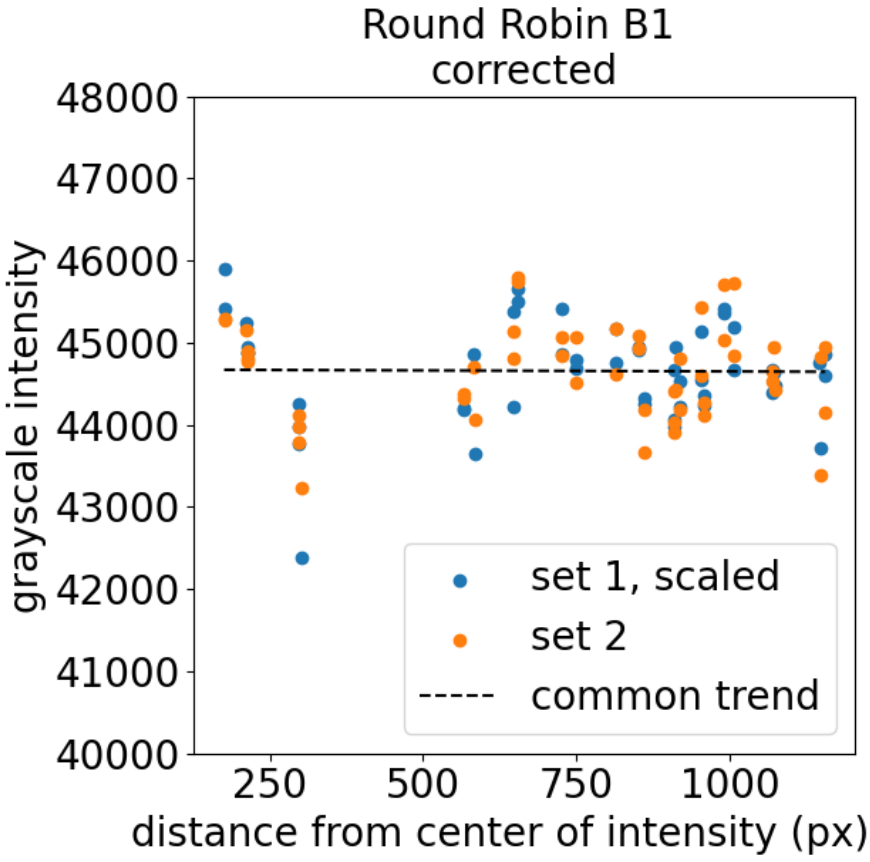

Figure B.7: Comparison of B1S1 and B1S2 grayscale intensity variation.

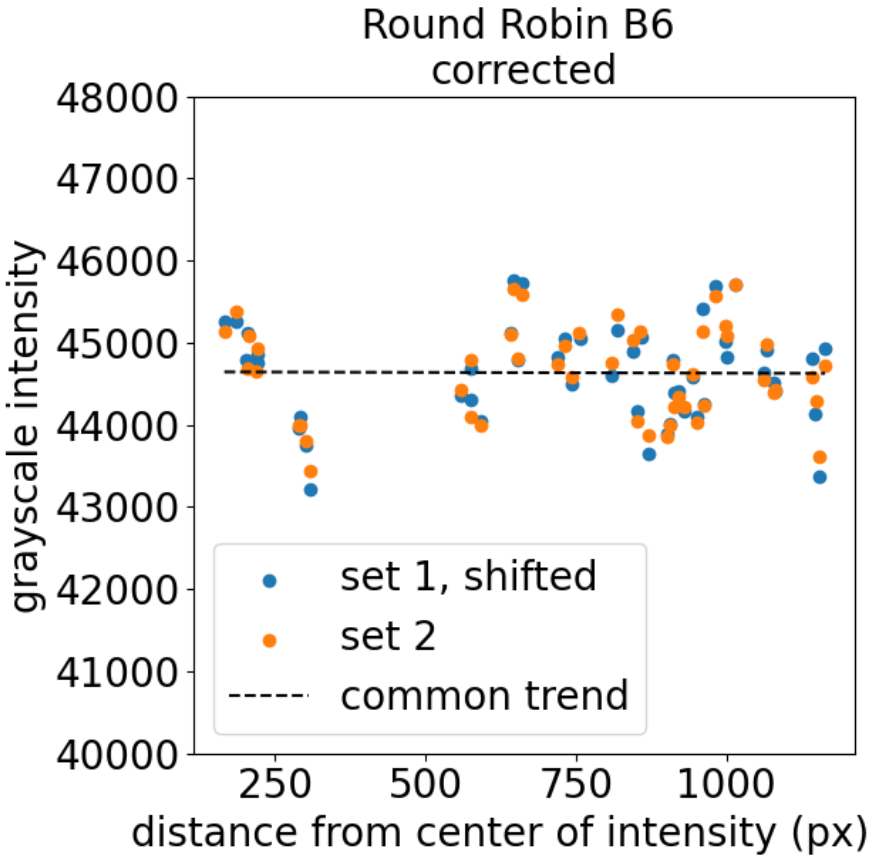

Figure B.8: Comparison of B6S1 and B6S2 grayscale intensity variation.

Appendix C. ADDITIONAL RESULTS

C.1 Direction of spatter trajectories

Table C.1: Slope of linear region of spatter angle difference plots for all zones.

	front	back
Z0	$-.302 \pm .070$	$-.370 \pm .070$
Z1	$-.473 \pm .086$	$-.665 \pm .076$
Z2	$-.504 \pm .095$	$-.269 \pm .089$
Z3	$-.384 \pm .078$	$-.303 \pm .083$
Z4	$-.266 \pm .088$	$-.415 \pm .120$

Table C.2: Slope of erratic region of spatter angle difference plots for all zones.

	front	back
Z0	2.8 ± 13.3	3.3 ± 16.1
Z1	40 ± 395	18 ± 340
Z2	7.1 ± 64.9	1.7 ± 41.3
Z3	3.8 ± 9.8	1 ± 52
Z4	2.3 ± 47.1	2.0 ± 24.4

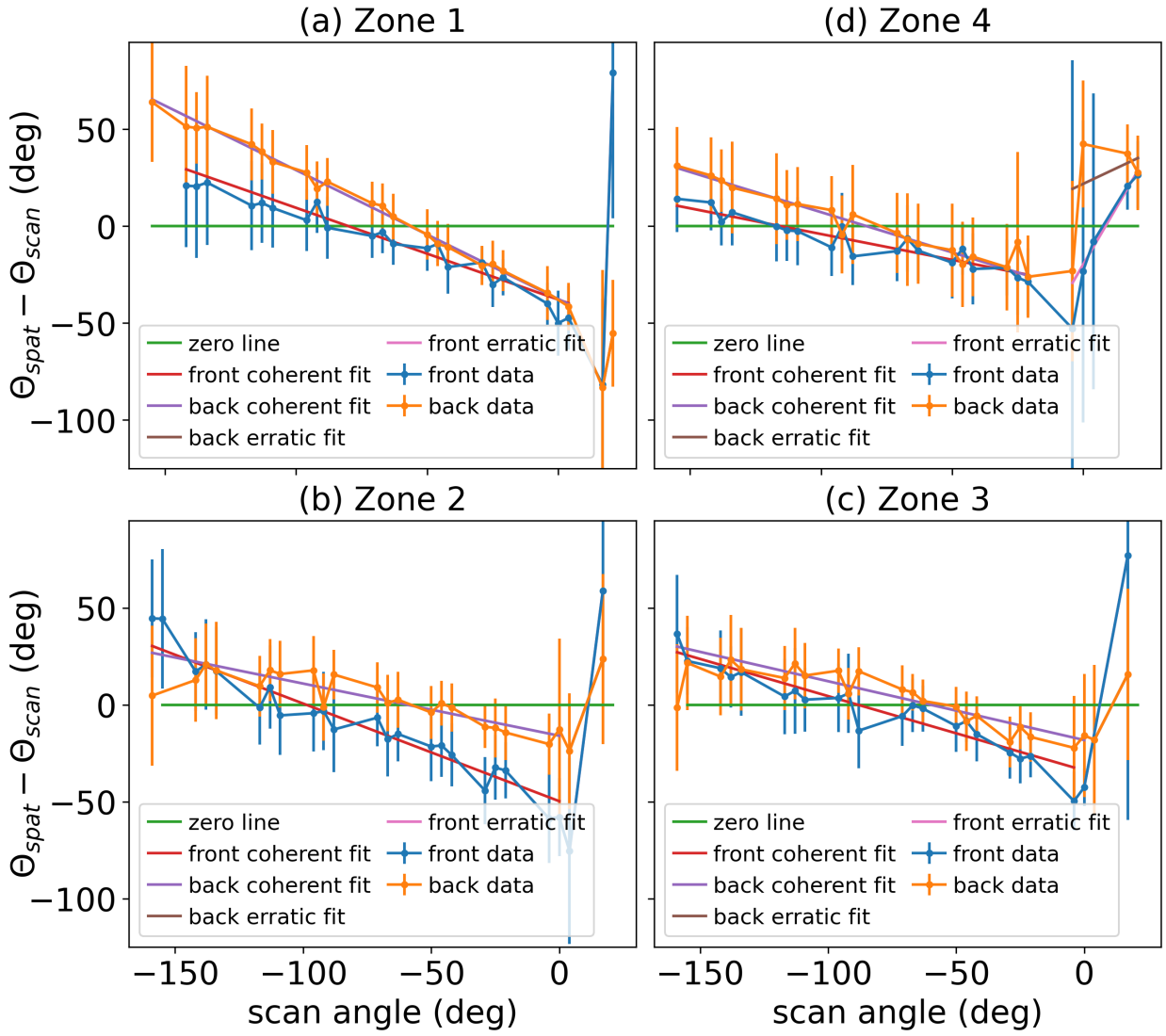

Figure C.1: Linear fit for the direction of the spatter trajectories in Zones 1 to 4, shown in (a) to (d), respectively, in terms of the scan angle data. The domain of the data has been rotated so the linear regions are presented uninterrupted. This data includes the spatter in the front and back ROIs.

C.2 Area Intensity

C.2.1 Fixed Distance from Specimen

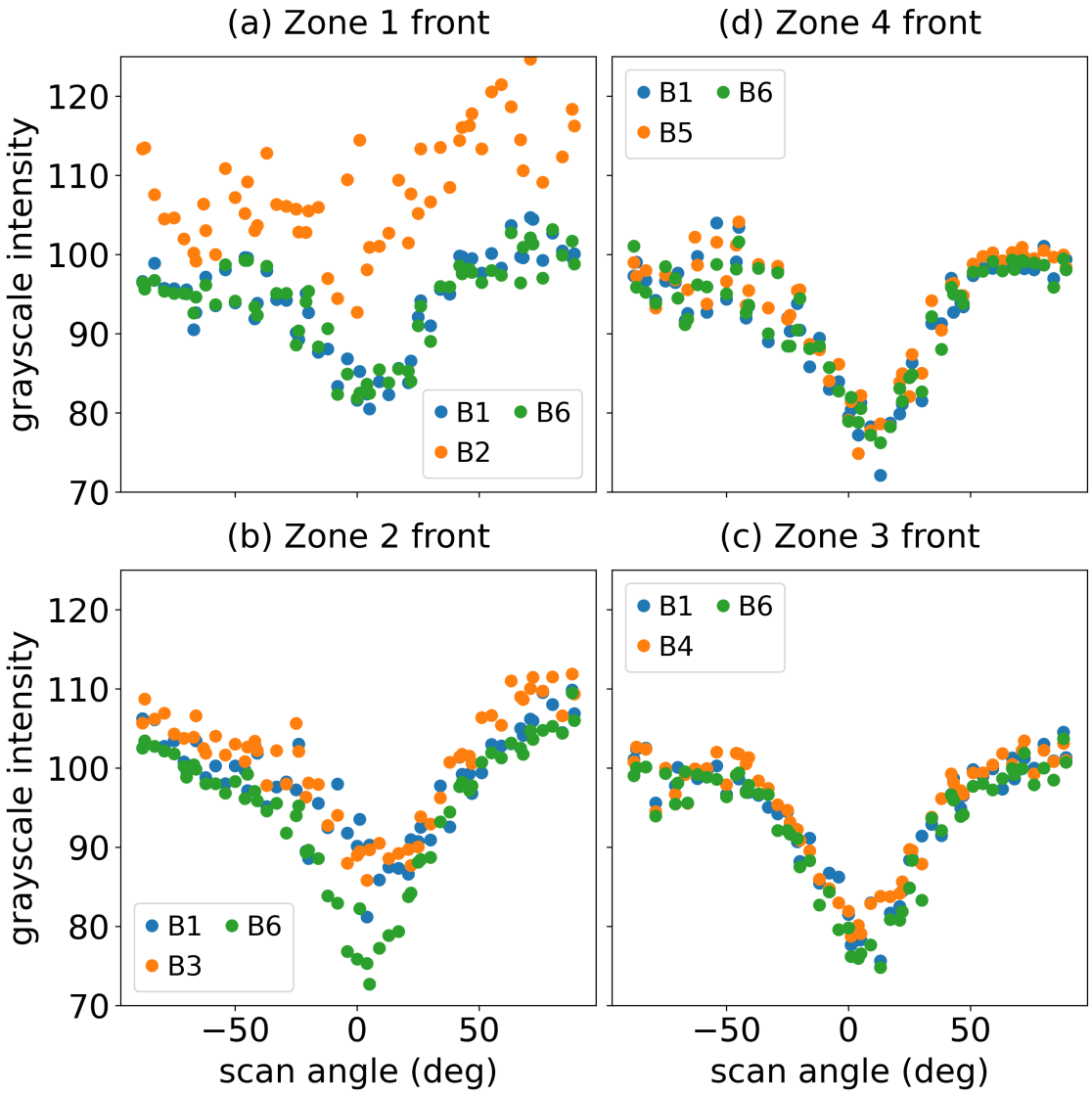

Figure C.2: The distribution of inter-specimen grayscale intensity for the front regions of Zones 1 to 4, shown in (a) to (d), respectively, that resulted from the builds performed with **GA powder**. The data presented here includes the grayscale intensity distributions for six builds.

C.2.2 Variation in spatter intensity with distance

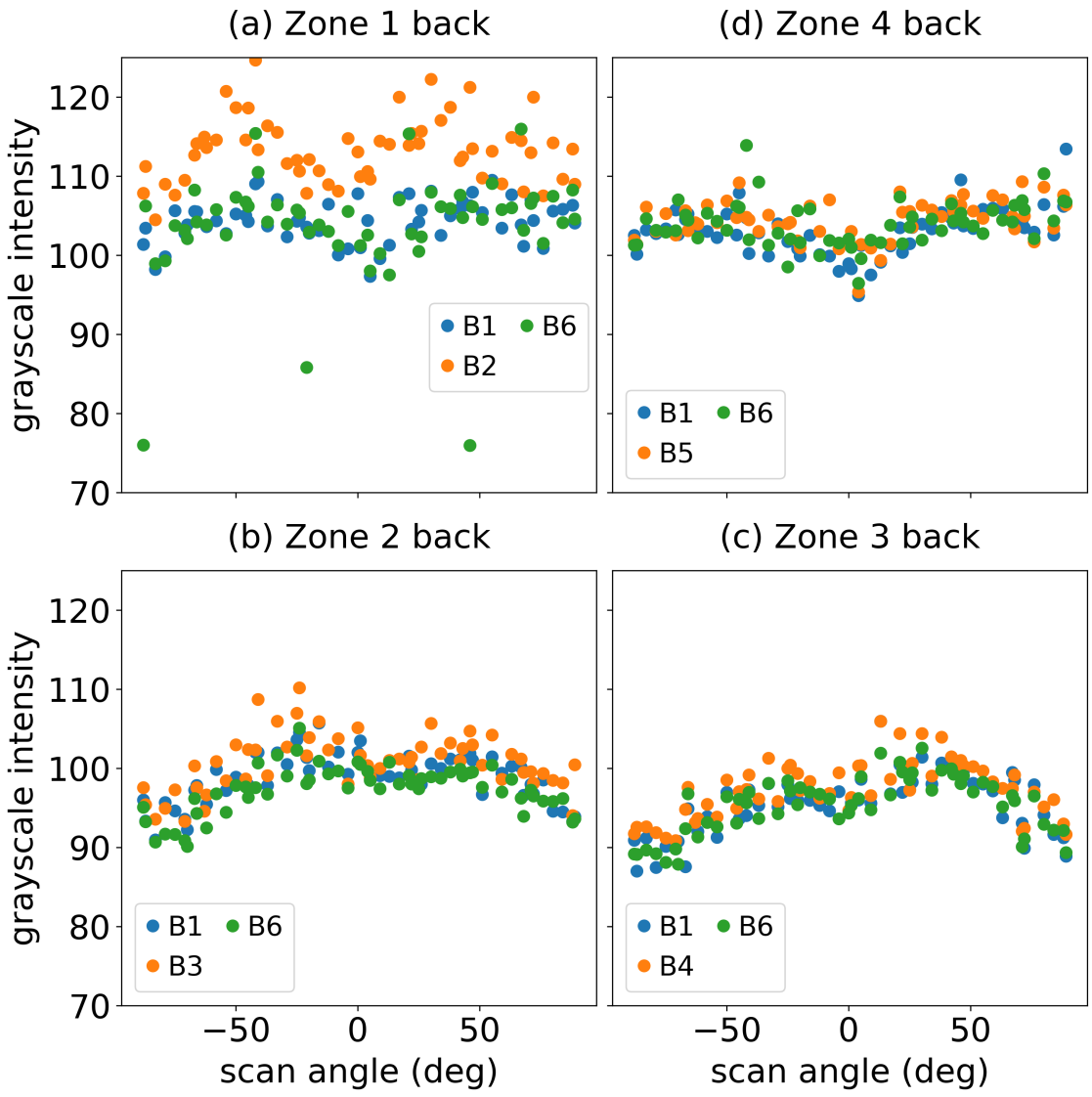

Figure C.3: The distribution of inter-specimen grayscale intensity for the back regions of Zones 1 to 4, shown in (a) to (d), respectively, that resulted from the builds performed with **GA powder**. The data presented here includes the grayscale intensity distributions for six builds.

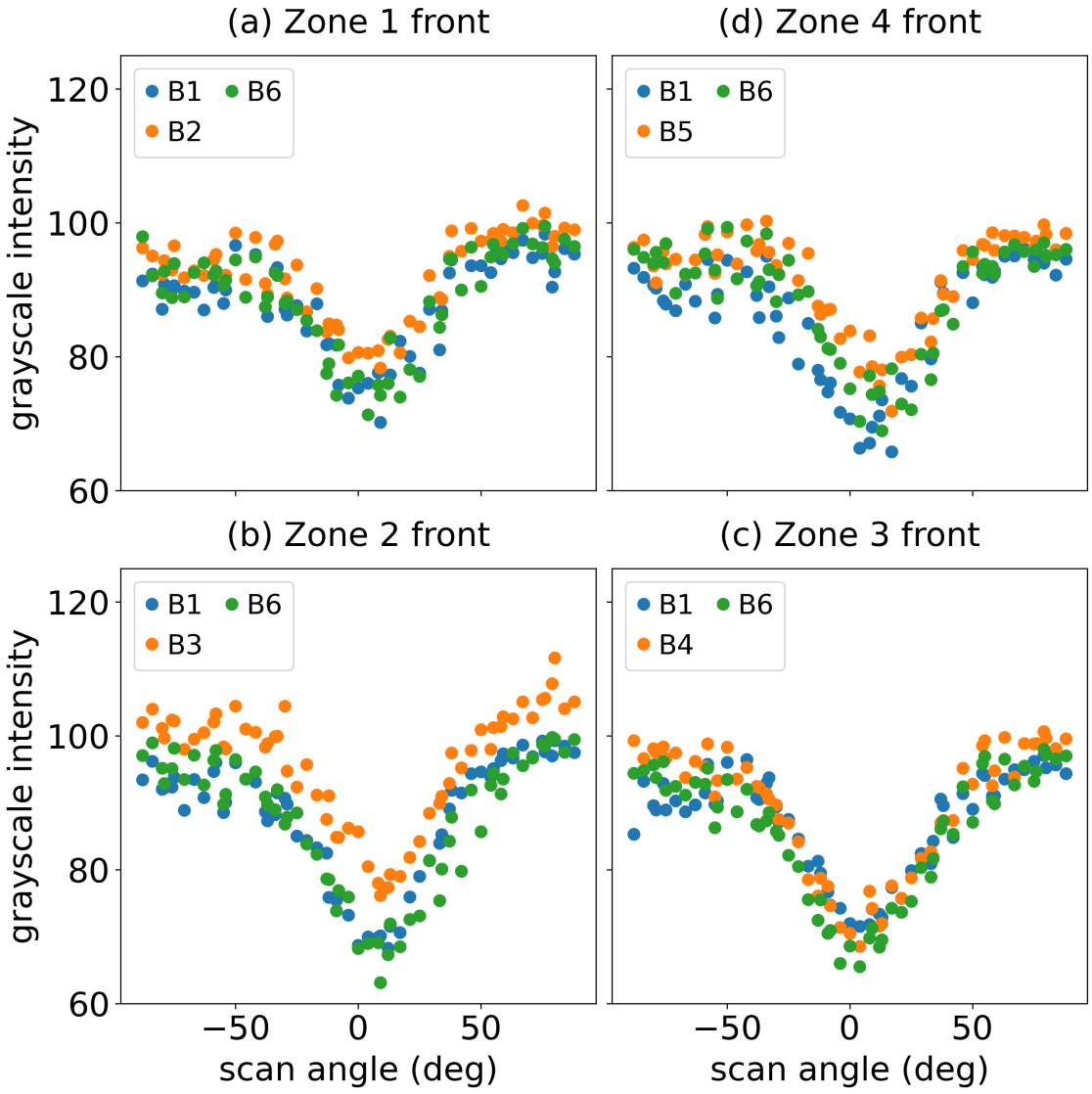

Figure C.4: The distribution of inter-specimen grayscale intensity for the front regions of Zones 1 to 4, shown in (a) to (d), respectively, that resulted from the builds performed with **PA powder**. The data presented here includes the grayscale intensity distributions for six builds.

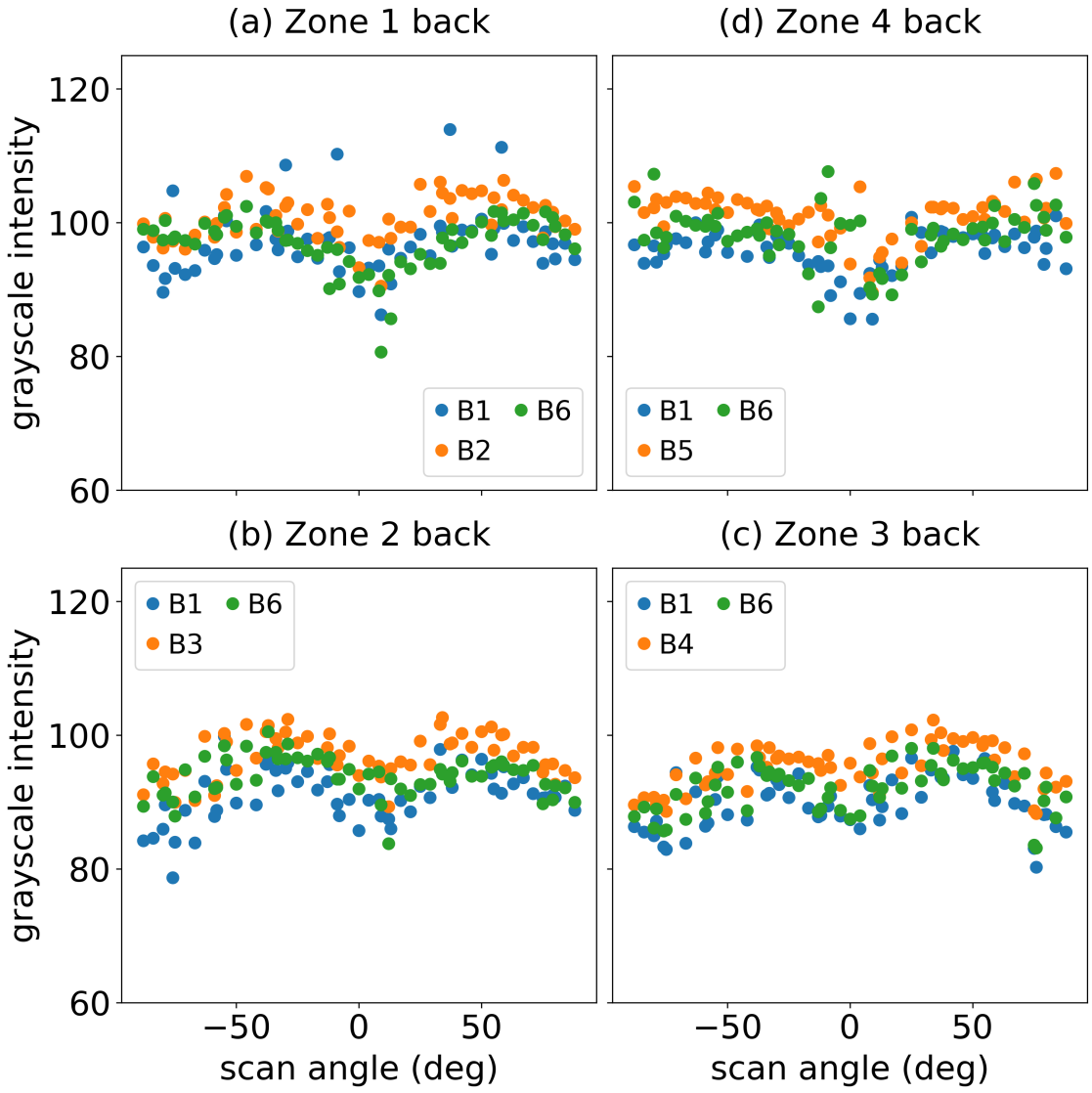

Figure C.5: The distribution of inter-specimen grayscale intensity for the back regions of Zones 1 to 4, shown in (a) to (d), respectively, that resulted from the builds performed with **PA powder**. The data presented here includes the grayscale intensity distributions for six builds.

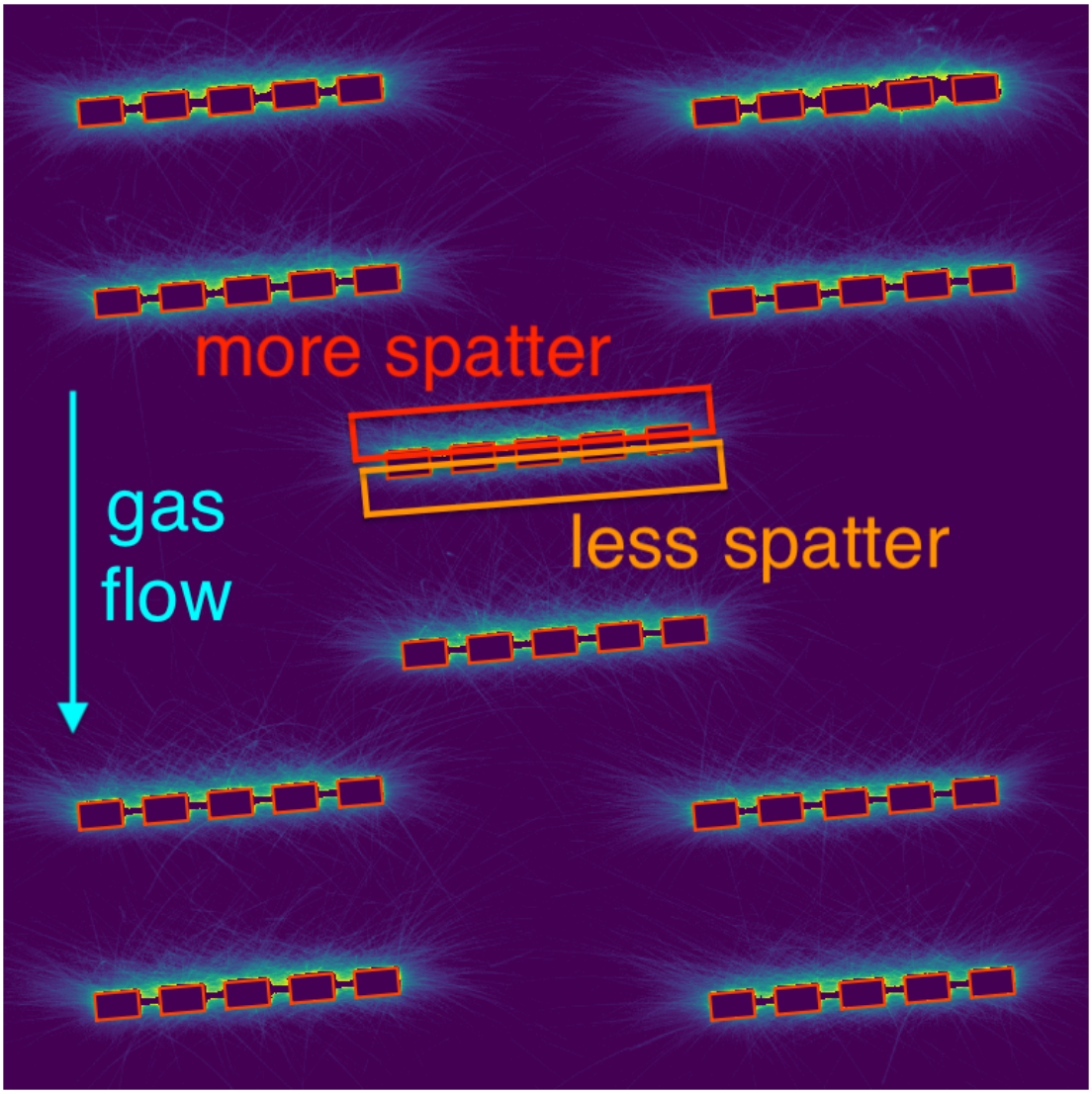

Figure C.6: OT image of build space at a scan angle of 0° (horizontal), showing more spatter content on the back-facing sides of the specimens than on the front-facing sides. This image is of layer 1079 from PA powder Build 6. Overall, there is less spatter content in this image than in layer images for builds produced with GA powder, but this image exhibits more spatter on the back-facing sides of the printed regions (red) than on the front facing sides (orange).

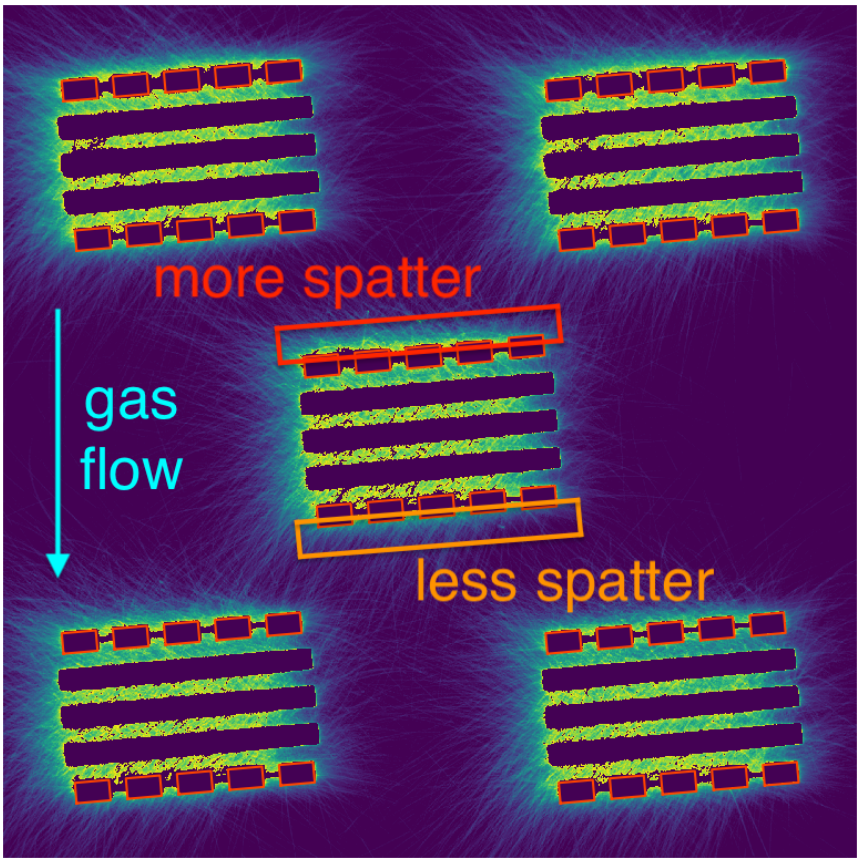

Figure C.7: OT image of build space at a scan angle of 0° (horizontal), showing more spatter content on the back-facing sides of the specimens than on the front-facing sides. This image is of layer 1079 from PA powder Build 6. This image contains additional spatter content since in this layer support material for the horizontal specimens is also being printed, though comparison of the back-facing side of Zone 0 (red) to the front facing side (orange) shows the grayscale intensity and thus spatter content on the back-facing side is greater.

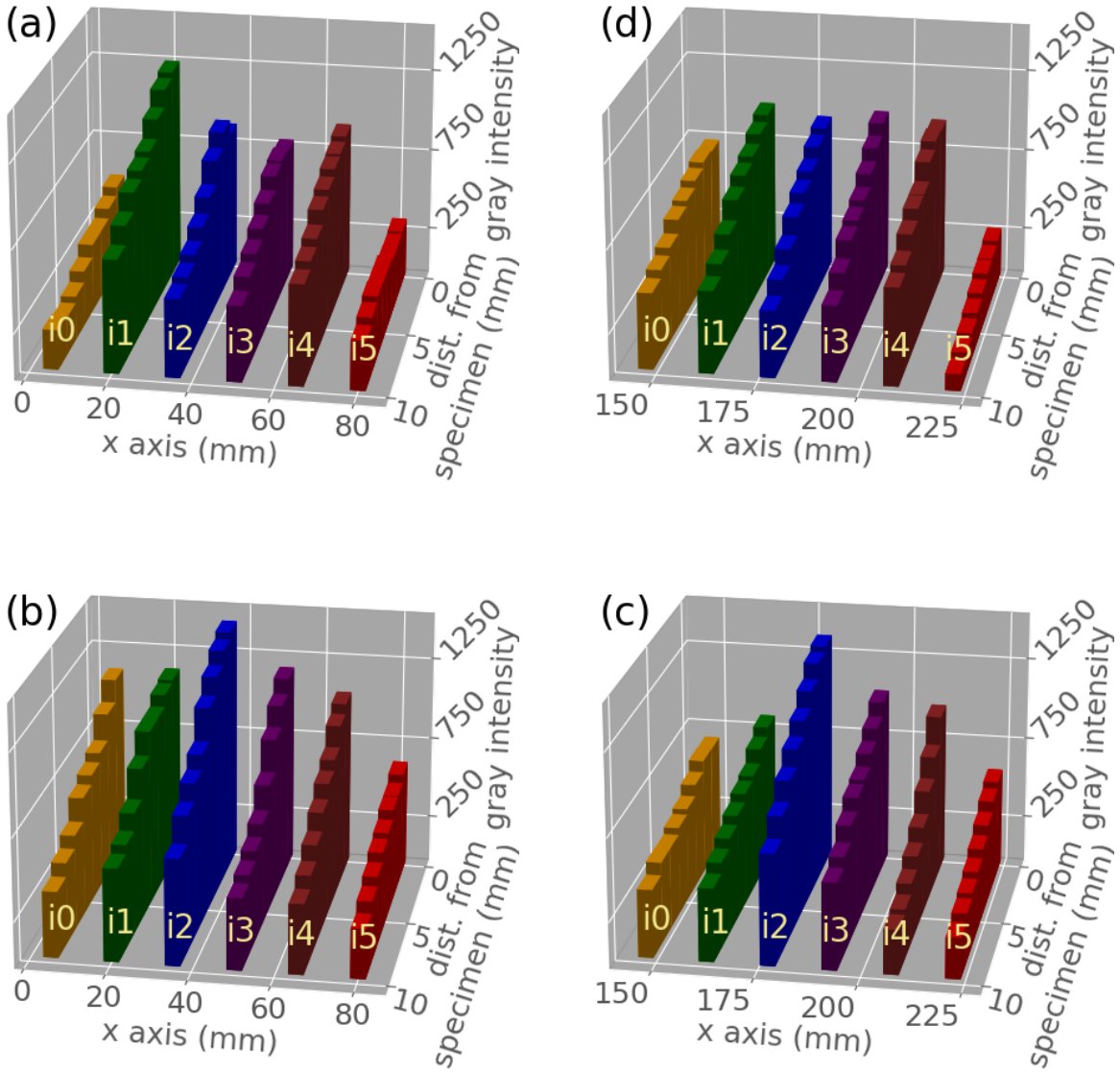

Figure C.8: Inter-specimen grayscale intensity for Zones 1 to 4, shown in (a) to (d), respectively, in the front ROIs and in LPBF with a scan angle = 88°. This data is for builds produced with **PA powder**. Notable features include an oscillation in grayscale intensity adjacent to the specimens in Zone 1 and a mostly constant level of grayscale intensity for sub-ISR Zone 1, i5 in (a).

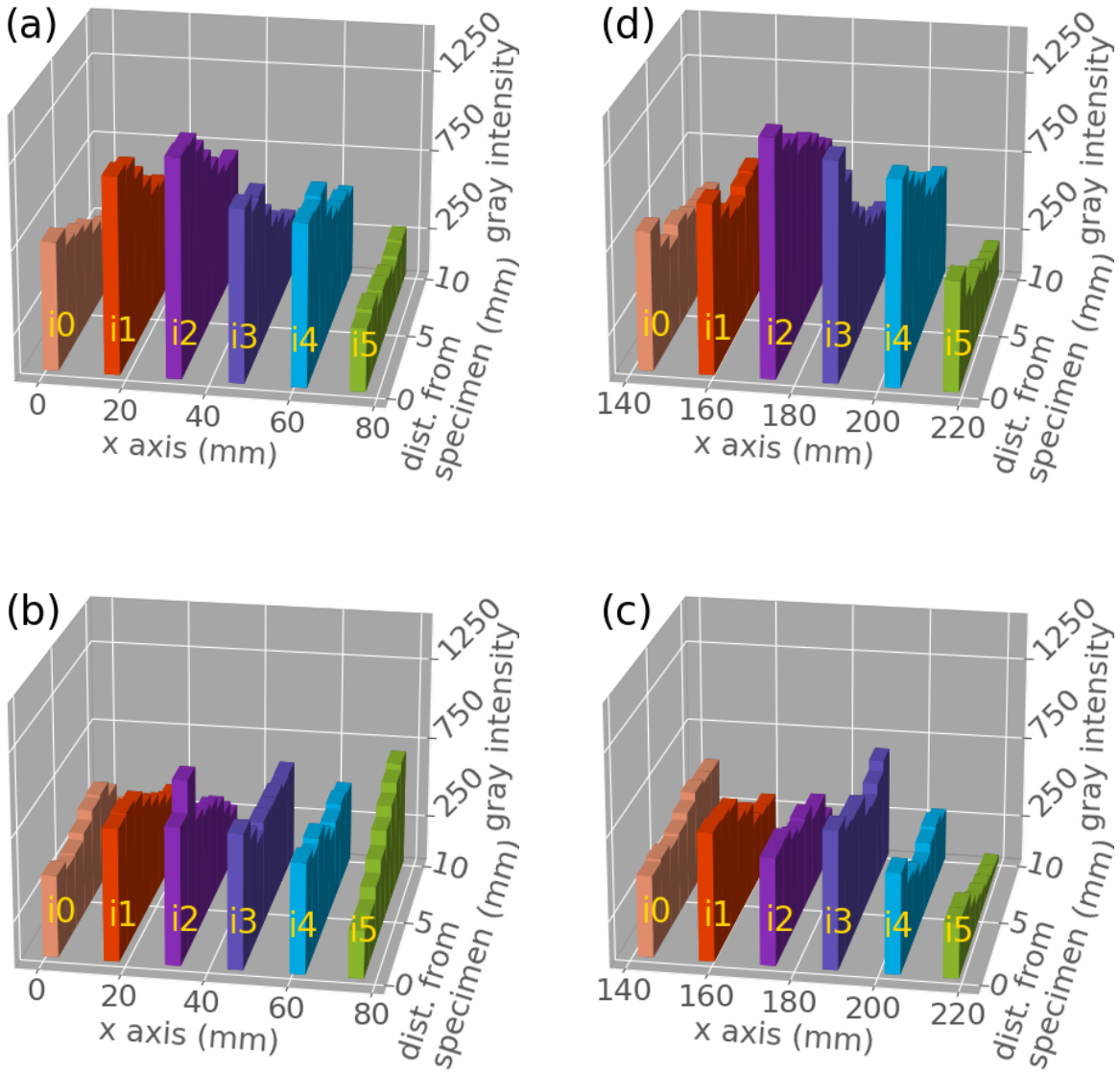

Figure C.9: Inter-specimen grayscale intensity for Zones 1 to 4, shown in (a) to (d), respectively, in the back ROIs and in LPBF with a scan angle = 88°. This data is for builds produced with **PA powder**. Notable features include a mostly constant level of grayscale intensity for Zone 1, i5 in (a), a reversal (increase) in grayscale intensity in Zone 2, i5 in (b), and an oscillation in grayscale intensity adjacent to the specimens in Zone 3 in (c).

C.3 Comparison to Specimen Porosity

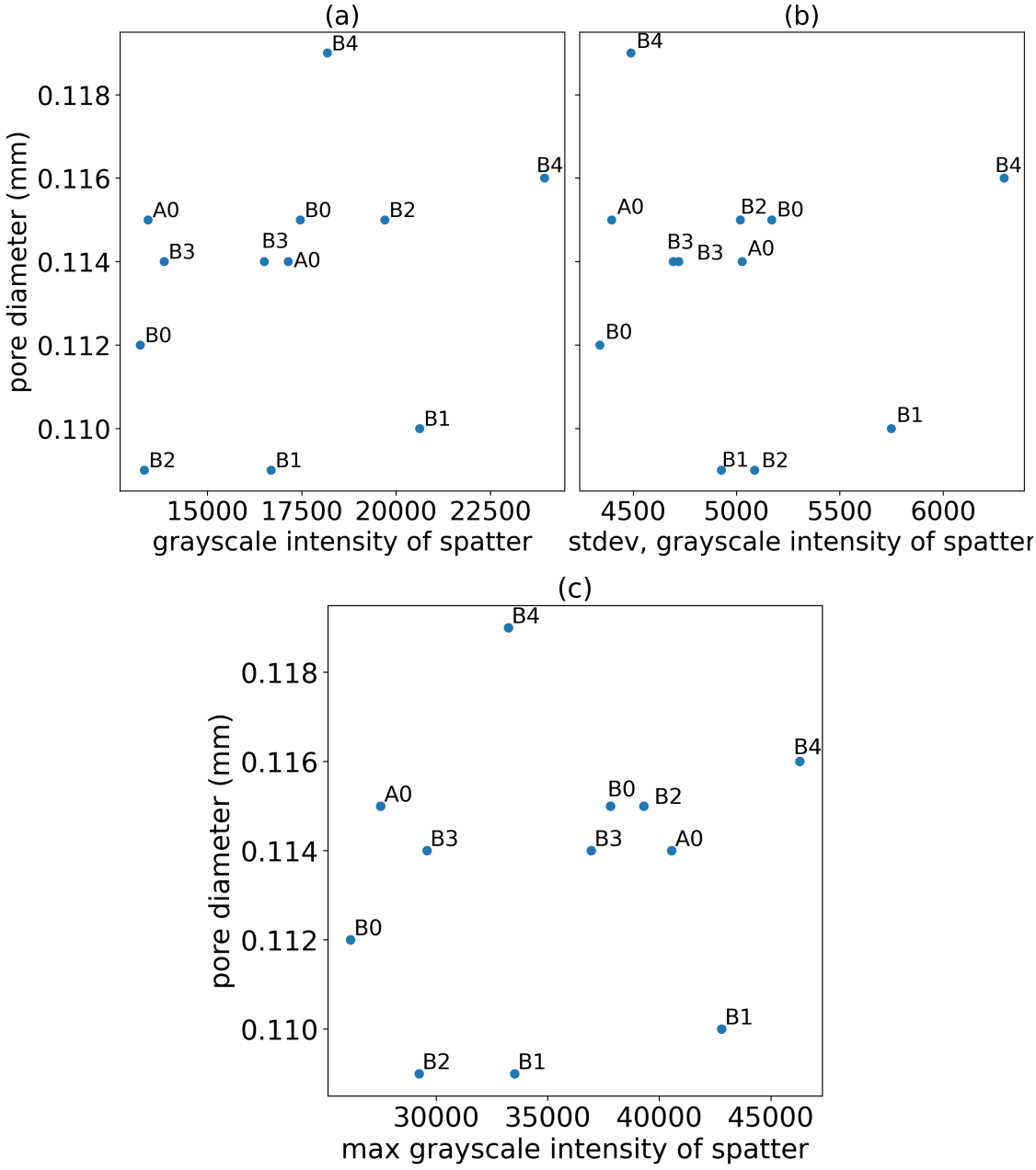

Figure C.10: Evaluation of the pore diameter in terms of the (a) grayscale intensity, (b) standard deviation in grayscale intensity, and (c) maximum grayscale intensity.

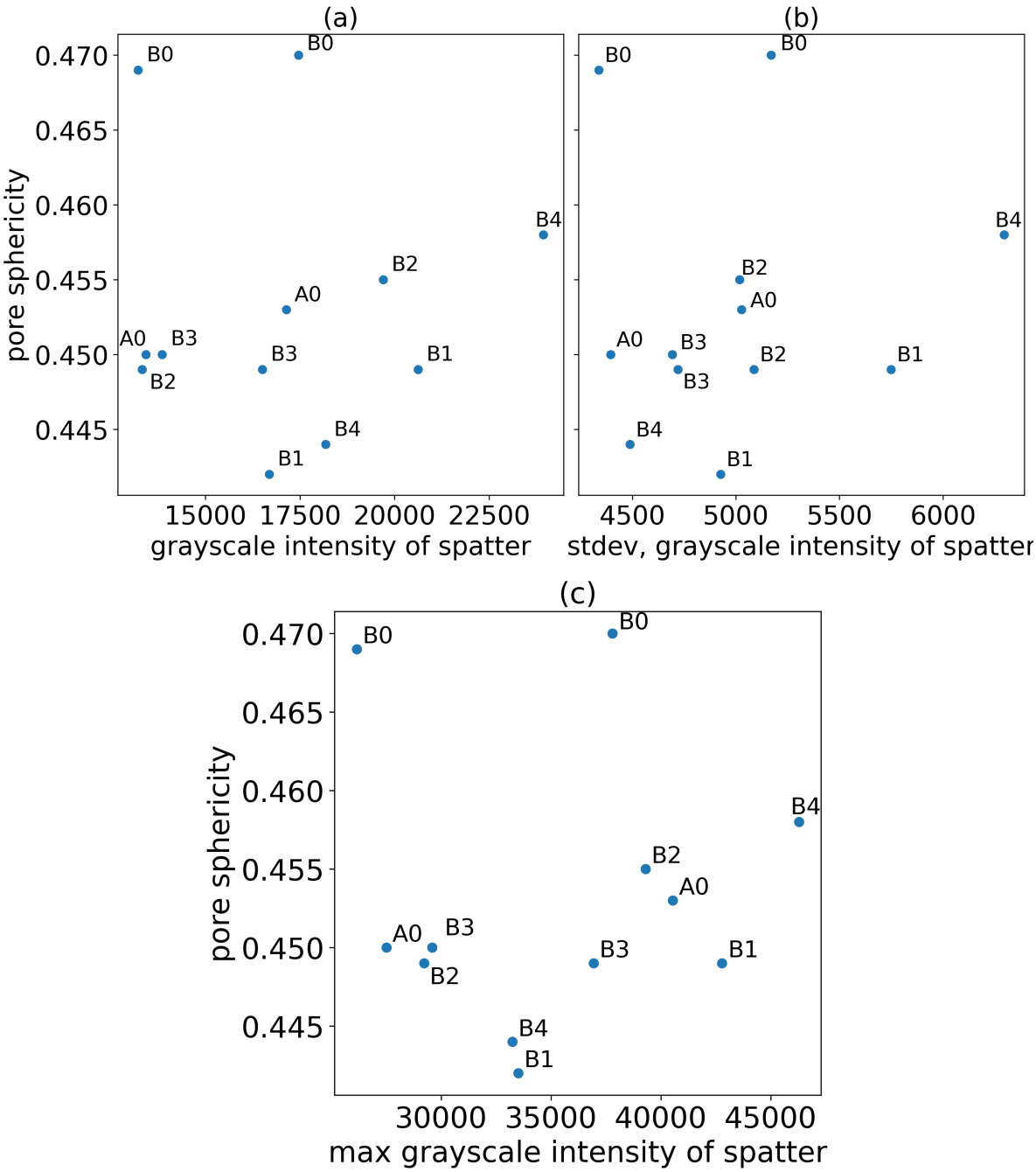

Figure C.11: Evaluation of the pore sphericity in terms of the (a) grayscale intensity, (b) standard deviation in grayscale intensity, and (c) maximum grayscale intensity.

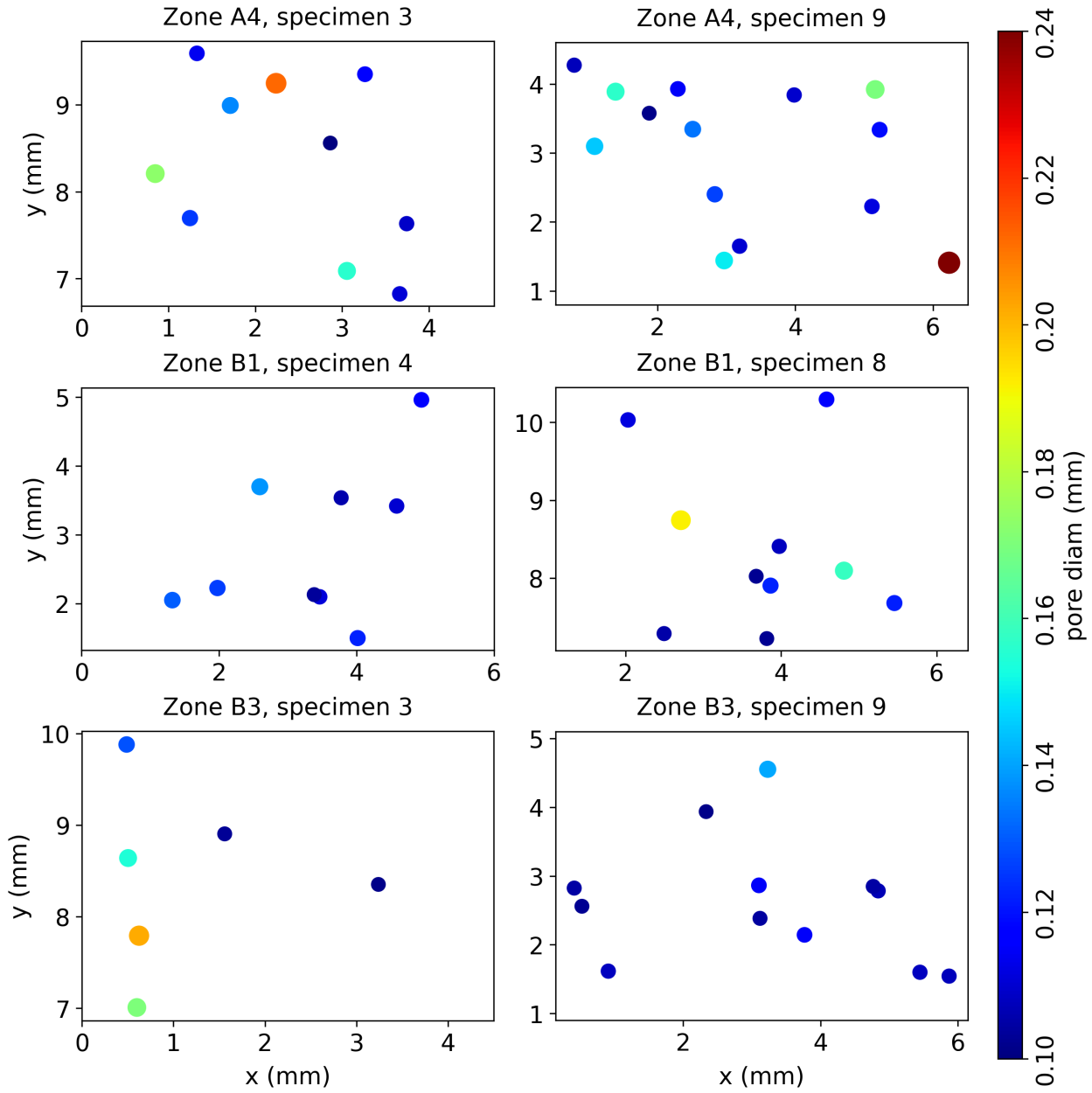

Figure C.12: Pore locations in select specimens for UW Round Robin Build 1, performed with **PA powder**. This shows pores as observed along the axis of the vertical specimen. Pores with a circular equivalent diameter less than 100 μm have been omitted. The sizes of the dots are proportional to the circular equivalent diameter of the corresponding pore but have been exaggerated for easier visibility (i.e. pores are not to scale with the plot axes.)

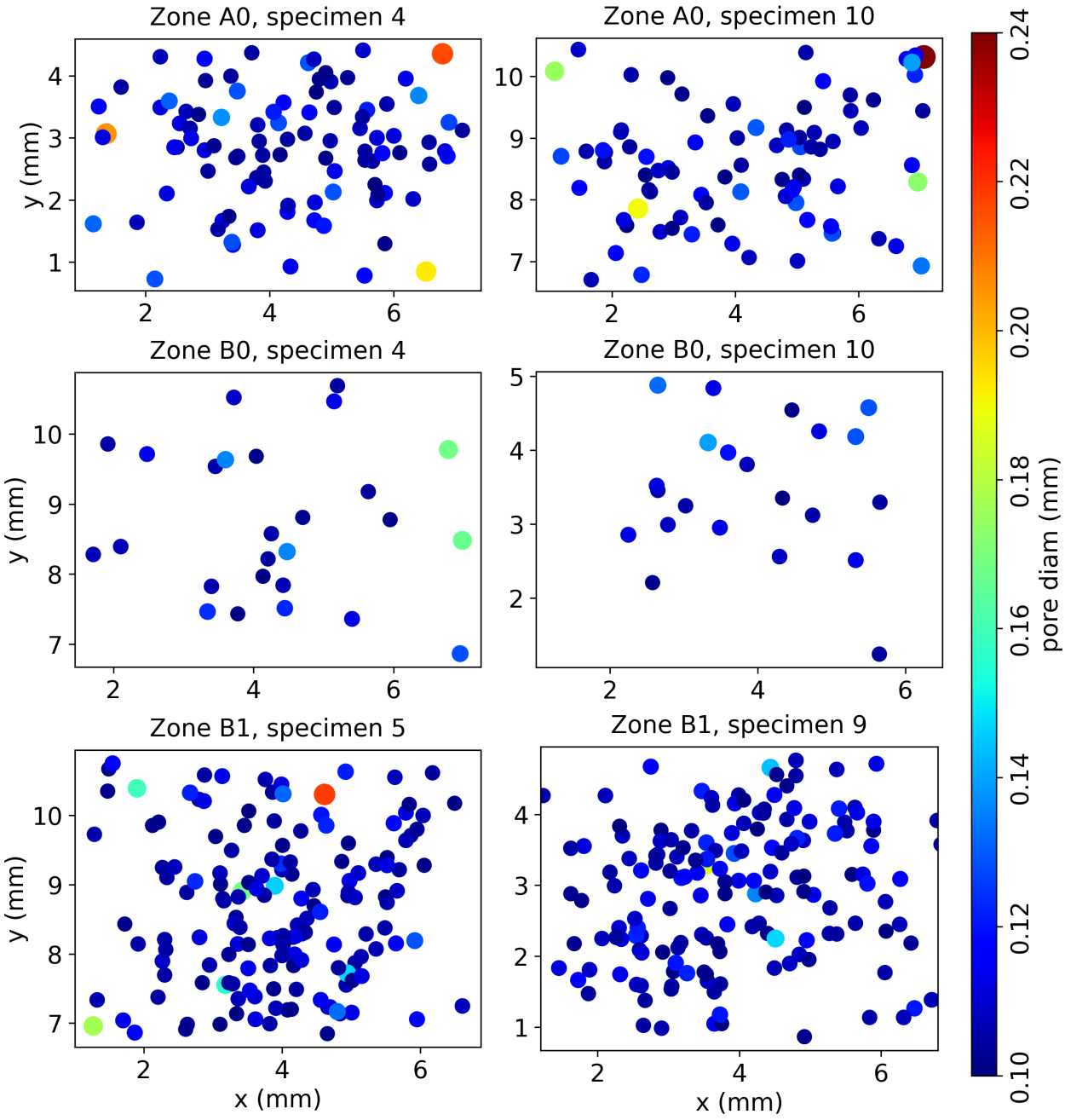

Figure C.13: Pore locations in select specimens for UW Round Robin Build 6, performed with **PA powder**. This shows pores as observed along the axis of the vertical specimen. Pores with a circular equivalent diameter less than 100 μm have been omitted. The sizes of the dots are proportional to the circular equivalent diameter of the corresponding pore but have been exaggerated for easier visibility (i.e. pores are not to scale with the plot axes.)

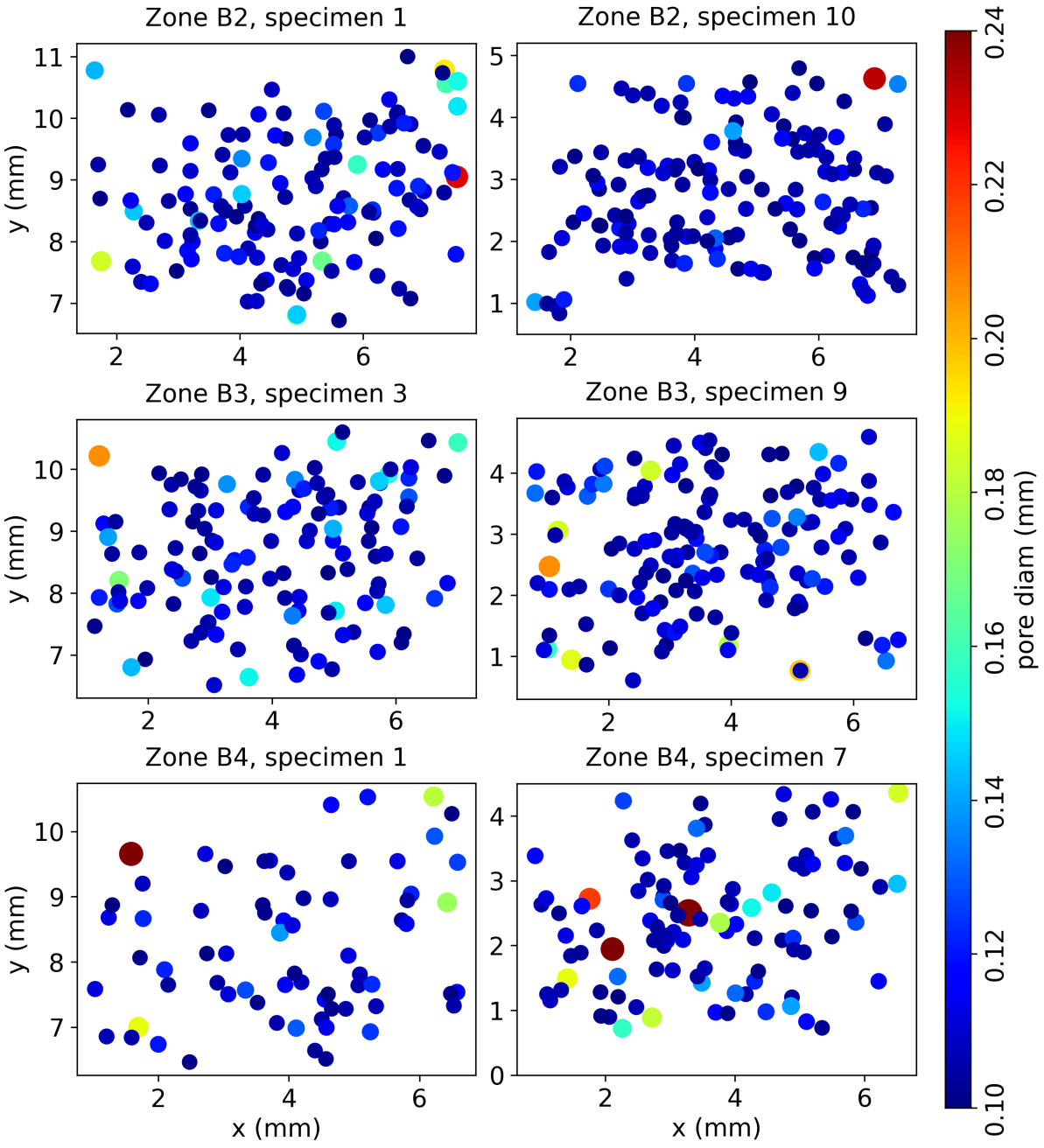

Figure C.14: Pore locations in select specimens for UW Round Robin Build 6, performed with **PA powder**. This shows pores as observed along the axis of the vertical specimen. Pores with a circular equivalent diameter less than 100 μm have been omitted. The sizes of the dots are proportional to the circular equivalent diameter of the corresponding pore but have been exaggerated for easier visibility (i.e. pores are not to scale with the plot axes.)

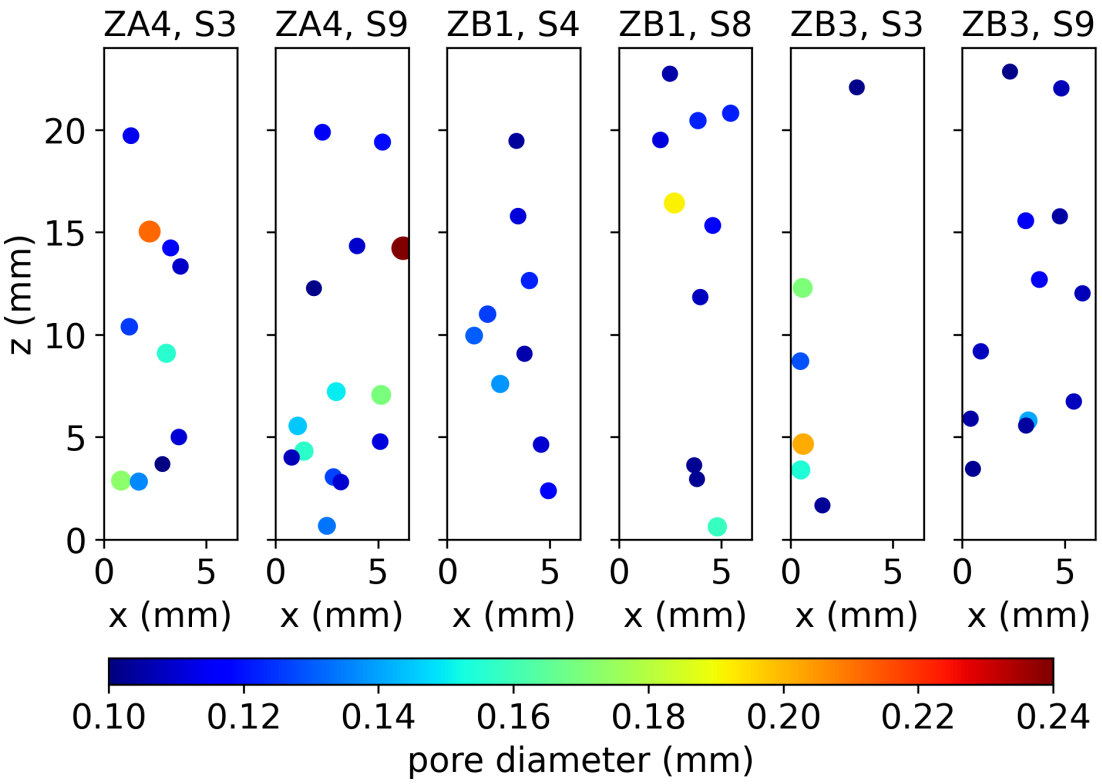

Figure C.15: Pore locations in select specimens for UW Round Robin Build 1, performed with **PA powder**. This shows pores as observed across the height of the vertical specimen. Pores with a circular equivalent diameter less than 100 μm have been omitted. The sizes of the dots are proportional to the circular equivalent diameter of the corresponding pore but have been exaggerated for easier visibility (i.e. pores are not to scale with the plot axes.)

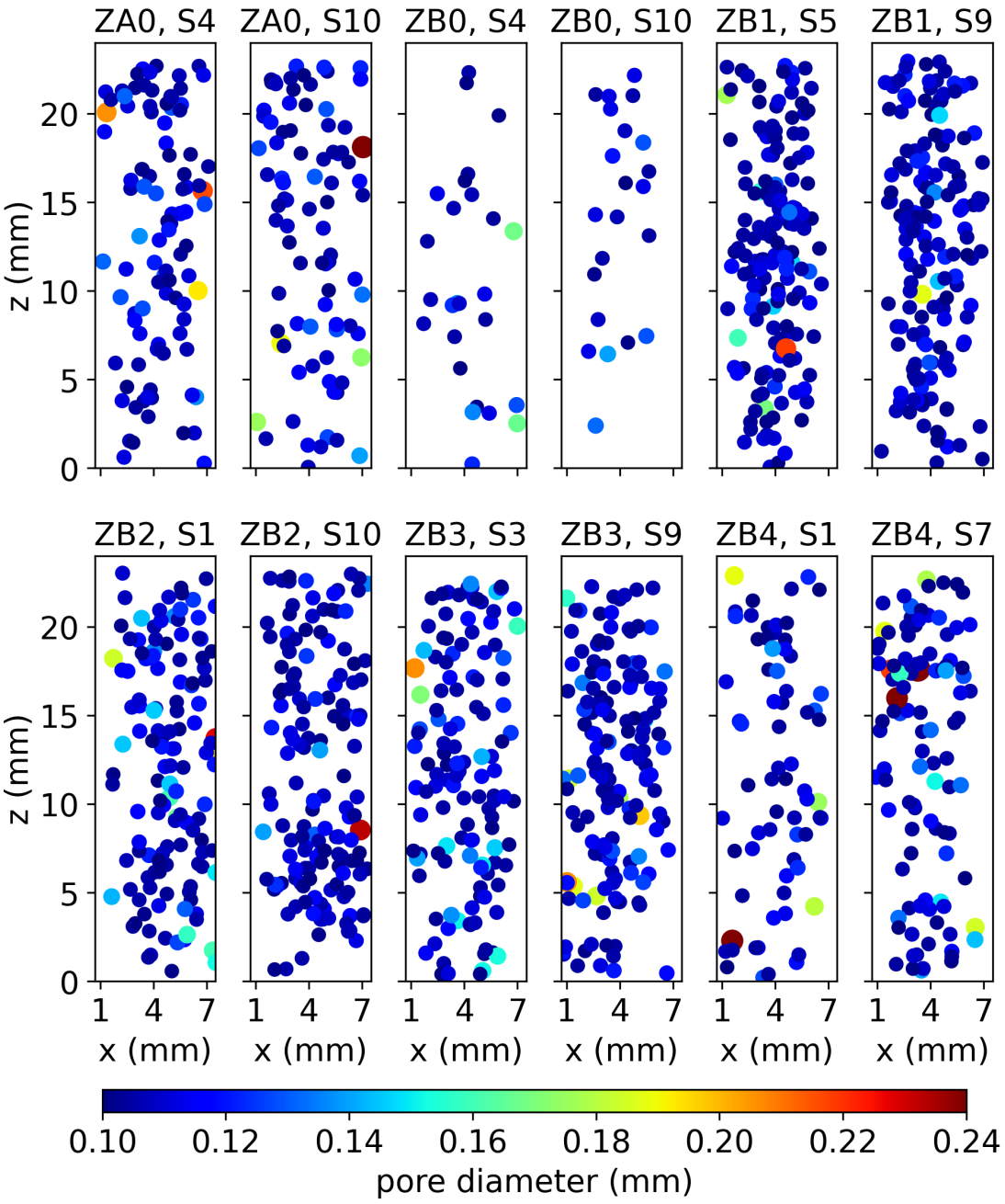

Figure C.16: Pore locations in select specimens for UW Round Robin Build 6, performed with **PA powder**. This shows pores as observed across the height of the vertical specimen. Pores with a circular equivalent diameter less than 100 μm have been omitted. The sizes of the dots are proportional to the circular equivalent diameter of the corresponding pore but have been exaggerated for easier visibility (i.e. pores are not to scale with the plot axes.)